UNIVERSITAT POLITÈCNICA DE VALÈNCIA

Doctoral thesis submitted for the degree of Doctor of Philosophy in Telecommunications Engineering

Investigation of multipolar interference in silicon disks for on-chip photonics

Evelyn Díaz Escobar

Supervisor: Dr. Alejandro José Martínez Abiétar

Valencia, February 2023

Ph.D. THESIS
Evelyn Díaz Escobar
Investigation of multipolar interference in silicon disks for on-chip photonics
Nanophotonics Technology Center
UNIVERSITAT POLITÈCNICA DE VALÈNCIA

A mi familia,
en especial a mi madre.

Abstract

High-index nanoparticles support electromagnetic multipoles that determine their response to an incident wave. When different multipoles are excited, they can interfere, giving rise to surprising phenomena. For example, from the antiphase oscillation of the Cartesian toroidal and electric (or magnetic) dipole or the corresponding higher-order multipoles arise the so-called anapole states, characterized by a substantial reduction in the far-field scattering and a strong localization of energy inside the disk. One of the simplest high-index structures supporting multipolar interference is the disk, which can be easily built on a silica substrate using standard silicon nanofabrication tools. Most studies of anapole states in high-index dielectric disks have addressed anapoles that can be excited under normal illumination, but the in-plane incidence is necessary for building silicon photonic integrated circuits (PICs) when light is completely bound to the chip plane.

In this thesis, we investigate via numerical simulations annex experimental measurements the appearance of multipolar interferences in silicon disks when we excited in-plane through waveguides. First, we investigate the effects on isolated subwavelength-sized disks and then extend our investigation to one-dimensional (1D) periodic chains. Under the in-plane excitation of a silicon subwavelength-sized disk, we observe magnetic and electric anapoles of various orders, changing the geometry of the system. Interestingly, we observed a decoupling of the minimum in the far-field scattering and the maximum of energy localization in the disk, which takes place at well-separated wavelengths for in-plane excitation of the anapole as compared to the usual normal incidence case. On the other hand, through the excitation of the toroidal dipole, we demonstrate the efficient transmission above the light cone in a periodic structure formed by silicon subwavelength-sized disks. Finally, we predict the closure of the Bragg bandgap due to the interaction between electric and magnetic dipoles in a periodic structure formed by silicon nanobricks. Our results highlight significant differences between multipoles interferences when the particles are illuminated from different directions and have direct implications for the use of wavelength-size disks in high-index PICs for applications ranging from biosensing and spectroscopy to nonlinear signal processing.

Resumen

Las nanopartículas de alto índice admiten multipolos electromagnéticos que determinan su respuesta a una onda incidente. Cuando se excitan diferentes multipolos, estos pueden interferir, dando lugar a fenómenos sorprendentes. Por ejemplo, a partir de la oscilación en antifase del dipolo toroidal y eléctrico (o magnético) cartesiano o de los correspondientes multipolos de orden superior surgen los llamados estados anapolares, caracterizados por una reducción sustancial de la dispersión de campo lejano y una fuerte localización de la energía dentro del disco. Una de las estructuras de alto índice más sencillas que soportan la interferencia multipolar es el disco, que se puede construir fácilmente sobre un sustrato de sílice utilizando herramientas estándar de nanofabricación de silicio. La mayoría de los estudios de estados de anapolos en discos dieléctricos de alto índice han abordado anapolos que pueden excitarse bajo iluminación normal, pero la incidencia en el plano es necesaria para construir circuitos integrados fotónicos de silicio cuando la luz está completamente unida al plano del chip.

En esta tesis investigamos mediante simulaciones numéricas anexas a medidas experimentales la aparición de interferencias multipolares en discos de silicio cuando excitamos en el plano a través de guías de ondas. Primero, investigamos los efectos en discos aislados del tamaño de una sublongitud de onda y luego ampliamos nuestra investigación a cadenas periódicas unidimensionales. Bajo la excitación en el plano de un disco de silicio del tamaño de una sublongitud de onda, observamos anapolos magnéticos y eléctricos de varios órdenes, cambiando la geometría del sistema. Curiosamente, observamos un desacoplamiento del mínimo en la dispersión de campo lejano y el máximo de localización de energía en el disco, que tienen lugar en longitudes de onda bien separadas para la excitación en el plano del anapolo en comparación con el caso de incidencia normal habitual. Por otro lado, a través de la excitación del dipolo toroidal, demostramos la transmisión eficiente por encima del cono de luz en una estructura periódica formada por discos de silicio del tamaño de una sublongitud de onda. Finalmente, predecimos el cierre de la banda prohibida de Bragg debido a la interacción entre dipolos eléctricos y magnéticos en una estructura periódica formada por nanobloques de silicio. Nuestros resultados resaltan diferencias significativas entre las interferencias multipolares cuando las partículas se iluminan desde diferentes direcciones y tienen implicaciones directas para el uso de discos del tamaño de la longitud de onda en circuitos integrados fotónicos de alto índice para aplicaciones que van desde la biodetección y la espectroscopia hasta el procesamiento de señales no lineales.

Resum

Les nanopartícules d'alt índex admeten multipols electromagnètics que determinen la seua resposta a una ona incident. Quan s'exciten diferents multipols, aquests poden interferir, donant lloc a fenòmens sorprenents. Per exemple, a partir de l'oscil·lació en antifase del dipol toroidal i elèctric (o magnètic) cartesià, o dels corresponents multipols d'ordre superior, sorgeixen els anomenats estats anapolars, caracteritzats per una reducció substancial de la dispersió de camp llunyà i una forta localització de l'energia dins del disc. Una de les estructures d'alt índex més senzilles que suporten la interferència multipolar és el disc, que es pot construir fàcilment sobre un substrat de sílice utilitzant eines estàndard de nano fabricació de silici. La majoria dels estudis d'estats d'anapols en discos dielèctrics d'alt índex han abordat anapols que poden excitar-se sota il·luminació normal, però la incidència en el pla és necessària per a construir circuits integrats fotònics de silici quan la llum està completament unida al pla del xip. En aquesta tesi investiguem mitjançant simulacions numèriques annexes a mesures experimentals l'aparició d'interferències multipolars en discos de silici quan excitem en el pla a través de guies d'ones. Primer, investiguem els efectes en discos aïllats de la grandària d'una sublongitud d'ona i després ampliem la nostra investigació a cadenes periòdiques unidimensionals. Sota l'excitació en el pla d'un disc de silici de la grandària d'una sublongitud d'ona, observem anapols magnètics i elèctrics de diversos ordres, canviant la geometria del sistema. Curiosament, observem un desacoblament del mínim en la dispersió de camp llunyà i el màxim de localització d'energia en el disc, que tenen lloc en longituds d'ona ben separades per a l'excitació en el pla del anapol en comparació amb el cas d'incidència normal habitual. D'altra banda, a través de l'excitació del dipol toroidal, vam demostrar la transmissió eficient per damunt del con de llum en una estructura periòdica formada per discos de silici de la grandària d'una sublongitud d'ona. Finalment, prediem el tancament de la banda prohibida de Bragg a causa de la interacció entre dipols elèctrics i magnètics en una estructura periòdica formada per nanobloques de silici. Els nostres resultats ressalten diferències significatives entre les interferències multipolars quan les partícules s'il·luminen des de diferents direccions i tenen implicacions directes per a l'ús de discos de la grandària de la longitud d'ona en circuits integrats fotònics d'alt índex per a aplicacions que van des de la biodetecció i l'espectroscòpia fins al processament de senyals no lineals.

Acknowledgments

Tras concluir un trabajo arduo como lo es la finalización de una tesis doctoral, es inevitable mirar atrás y pensar en cada una de las personas que contribuyeron e hicieron posible la culminación de esta. Por ello es para mí un verdadero placer utilizar este espacio para ser consecuente con cada una de ellas, expresándoles mis más sinceros agradecimientos.

Primero que todo y de manera muy especial quiero agradecer a mi supervisor Dr. Alejandro Martínez Abiétar por aceptarme para realizar esta tesis doctoral bajo su dirección. Sin lugar a duda, su apoyo y confianza en mi trabajo han sido determinantes. Su capacidad para guiarme ha ido más allá del desarrollo de esta tesis, también ha contribuido en mi evolución como investigadora. Los resultados alcanzados hoy en día no habrían sido posibles sin su orientación oportuna, bajo una dirección caracterizada por el respeto, el trato ameno y cercano, elementos esenciales para culminar cualquier proyecto exitosamente. Le agradezco también haberme facilitado los medios suficientes para llevar a cabo todas las actividades propuestas en el desarrollo de esta tesis.

Quiero agradecer de manera especial a una excelente profesional, a la que admiro profundamente, la Dra. Laura Mercadé; de quien debo destacar por encima de todo disponibilidad tanto a nivel laboral como personal. Sin duda es un camino difícil y más si toca recorrerlo lejos de casa, pero Laura es de esas personas que siempre quisieras tener cerca para sentir apoyo en ese arduo recorrido. Gracias por cada aporte, cada consejo desde la serenidad que te caracteriza, a ti también debo gran parte de mis resultados.

También quiero agradecer a la Dra. Ángela Barreda quien colaboró en muchos de los resultados presentados en esta tesis y estuvo siempre dispuesta a ayudar.

Quiero extender mi más sincero agradecimiento a mis compañeros del NTC: Alba, Sergio, David Zurita, Kike, Elena y Ana por toda la ayuda brindada; y a todos los que han estado durante este largo camino: Raúl, Alberto, Javi, Miguel, Frank, Maribel, Miroslavna, Miguel Sinusía, Víctor, Javi Albiac, Roberto, a todos en general, gracias por todos los excelentes momentos que compartimos dentro y fuera del centro, gracias además por estar al pendiente de mi evolución o cualquier preocupación que tuviera. Gracias también al equipo de fabricación, en especial a Amadeu, por estar dispuesto siempre a ayudar.

I also want to thanks to Dr. Thomas Bauer, Dr. Kobus Kuipers and Dr. Alessandro Pitanti for their collaborations.

Debo agradecer a la Generalitat Valenciana que con su programa de becas Santiago Grisolía GRISOLIAP/2018/164 me permitió comenzar este camino. Al Instituto de Tecnología Nanofotónica y a la Universidad Politécnica de Valencia por darme la oportunidad de labrar mi camino hacia el título de Doctor of Philosophy in Telecommunications Engineering en sus instalaciones.

A mis amigos: Luis Manuel, Steve, Ariel, Lianet, Diana, Luis Miguel, Beatriz, Jose

y Vicente que han compartido conmigo los “ires y venires” en el plano personal y por su disposición y apoyo en todo. En especial a Yoannet, que ha estado siempre en cada momento difícil que me ha tocado vivir y con sus sabias palabras y compañía me ha hecho sentir mejor, no alcanzan las palabras para expresarte todo mi agradecimiento. A todos muchas gracias por convertirse en mi familia en este lado del mundo.

Y, por supuesto, el agradecimiento más profundo y sentido va para mi familia, en especial a mi madre, estar lejos de ella ha supuesto uno de los principales retos para mí. Sin su inspiración, confianza, apoyo y motivación habría sido imposible llevar a cabo este arduo proyecto. A mi tía por ser un ejemplo a seguir y a mi primo Eduardo, ustedes saben todo lo que significan para mí. A Jorge, por su apoyo incondicional y por hacerme tan feliz. A mis abuelos y a toda mi familia en general, gracias por ser el pilar que sostiene mi vida.

List of abbreviations

PIC	Photonic Integrated Circuitry
CST	CST Microwave Studio - 3D Electromagnetic Simulation Software
FS	Free-Space
NSOM	Near-field Scanning Optical Microscope
THG	Third Harmonic Generation
TE	Transverse Electric
TM	Transverse Magnetic
FDTD	Finite-Difference Time-Domain
SEM	Scanning Electron Microscope
GST	$Ge_2Sb_2Te_5$
ED	Electric Dipole
MD	Magnetic Dipole
SOI	Silicon-On-Insulator
BIC	Bound States in the Continuum
PBG	Photonic Band Gap
1D	One-Dimensional
2D	Two-Dimensional
3D	Three-Dimensional
TIR	Total Internal Reflection

Contents

Chapter 1

Introduction

Contents

1.1 Background and motivation

The purpose of the photonic structures investigated in this thesis is summarized in the current chapter, which discusses the advantages of integrating wavelength-sized disk resonators supporting multipolar resonances in silicon photonic circuits. It includes a review of previous efforts in this area and discusses how this hybrid method can improve existing photonic integrated circuits and enable new and game-changing photonic applications.

1.1.1 Technological platform: silicon photonics

The technological platform that we use to build the proposed structures in this thesis is silicon photonics. The concept of employing silicon as a material for light guiding, filtering, and manipulation was initially investigated in the 1980s [1–3], but it was not until the last two decades when the demand for high-speed and low-power photonics emerged, that the field began to flourish as we know it today, becoming likely the dominant technology of PICs [4]. The ability to mass-produce low-cost devices integrating photonic and electronic components using current semiconductor fabrication processes (such as complementary metal-oxide-semiconductor (CMOS)) is the significant advantage of silicon photonics over competing strategies (such as III-V semiconductor heterostructures) [5–9].

Two main reasons were behind the original discard of silicon as an appropriate material for PICs: I) since silicon is an indirect bandgap material, we cannot build silicon

lasers; and II) silicon is centrosymmetric, thus lacking an electro-optic effect that prevents the realization of high-speed electro-optic modulators, which are essential in the electronic-to-optics conversion process. Notably, both problems can be solved. III-V lasers can be integrated on silicon PICs by means of bonding techniques [10, 11] and high-speed modulators can be realized on silicon employing the so-called free-carrier dispersion effect [12, 13].

Due to the performance of individual photonic devices being frequently vulnerable to variability in the geometrical features of the devices, silicon photonics faces the difficulty of high sensitivity to fabrication-process variations [14]. For instance, the device's transmission might be significantly impacted by variations in dimension as minor as a few ångströms. Unfortunately, the statistical distribution of atomic-scale material deposited or etched during wafer manufacturing makes it hard to attain the subnanometer precision that is frequently required. The insertion and propagation losses in silicon photonic systems continue to be a problem, particularly in systems where each photon is a valuable resource, as in quantum optics applications [4].

Silicon photonics can address some of these obstacles using solid-state physics notions, such as cooperative phenomena. Recent experiments have demonstrated that careful system engineering can frequently trade off characteristics, including bandwidth, robustness, size, and power dissipation. The parametric nonlinear processes in silicon-compatible materials can also be used in silicon photonics, and they are made more effective by group-velocity dispersion engineering and maximum light confinement for index guiding structures [15]. The strong confinement of light in the waveguides, which enables high intensities and dispersion engineering, has been proven to make these nonlinear processes in silicon nitride, for instance, effective. For example, multi-wavelength comb-like light sources based on this nonlinear phenomena [16] and high-performance photonic circuits that massively wavelength multiplex and de-multiplex systems with scalable aggregate bandwidth that is relatively immune to optical losses are both made possible by dispersion engineering. When low-bandwidth electronics are used, each optical lane's high-sensitivity light detection results in robustness to optical losses [4].

Silicon photonics seems to be also a very appropriate platform to allocate new fields of research such as optomechanics [17] and quantum integrated photonics [18]. Even with commercial devices on the market [19, 20], silicon integrated circuits made on silicon-on-insulator (SOI) (see Fig. 1.1) wafers are currently being used for label-free biosensors [21–23] and high-speed data transmission [24, 25], among other applications. The ability to successfully translate basic laboratory research into commercial realities and the ongoing advances of the scientific community continues to propel the field forwards [4, 9].

Still, on the way towards extreme miniaturization of PICs, research in silicon photonics needs new ways to reduce the total size of the basic structures used to process information, namely ring resonators, and Mach-Zehnder interferometers, which occupy from tens to hundreds of μm^2. This requires photonic elements able to strongly confine the optical fields in very small regions (tentatively, the size of a wavelength or even smaller), whilst presenting a resonant behavior that can be used to implement several functionalities. One possibility would be to integrate metallic elements - supporting plasmonic resonances - on silicon waveguides, an approach that could be interpreted as hybrid photonic-plasmonic circuits [26]. However, metallic elements display large absorption losses and also radiate out-of-chip [27, 28], which would result in reduced power efficiency when building on-chip functionalities.

A possible way to solve this issue is by using subwavelength scale high-index res-

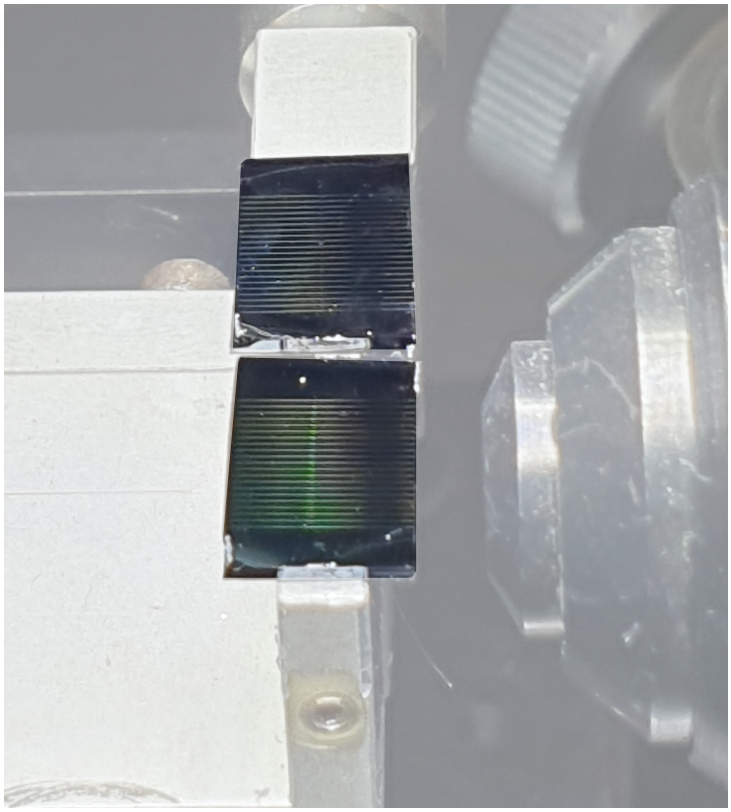

Figure 1.1: Image of SOI chips fabricated in Nanophotonics Technology Center (NTC) in Valencia.

onators [29,30]. Even though the size of such photonic elements is somewhat bigger than the size of plasmonic nanostructures, high-index nanophotonics allows for enormously reducing absorption losses (avoiding the use of metals) whilst still keeping wavelength and even subwavelength size dimensions. Moreover, they can be tailored to suppress out-of-plan scattering, thus enabling the whole optical field to be confined in the PIC.

1.1.2 High-index nanophotonics

The field of nanophotonics has grown rapidly in recent years due to new ideas in the physics of metamaterials and metasurfaces as well as the quick advancement of nanoscale fabrication technologies, which enable a variety of applications reliant on adaptable and effective subwavelength light manipulations (e.g. [29, 31–42]). Similar to conventional photonics operating at other spatial scales, fundamental research, and applications in nanophotonics heavily rely on resonant light-matter interactions; therefore, a thorough analysis of the excitation and interference of electromagnetic multipoles is typically essential and indispensable to know the optical response of high-index resonators [37, 38, 43–46].

Mie theory can be used to describe the electromagnetic response of high-index nanoparticles [47]. This means that by obtaining the near-fields when illuminating a high-index nanostructure, we have analytical solutions to model the far-field scattering. For very small (in terms of the wavelength) nanoparticles, the electric and magnetic dipoles dominate conventional multipole expansions, which are often used for dynamic

charge-current distributions on length scales much smaller than the effective wavelength of light [43, 45, 46, 48]. However, higher order multipoles, including dynamic toroidal multipoles, will emerge when the dynamic charge-current is dispersed over a region that is comparable to or bigger than the effective wavelength of light, and they will help to produce complex electromagnetic fields [43, 45, 46, 48, 49]. Notably, the interference of different multipoles can lead to intriguing effects, being one of them the cancellation of far-field scattering [50]. Such effects have been normally observed when illuminating a set of high-index scatterers using free-space propagating beams impinging under (quasi-) normal incidence. Illuminating such scatterers laterally, as required to build PICs, may enable to observe such multipolar interferences on-chip [46], thus enabling the application of high-index nanophotonics in silicon PICs. This is the key objective of this thesis.

1.1.3 Suppressing far-field scattering: Anapole states

As mentioned above, this thesis investigates the observation of multipolar interference in a very simple high-index scatterer (a silicon disk) so that out-of-plane scattering can be canceled and the large field confinement in the dielectric element can be used to build ultra-compact on-chip photonic elements. For this reason, in this subsection we explain in detail how the scattering can be suppressed via multipolar interference resulting in the scatteringless electromagnetic states labeled anapoles. Moreover, we will detail the different experiments reporting on the observation of anapoles states, as well their application in several functionalities when using free-space (FS) propagating light.

Light scattering by high-refractive-index dielectric nanoparticles can be explained by the formation of a set of radiative displacement currents upon illumination with an external source [29, 51]. Mie theory allows us to obtain analytical formula to get the far-field scattering from such currents. Interestingly, under certain conditions, a given combination of displacement currents may not scatter light due to destructive interference in the far field, resulting in the so-called anapole state [47, 50, 52–57] (see Fig. 1.2).

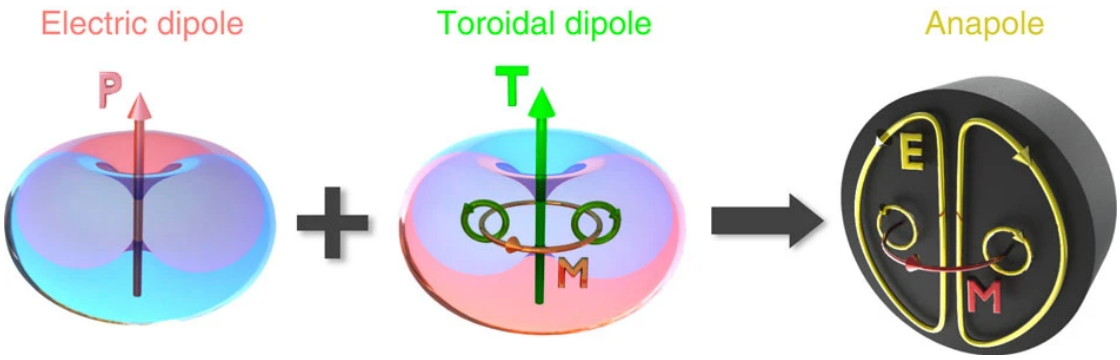

Figure 1.2: Illustration of an anapole excitation. The toroidal dipole moment is associated with the circulating magnetic field **M** accompanied by electric poloidal current distribution. Since the symmetry of the radiation patterns of the electric **P** and toroidal **T** dipole modes are similar, they can destructively interfere, leading to total scattering cancellation in the far-field with non-zero near-field excitation. [50]

Describing the electromagnetic response of the nanoparticle by a set of multipole eigenstates (derived from the polarization currents), such an anapole condition results from the antiphase oscillation of the Cartesian electric and toroidal dipole or corresponding higher-order multipoles [47, 50, 52–58]. Notably, an anapole is not a natural eigenmode of a certain electromagnetic structure so that, for example, it cannot lead to lasing [57]. This is why we call it an anapole state but not an anapole resonance or an anapole mode. In contrast, an anapole is a distinct state that results from the interference between two eigenmodes of the nanoparticle, thus being reminiscent of the first and second Kerker conditions [59] arising from the interference between electric and magnetic dipolar Mie-type resonances, as well as the formation of accidental quasi-bound states in the continuum via the strong coupling of a Mie-type and a Fabry-Pérot-type resonance [60].

Unlike metamaterial-based cloaking structures [61], which are characterized by the complete absence of local internal fields since the radiation cannot go through the cloak [57, 62], anapole states are usually accompanied by a strong concentration of electromagnetic energy inside the nanoparticle [47, 63, 64]. This remarkable feature has been used to boost light-matter interaction and enhance nonlinear effects such as harmonic generation [65–67] or Raman scattering [68] in different experiments. This is indeed one of the main motivations of this thesis: since such nonlinear effects - which can be used for all-optical signal processing [69] - can be observed using FS optical excitation, can they also be observed under lateral illumination thus paving the way towards on-chip nonlinear high-index nanophotonics?

A prototypical structure to achieve radiationless anapole states is a high-index nanodisk [50, 52, 63], which can be easily fabricated on low-index substrates using standard lithography techniques. This is the case, in particular, of SOI wafers, so silicon disks supporting anapole states can be fabricated using standard silicon technology. The two main signatures of the electric anapole condition in high-index disks are: (i) in the far field, a strong suppression of scattering [50] and (ii) in the near field, the formation of poloidal displacement currents with the electric field forming local vortices, with opposite rotation sense in each half of the disk [63].

Anapoles have been the focus of several publications, highlighting their excitation for various configurations and showcasing their wide range of applications. Notably, the main feature that all of these reports share is that anapole states are excited from the top (normal or quasi-normal incidence) using FS propagating beams. In what follows, we summarize the main works that we have found in the literature.

In 2015, Miroshnichenko et al. [50] introduced the anapole state term as a composition of electric and toroidal dipole moments, resulting in destructive interference of the radiation fields due to the similarity of their far-field scattering patterns (see Fig. 1.2). The authors demonstrated for the first time the existence of an anapole state in optics in a very simple structure: a silicon nanodisk. They discovered that the anapole state, which can be experimentally activated and observed with a normally-incident plane wave, is supported by a silicon nanodisk with a diameter ranging from 200 to 400 nm and a height of 50 nm situated on a quartz substrate. With three-dimensional (3D) Electromagnetic Simulation Software - CST Microwave Studio (CST) calculations, the authors observed a significant dip in the far-field scattering spectrum and an increase in the near-field inside and around the disk, which showed the presence of the electric and toroidal dipoles that together form the anapole state configuration. These calculations are confirmed through current Cartesian and field spherical multipole de-

compositions where the authors observed strong suppression of the total scattering due to the far-field cancellation of electric and toroidal dipole radiations, which is precisely the condition for anapole state excitation. To confirm these theoretical predictions, they performed experiments where the far-field scattering spectra were measured using single nanoparticle dark-field spectroscopy. The authors found that a scattering dip appeared around 550 nm for disks with diameter > 200 nm, which was in good agreement with the theoretically predicted anapole excitation. Finally, using a near-field scanning optical microscope (NSOM) and a supercontinuum light source, the near-field distribution surrounding the disks was mapped at various wavelengths to demonstrate that the spectral dip in far-field scattering corresponded to the dark anapole state excitation.

In 2016, Ren Wang and Luca Dal Negro [52] through the engineering of non-radiative anapole states using numerical simulations, suggested a novel, frequency- and angularly-broadband method to achieve absorption rate enhancement in high-index dielectric nanostructures. Using the multipolar decomposition method, the authors demonstrated anapole-driven absorption enhancement in nano-disks and square nano-pixels composed of silicon and germanium absorbing materials with wide and controllable wavelength tunability. Additionally, they carefully examined how the nanostructure's width D and height H affect the spectra of absorption enhancement, and they determined that an aspect ratio of $H/D \sim 0.2$ is ideal for the stimulation of anapole states with the best possible absorption enhancement. For a silicon nano-disk with $D = 350$ nm and $H = 60$ nm, the authors showed that the resonant anapole state is excited at 710 nm by a linearly polarized plane wave. They also investigated the effects of incidence angle and incident wave polarization, and they discovered that anapole states are polarization sensitive and that, when disturbed by the emergence of additional electromagnetic multipoles, their spectral purity significantly degrades beyond 20° incidence, particularly for the p-polarization. The authors looked at the impact of coating, and they demonstrated that even when coating both sides of the nanostructures with a low-index dielectric layer, anapole-induced absorption amplification is still possible. Finally, they designed dimers as a specific example of nanostructured arrays with enhanced absorption bandwidth.

Wei et al. [53] presented a method for radiationless excitation of a high-index isotropic dielectric nanosphere's anapole state by illumination with tightly focused radially polarized beams. The authors showed that the anapole state could be triggered by a single-focused beam, however electric quadruple radiation was still a negligible contribution to the total scattering power. They found that a 4π configuration, where the two counter-propagated radially polarized had the same amplitude but a different phase, could excite an ideal radiationless anapole, which demonstrated a situation in which the reciprocity condition was not broken, but a non-radiating mode could still be excited by external illumination. This was the first time in which a configuration that allowed the excitation of the anapole state in an isotropic spherical Mie particle was proposed.

Grinblat et al. [66] observed experimentally enhanced third harmonic generation (THG) by exciting a germanium nanodisk at the anapole state. The electric field energy within a thin germanium nanodisk was maximized due to high confinement within the dielectric, which was evident from the disk's pronounced valley in its scattering cross-section at the anapole state. To understand the nature of the anapole state, the authors analyzed how the third harmonic signal varied with disk size and pump wavelength. They demonstrated that at an excitation wavelength of 1650 nm, each germanium nanodisk produced a highly effective third-order susceptibility, corresponding to an associated third harmonic conversion efficiency of 0.0001%, which is four orders of magnitude

improvement over the case of an unstructured germanium reference film.

In 2017, Luk'yanchuk et al. [54] studied the light scattering from a single spherical particle with high-index of refraction and distinguished between two types of anapole states: electric and magnetic, with significant differences between them. First, greater size parameters were required for the excitation of the magnetic toroidal mode, which often resulted in bigger contributions from the other excited modes. Second, the energy flow between these two types of anapoles differed significantly. The magnetic anapole concentrated the energy outside the particle, something like plasmonic particles, whereas the electric anapole concentrated energy inside the particle. Finally, the authors showed that hybrid anapole states could emerge when both forms of anapole states were activated simultaneously. However, the partial contributions from higher-order modes, which resulted in the production of non-trivial field configurations with vortices and singularities both within and outside the particle, hindered this phenomenon from occurring for spherical particles. The authors showed that for a sphere with refractive index $n = 25$, the second zeros of dipole scattering were discovered for the electric dipole (ED) at size parameter $q = 0.309$ and the magnetic dipole (MD) at $q = 0.353$. This paper highlighted the fact that anapole states can take place beyond the interference between the electric dipole and the toroidal dipole (first electric anapole): higher-order anapoles, therefore, will be present in high-index nanoparticles.

Luk'yanchuk et al. [62] also found that related to the excitation of an anapole state with an associated spectral Fano line shape, there were conditions for which the scattering of a small spherical dielectric particle was strictly below the value that follows from the Rayleigh limit. The authors determined that the small size parameter $q << 1$, a big refractive index, typically $n > 5$, and weak dissipation were the only requirements for such ultra-small scattering.

Grinblat et al. [65] presented that third harmonic generation (THG) nonlinear processes could be significantly improved, in particular, when the dielectric nanoantenna supported the nonradiating anapole state, which is characterized by a minimum in the extinction cross-section and maximum electric energy within the material. The authors demonstrated that a higher-order anapole state provided the maximum THG efficiency on the nanoscale at optical frequencies in a 200 nm thick germanium nanodisk. They identified the formation of a higher-order anapole state with a valley in the extinction cross-section - which was substantially narrower than that of the fundamental anapole - by doubling the diameter of a disk that supported the fundamental anapole state. At a third-harmonic wavelength of 550 nm, the authors saw a greatly enhanced electric field confinement effect within the dielectric disk, resulting in THG conversion efficiencies as high as 0.001%. Additionally, they saw the anapole near-field intensity distributions by mapping the THG emission throughout the nanodisk.

Gongora et al. [70] proposed a nanoscale laser based on a tightly confined anapole state. The authors showed via numerical simulations how to design nanolasers based on InGaAs nanodisks as on-chip sources with distinctive optical features using the anapole state's non-radiative nature. They showed the creation of ultrafast (of 100 fs) pulses via spontaneous mode locking of multiple anapoles, as well as a spontaneously polarized nanolaser that can couple light into waveguide channels with four orders of magnitude more intensity than conventional nanolasers.

Mazzone et al. [71] investigated the interaction and coupling of a group of anapole states in silicon nanoparticles. The authors showed anapole state transfer across an ensemble of nanoparticles by combining simulation and analytical results. They selectively

excited the first anapole state in one nanochain and characterized the propagation of energy along the chain. The authors showed that nanochain might support guided modes that propagate without radiative losses at distances of several µm, even across deformations and bends, thanks to the effective near-field coupling between nearby nanoparticles.

Zenin et al. [72] studied experimentally the anapole states of silicon disks excited by a plane wave in FS and on top of a glass substrate. The authors demonstrated three methods to indicate the presence of anapole states in the disks: (1) a reduction in the total scattering cross-section, (2) a local maximum in the total accumulated electromagnetic energy inside the particles, and (3) a reduction of the normal near-field electric component. The authors demonstrated that all three identification methods yielded comparable outcomes, with standard errors under 5%. They finally showed that narrower resonances and stronger energy concentration are relevant features of higher-order anapole states.

In 2018, Li et al. [56] discussed how the magnetic toroidal dipole and the magnetic dipole interact to produce the lowest order of magnetic anapoles. The authors showed how to remove higher-order components from curvilinear coordinate systems using a simple but general method. By expanding the Bessel or spherical Bessel functions, they could separate the toroidal multipole components of multipole expansions in polar coordinates (two and three dimensions). Their approach showed that higher-order current configurations with the same radiation properties as the pure electric dipoles exist in addition to the electric toroidal multipole. The authors found that the perfect cancellation of all higher-order current configurations was necessary for the anapole condition (this is, complete suppression of far-field scattering).

Yang et al. [63] demonstrated a strong field enhancement with anapole assistance in individual all-dielectric nanostructures. Using numerical simulation, the authors shown that under normal incident plane wave illumination strong electric fields with multiresonant intensity increases reaching 10^3 times can be generated within individual all-dielectric nanostructures, such as a slotted silicon nanodisk. By creating a specialized slot region at anapole state-generated electric field maxima, boundary conditions were used to promote electric field enhancement without degrading the far-field characteristics of anapoles. An extensive analysis of the system's fundamental and higher-order optical responses was performed using a multipole decomposition technique. The authors also reported how geometric parameters and mode interactions affect spectral evolution and intensity enhancement in the anapole state.

Timofeeva et al. [67] presented a novel method for fabricating disk nanoantennas from III-V nanowires, a new design idea based on free-standing disks, and an end-to-end approach for studying nanostructures supporting non-radiating topologies in the optical range. Using those disk nanoantennas, the authors experimentally demonstrated the suppression of far-field radiation and the strongly correlated substantial amplification of the second-harmonic generation. The technology presented involved cutting nanowires with a focused ion beam milling tool, enabling the construction of disk-based designs on any substrate. The approach that the authors offered is broad and can be used for many nanowire and nanomaterial types, which may also include silicon.

Baranov et al. [68] demonstrated that the anapole condition of silicon nanodisks strongly enhances another nonlinear process: Raman scattering. The authors showed a peculiar situation where a reverse correlation was observed; they quantified a multifold enhancement of Raman emission combined with suppressed elastic scattering. The system that enabled this peculiar effect was conformed of silicon nanodisks excited in

the so-called anapole state, for which the optical fields in the core of the silicon particles were enhanced, amplifying light-matter interaction and Raman scattering at the Stokes-shifted emission wavelength while the electric and toroidal dipoles interfered destructively in the far-field, preventing elastic scattering.

Lamprianidis and Miroshnichenko [73] explored numerous experimental settings for obtaining the so-called magnetic anapole states. The total suppression of magnetic dipole scattering was connected to such modes. The authors used a unique configuration of structured-light excitation to be able to achieve anapole states experimentally. It turns out that, under certain conditions, only spherical harmonics of the magnetic type were presented in the focal region of azimuthally polarized beams. The coupling between the particle and higher-order harmonics depended on the particle size in relation to the incident wavelength. Due to symmetry principles, the authors exposed that it was possible to cancel out all harmonics of even order by using two counter-propagating out-of-phase beams. This created the perfect environment for the excitation of a magnetic anapole state in a silicon nanosphere, especially when combined with a phase mask applied to the beams that are intended to reduce the interfering octupolar content. They also covered practical configurations for the experimental detection of magnetic anapole states, based on silicon nanodisks and nanopillars. By using a singular value decomposition of their T-matrices, the authors described the physical mechanism of their excitation in the hosting nanoparticles using the T-matrix formalism.

Xu et al. [74] proposed a mirror-enhanced anapole system to considerably improve the efficiency of the THG process. The authors demonstrated that using an anapole resonator on a mirror system (Au film), one can obtain (i) high near-field enhancement based on an overlap between the resonantly excited Cartesian electric and toroidal dipole moments, a property that is not possible with regular anapole resonators, and (ii) free-charge oscillations within the interface that act as an additional nonlinear source below the interface and further increase the total achieved nonlinear emission. As a result, compared to a typical anapole resonator on an insulator substrate, the authors' arrangement increased the third harmonic emission by two orders of magnitude. They presented an outstanding overall third harmonic conversion efficiency of 0.01%.

In 2019, Baryshnikova et al. [47] provided a concise summary of the theoretical and experimental findings on the physics of optical anapoles with an emphasis on the most recent developments in its application to subwavelength dielectric structures and metaoptics. The authors began by studying anapoles concepts in metaoptics and tackled papers showing experimental observations. Finally, they summarized the applications of anapoles as enhanced nonlinear effects, nanolasers in subwavelength photonics, and anapole-driven metamaterials, among others.

Monticone et al. [57] studied the similarities and differences between two classes of radiationless scattering states, anapoles and embedded eigenstates, concentrating mainly on the problem of exciting these field distributions in an open cavity and the implications of reciprocity. The authors showed that the embedded eigenstate fields are orthogonal to the polarization fields induced at their frequency, which means they cannot link to external stimulation in a linear reciprocal system. They demonstrated that the anapole is an induced radiationless field distribution that corresponds to a zero of the dipolar scattering coefficient rather than an eigenmode of the scattering system. Because of this, the anapole state only exhibits nonradiative properties when a monochromatic incident field is outside of it. However, when the excitation is turned off, the anapole state begins to disintegrate into radiation.

Gurvitz et al. [58] addressed theoretically high-order toroidal moments as well as their related higher-order anapole states, greatly extending the Cartesian multipole analysis to the magnetic 16-pole and electric 32-pole. The authors demonstrated the ability to build high-order anapole states up to electrical octupole anapole. They showed how anapoles, which can be both magnetic and electric, can localize either magnetic or electric energy inside a particle. Finally, the authors developed conditions for the simultaneous realization of two anapoles of different types to excite a "hybrid" anapole state.

Tian et al. [75] showed that by structuring the phase-change alloy $Ge_2Sb_2Te_5$ (GST), anapole states can be actively controlled. Through a meticulous multipole investigation, the authors looked into the fundamental optical response of individual GST nanostructures. They discovered that the GST material's high index and striking optical contrast enable its nanostructures to support a distinctive series of Mie resonances with active tunability. They proved the spectrum shifting between the scattering bright and dark states that correspond to the ED and anapole states, respectively. The authors demonstrated that the ED-to-anapole shifting in a GST nanodisk might be accomplished by only introducing a phase change $\Delta C = 50\%$ at any given wavelength between 3.9 µm and 4.6 µm and with an arbitrary crystallinity of the GST disk.

A careful investigation of the multimodal shifting among all of these states also revealed the existence of higher-order anapole states.

In 2020, Kapitanova et al. [76] theoretically predicted and empirically proved that magnetic anapole states—also known as magnetic-type non-radiating sources—can occur in a dielectric cylindrical particle and are characterized by suppressed MD radiation. The authors demonstrated and explained the physical basis of the anapole state through the multipole expansion analysis. They assumed a TE-polarized plane wave-excited infinitely long water cylinder with a radius of 18 mm. Around the frequency of 1.55 GHz, they detected the formation of the magnetic anapole state due to the destructive interference between the MD and the magnetic toroid led to significant suppression of the contribution of the spherical MD in the scattering cross-section. The finite-size prototype's experimental study validated its distinctive three-hump magnetic field distribution inside the particle, which corresponds to the magnetic anapole state, and its primarily dipole-like emission in the far-field zone. They conducted experimental research in the microwave frequency range that allowed them to directly examine the distinctive field profile inside the dielectric particle and measure the far-field (scattered field) characteristics. The idea holds throughout frequency ranges, from the visible range for nanoparticles to the microwave region for objects millimeters in size.

1.1.4 Multipolar interference in periodic chains of high-index nanoparticles

So far, we have only considered the existence of multipolar moments -as well as their interference causing anapoles - in single nanoparticles. Even when characterized forming arrays, as in [50], the response of the system is dominated by the response of a single nanoparticle, and coupling between adjacent nanoparticles is thus disregarded. However, the excitation of different electromagnetic multipolar moments may also lead to interesting effects when periodic chains are formed.

Indeed, it was shown via numerical simulations in [71] that chains of high-index disk supporting anapole states may guide light efficiently as a result of the cancellation of far-field scattering. Notice that such guiding takes place for modes over the light cone,

thus coexisting the continuum of radiation, so they should be inherently lossy. In [77], guidance through chains of high-index disk was analyzed, but the authors found that the guidance at wavelength around the anapole state is not very efficient. However, when each dielectric disk was divided into two halves by inserting an air slot (see Fig. 1.3), highly efficient guidance - even through sharp bends - was observed in simulations as well as in experiments around 10 μm wavelengths [77].

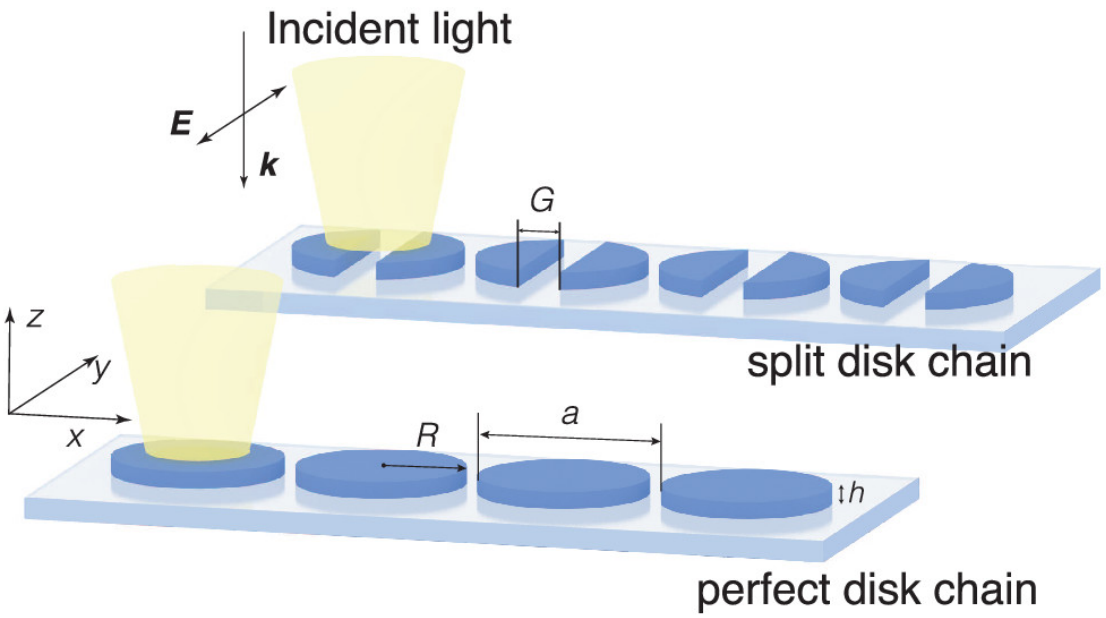

Figure 1.3: Sketch of periodic chains of disk (slotted and regular) excited from the top by a plane wave, as proposed in [77]. Reprinted with permission from [77]. Copyright 2023 American Chemical Society.

In summary, Huang et al. [77] demonstrated theoretically and experimentally that anapole-based chains made of subwavelength silicon disks with air gaps (G) (Fig. 1.3) are highly efficient at compactly transferring electromagnetic energy over long distances. The authors discovered that an air-gap structure could increase the energy confinement within the isolated disks, which boosts the chain's effectiveness even more. Specifically, the authors found that the split disk with $G = 0.5R$ is the best candidate for electromagnetic fields confinement, and the anapole state appears around 10.2 µm for a disk with radius R= 3.83 µm when excited by a plane wave. By achieving a 90° bending loss of 0.32 dB at the optical communication wavelength, the authors showed that the chain is low loss and scalable at infrared wavelengths. As suggested in Ref. [77], efficient guide light should be most valuable when building the chains on SOI and performing the guidance in the technologically-relevant telecom wavelength regime.

Since interference between multipolar moments play a role in the light guidance along periodic chains of dielectric scatterers above the light line, where guided modes are inherently lossy, it makes sense to see if there will be also some interesting effect arising from multipolar interference below the light line, when inherently lossess guided modes can appear. In this case we are going to low frequencies (to operate below the light cone), so the modes involved in this interaction will be mainly the electric dipole and the magnetic dipole.

The periodic modulation (period a) of the index of refraction of a dielectric medium gives rise to photonic band gaps (PBGs) where electromagnetic propagation along the direction of periodicity is forbidden [78]. If we consider a periodic medium formed by periodic layers of indices n_1 and n_2, a so-called 1D photonic crystal, the lowest-frequency PBG opens due to the splitting of the so-called dielectric and air bands at the Bragg wavelength, defined as $\lambda = 2\bar{n}a$, where $\bar{n} \approx \frac{n_1+n_2}{2}$. Interestingly, the width of the PBG is directly proportional to the index contrast, as $\Delta n \approx \frac{n_1-n_2}{\bar{n}}$. This essentially means that the PBG arises even for minute values of Δn, as in the case of fiber Bragg gratings used as wavelength filters in telecom networks [79], and can become very large when high-index materials—such as silicon—are used. Indeed, the existence of full, three-dimensional (3D) PBGs in 3D photonic crystals can be explained as the overlapping of wide 1D-PBGs in every possible spatial direction, i.e., for every possible wave vector k [80, 81].

The first PBG is remarkably important in integrated guided optics since it is usually the only one placed below the light cone [82, 83]; therefore, it can give rise to localized modes with large Q factor when defect-like cavities are created. In the integrated optics arena, the confinement of light waves below the light line is achieved due to total internal reflection in the two dimensions perpendicular to the propagation direction, in which the system is periodic.

Recently, it has been shown theoretically [84] that the first (or Bragg) PBG can vanish in a 1D periodic thin film, though only for TM modes (with the electric field perpendicular to the film) and not for TE modes (with the electric field parallel to the film). This result is explained from the different boundary conditions to be satisfied by the electric and magnetic fields when propagating along the periodic film. However, this study was two-dimensional (2D) and did not include lateral confinement of the waves. From a practical perspective, it would be interesting to see whether the closure of the PBG is also maintained when transversal confinement via total internal reflection (TIR) is introduced, as in 1D photonic crystal slabs [85] built in high-index films. Moreover, if the chain is formed by high-index scatterers, it makes sense to analyze if the multipolar features of such scatterers have any influence on the closure of the PBG.

1.1.5 Motivation of the thesis

To the best of our knowledge, all previous experiments reporting on the observation of anapole states have made use of FS light impinging on the disks in a direction perpendicular to the substrate (out-of-plane incidence as show Fig. 1.4), with the disk either flat on the substrate [50, 72] or vertically standing [67].

However, it would be interesting to look at the properties of such states when excited by light propagating in-plane, as is the case in PICs, which are extensively used in multiple applications, including optical processing and communications, sensing or spectroscopy [86]. In this sense, the realization of anapole states may add novel functionalities to the existing utilization scenarios of high-index disks in PICs [87, 88]. In particular, anapole states could play a key role in nonlinear light processing in PICs, for instance, by reducing the footprint and power consumption of all-optical switching [69] and other nonlinear processing elements [89] while the undesired out-of-plane scattering could be completely suppressed. In comparison with other subwavelength-sized resonators, such as photonic crystal cavities, anapoles display a much broader bandwidth, which would enable a faster response as well as supporting processes such as four-wave mixing [90],

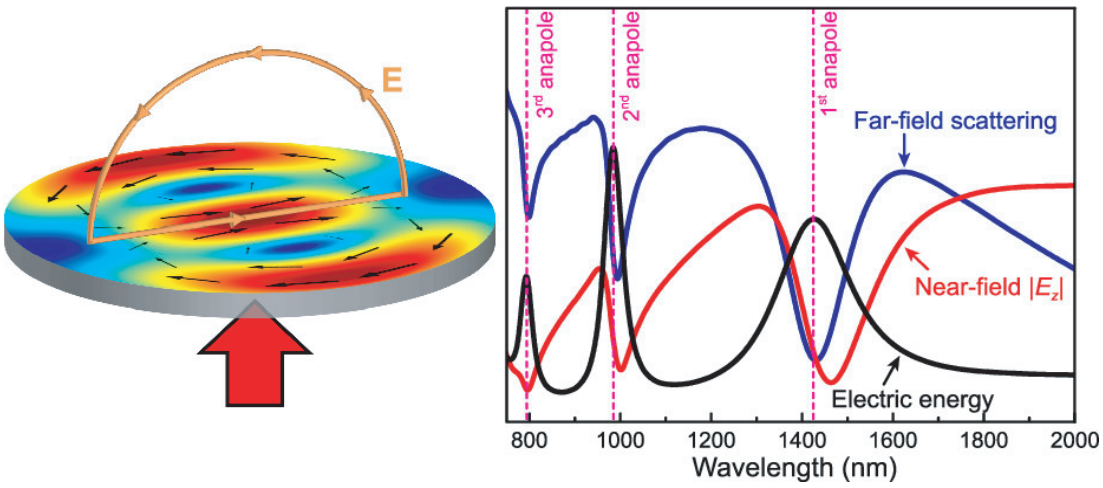

Figure 1.4: Illustration of the anapole state excitation in a silicon disk upon normal x-polarized plane-wave illumination and spectra of far-field scattering, near-field $|E_z|$ and electric energy where it is possible to observe different order of electric anapole states [72]. Reprinted with permission from [72]. Copyright 2023 American Chemical Society.

which could be employed in nonlinear signal processing.

Therefore, a main motivation of this thesis is to investigate numerically and experimentally if anapole states (of different orders) can be excited on-chip (this is, laterally instead of from the top) and still conserve their inherent properties: reduced scattering (particularly in the out-of-plane direction) and extreme field localization in the disk. To anticipate that this is possible, Fig. 1.5 shows the top scattering and disk intensity spectrum of a silicon disk when it is excited in-plane by a waveguide with modes similar to TE (Fig. 1.5**a**) and TM (Fig. 1.5**b**). Different orders of electric and magnetic anapole states are observed. In Chapters 2 and 3 we conduct detailed experiments to know more about such anapole states, and we show that they can be excited using a waveguide termination placed in close proximity to the disk.

It was also our motivation to see if slotted chains of silicon disks could guide light at telecom wavelength, as highlighted in [77]. As detailed in Chapter 4, we show that such guidance is possible but, interestingly, it can not be explained from the excitation of the first electric anapole but from the interference between the toroidal dipole and the magnetic quadrupole of the disk.

Finally, we addressed the closure of the PBG in 1D chains of nanobricks (here we used nanobricks instead of disks as dielectric scatterers, but our results could be also applied to disks) and we obtained that the interplay between the electric and the magnetic dipoles contributed to the disappearance of the PBG.

1.2 Structure of the thesis

The contents of the dissertation are distributed along the following chapters:

- In chapter 1 it is summarized the purpose of this thesis, which discusses the advantages of integrating silicon photonics and disk resonators. It includes a review

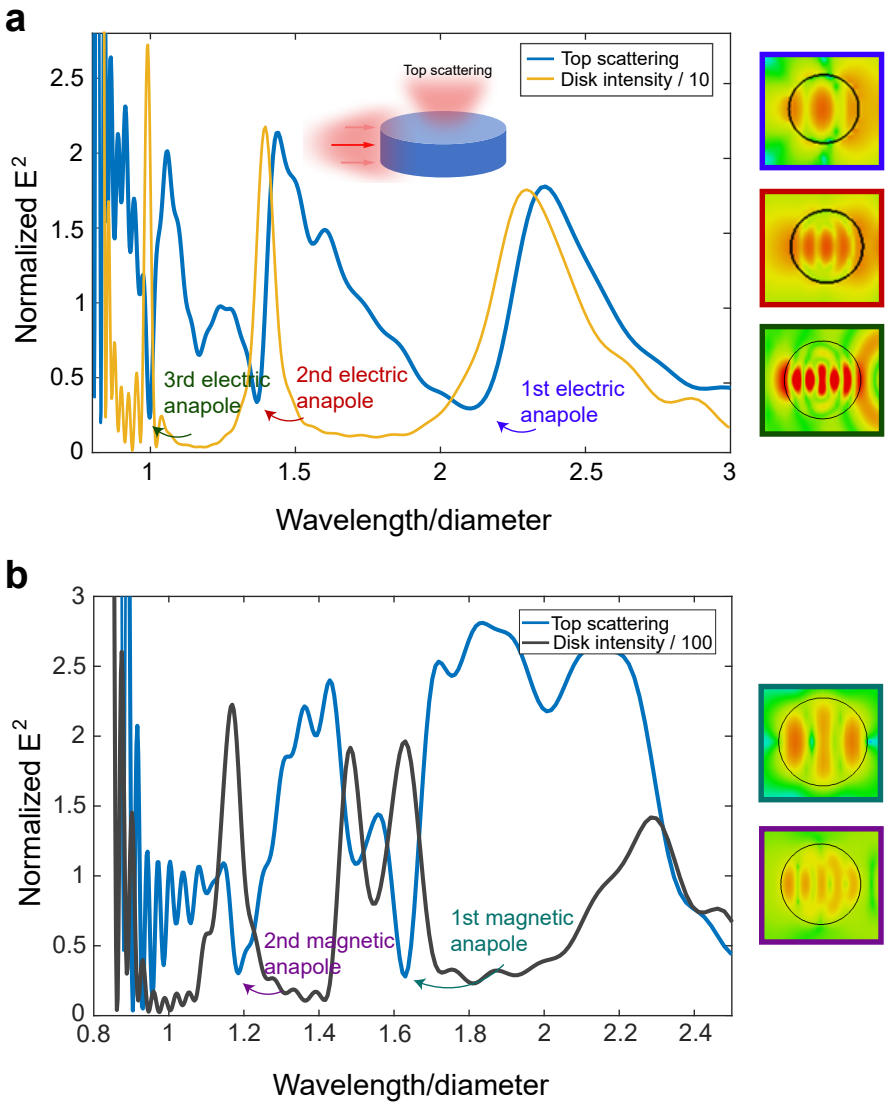

Figure 1.5: **Anapole states of silicon disks upon lateral illumination.** Top scattering and disk intensity spectrum with different orders of **a** electric and **b** magnetic anapole. Near-field patterns of the different anapole-orders are shown in the right panel. The disk dimensions are radius $r = 500$ nm and thickness $t = 350$ nm.

of previous efforts in this area and discusses how this hybrid method can improve existing photonic integrated circuits and enable new and game-changing photonic applications.

- In chapter 2, it is demonstrated that the first electric anapole state of an isolated silicon subwavelength-sized disk can be efficiently excited using an in-plane silicon waveguide as an illumination source. This fact significantly differs from the usual method of excitation of anapole states by FS plane-wave-like light, where the transverse component is dominant, making this study crucial for adequately designing the structures.

- In chapter 3, it is demonstrated that the second electric and magnetic anapole state

of an isolated silicon subwavelength-sized disk can also be efficiently excited using an in-plane silicon waveguide as an illumination source. These results highlight important differences between anapole states when the particles are illuminated from different directions and have direct implications to the use of wavelength-size disks in high-index PICs for applications ranging from biosensing to nonlinear signal processing.

- In chapter 4, it is demonstrated light guiding though straight and bent chains of silicon subwavelength-sized disks using an in-plane silicon waveguide as an illumination source. Our results highlight the potential of interference between different multiple moments using very simple and compact elements as wavelength-sized disc resonators to build complex functionalities in integrated photonics.

- In chapter 5, it is demonstrated that the interplay between the electric and magnetic dipole resonances of a single nanobrick can lead to the closure of the Bragg PBG for guided modes when forming a 1D photonic crystal. Our finding may have important consequences for the fields of photonic crystals and all-dielectric metamaterials.

Figure 1.6 shows a summary table of the main findings of each chapter along together with the dimensions of the employed high-index scatterers.

Chapter	Multipole interaction	Mode	Result	Dimensions of the structures	Wavelength
2	Electric and toroidal dipoles	TE	First-order electric anapole	Disk *r:* 350 nm *t:* 220 nm	1530 nm
3	Electric quadrupoole and toroidal dipole	TE	Second-order electric anapole	Disk *r:* 550 nm *t:* 350 nm	1510 nm
	Magnetic and toroidal dipoles	TM	First-order magnetic anapole	Disk *r:* 450 nm *t:* 350 nm	1480 nm
4	Excitation of toroidal dipole and magnetic quadrupole	TE	Efficient transmission above the light cone	Chain of disks *r:* 410 nm *G:* 0.5**r* *t:* 350 nm	1500 nm
5	Electric and magnetic dipoles	TE	Closure of bandgap	Chain of nanobricks w_x: 260 nm w_y: 450 mn w_z: 220 nm	1400 nm

Figure 1.6: Summary table of the contents of each chapter.

The advanced investigation carried out during this Thesis required multiple numerical, fabrication, and characterization tools. Therefore, I did my research in collaboration with a group of researchers who performed numerical multipolar decompositions (Dr. Ángela I. Barreda), near-field measurements (Dr. Thomas Bauer, Dr. Elena Pinilla-Cienfuegos), calculation of the Q factor in a periodic chain (Dr. Alessandro Pitanti), and sample fabrication (Dr. Amadeu Griol). The author has fully performed the FDTD and CST simulations, the preparation of the samples and the experimental set-up, and the experimental measurements of far-field scattering and transmission, and has collaborated in the sample fabrication process.

Chapter 2

Observation of the first-order anapole state in silicon disks driven by integrated waveguides

Contents

2.1 Introduction

As discussed in Chapter 1, high-index nanoparticles support radiationless states called anapoles, where dipolar and toroidal moments interfere to inhibit scattering to the far field. In order to exploit the properties arising from these interference conditions in photonic integrated circuits, the particles must be driven in-plane via integrated waveguides. Although many previous works have addressed the existence of anapole states in high-index spheres, the most simple photonic nanostructure that can support such state in planar photonic integrated circuits is the disk. In contrast to the case of large - in terms of wavelengths - disks, supporting whispering gallery modes in which light propagates around the disk, the response of subwavelength- and wavelength-scale disk to incident radiation will be dominated by Mie resonances. As a result, interference from such Mie resonances can lead to the mentioned anapole states.

In this chapter, we addressed via numerical simulation and experiments the excitation of the first electric anapole state in silicon disks when excited on-chip at telecom wavelengths. To this end, we have used silicon waveguides to excite the disk whilst top scattering has been collected to observe the presence of such states. As shown below, we have found that the anapole condition — identified by a strong reduction of the top (or out-of-plane) scattering — does not overlap with the near-field energy maximum in

contrast to the case of normal illumination, an observation attributed to retardation effects. We experimentally verified via far-field and near-field measurements the two distinct spectral regions corresponding to scattering minimum and energy maximum in individual disks illuminated in-plane from closely placed waveguide terminations.

To start with, we analyzed both numerically and experimentally the in-plane realization of an anapole state in individual silicon disks driven by the fundamental transverse electric (TE) mode of a silicon waveguide, so that the incident light travels normal to the disk axis. To study the near-field patterns, as well as the far-field scattering under both out-of-plane and in-plane illumination, we used numerical simulations. In collaboration with Dr. Ángela Barreda we calculated the multipolar moments for both cases. These simulation results showed a wavelength blue-shift of the electric anapole condition (identified as the wavelength for which the ED and toroidal moments cancel each other in the far field) for in-plane incidence in comparison to the usual normal incidence case. We attribute this phenomenon to retardation effects due to the wavelength-scale size of the disk along the illumination direction. More importantly, this additionally results in a decoupling of the minimum in the far-field scattering and the maximum of energy localization in the disk, which take place at well separated wavelengths for in-plane excitation.

To corroborate this observation, we conducted far-field experiments of fabricated samples (see detailed in Appendix C) recording out-of-plane scattering of different individual disks (excited by waveguides) and observe a strong reduction of the scattering in the wavelength region where the anapole condition is predicted to occur. Moreover, in collaboration with the research group led by Kobus Kuipers at DELFT University of Technology, we report, on NSOM experiments that illustrate the typical dual-vortex near-field pattern attributed to anapole states as well as a strong energy concentration at wavelengths red-shifted to the anapole condition, in agreement with the numerical simulations. Our results highlight important differences between anapole states when the particles are illuminated from different directions and have direct implications to the use of wavelength-size disks in high-index PICs for applications ranging from biosensing to nonlinear signal processing.

2.2 Scattering and multipolar response of silicon disks under normal and in-plane illumination

We start our study by calculating the scattering of light by a single silicon disk surrounded by air. We fix the disk thickness to $t = 220$ nm, which is the usual silicon thickness in commercial silicon-on-insulator wafers, while the radius r can be varied to tune the particular contribution of each multipolar moment at a certain wavelength [52]. Indeed, by properly choosing the dimensions of the disk, the destructive interference between the in-plane ED and the toroidal moments can be tuned to a specific spectral region (in our case: the experimentally accessible region of $\lambda = 1260$ - 1630 nm for far-field measurements). We consider two directions of incidence of the incoming wave: it can be either parallel (out-of-plane excitation) or perpendicular (in-plane excitation) to the disk axis, as shown in Fig. 2.1**a,d** respectively. For the latter, we consider that the electric (magnetic) field of the excitation wave is perpendicular (parallel) to the disk axis. The contributions to the scattering cross-section of the main multipole moments (Cartesian electric $\mathbf{p}$, magnetic $\mathbf{m}$, quadrupolar electric Q_{ele} and quadrupolar magnetic Q_{mag}, together with their respective toroidal moments ($\mathbf{T}$) for the case of the dipolar

electric, dipolar magnetic and quadrupolar electric modes), are shown in Fig. 2.1**b,e** for out-of-plane excitation and in-plane excitation, respectively.

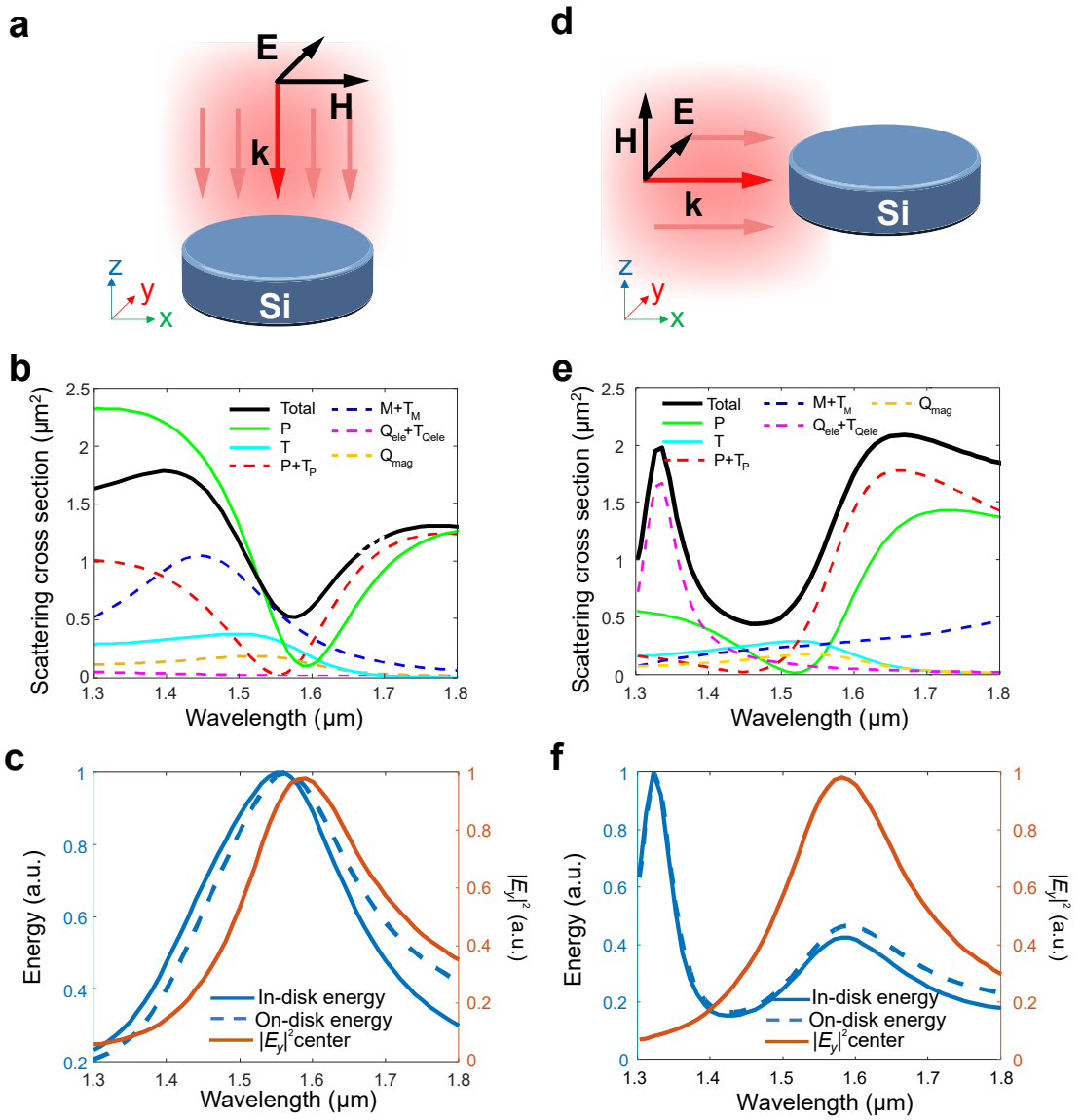

Figure 2.1: Optical response of a thin silicon disk in air. The direction of incidence of the incoming plane wave can be either parallel (**a-c**) or perpendicular (**d-f**) to the disk axis. The spectral contribution of the main Cartesian multipolar terms (electric dipole (**p**), magnetic dipole (**m**), electric quadrupole (Q_{ele}), magnetic quadrupole (Q_{mag}) and their respective toroidal moments for the electric dipole, magnetic dipole and electric quadrupole modes, represented by **T** to the scattering cross-section is shown in **b** and **e** for each case. The total scattering cross-section is represented in black. The spectra representing the energy inside the disk and on the disk surface, as well as the electric-field intensity at the disk center for each configuration are depicted in **c** and **f**, respectively. The disk dimensions are $r = 350$ nm and $t = 220$ nm.

It can be seen that the anapole condition — this is, $|\mathbf{p}| = |-1k\mathbf{T}|$, where k is the wave

number — is satisfied for both configurations. However, it occurs at significantly different wavelengths (1555 nm for out-of-plane incidence, and 1444 nm for in-plane incidence), which — at first glance — is a surprising fact when we consider that the dimensions of the disk are the same and the incident electric field is normal to the disk axis in both cases. Another remarkable difference arises when looking at the energy stored in the disk, which is directly related to the intensity of the electric field. While for normal incidence, the energy and electric-field intensity maxima are observed close to the anapole condition (Fig. 2.1**c**), in agreement with previous works [50,52,65–68], for in-plane incidence these magnitudes are red-shifted to wavelengths around 1600 nm, as depicted on Fig. 2.1**f**. This means that the absence of scattering is no longer linked to a maximization of the energy stored (or electric-field intensity) in the disk, as it happens under normal incidence (this is, in experiments with FS excitation and collection). Regarding the quadrupolar terms, although this scattering is in general smaller than the one coming from the dipolar terms, it becomes predominant around the anapole region, preventing a complete cancellation of the disk scattering. However, in our experimental realization, we measure the scattered far field along the disk axis and in this direction — which we call top scattering — the contribution from the quadrupolar terms should be negligible, thus allowing us to determine the anapole condition, as shown below.

We explain this discrepancy between energy maximum and scattering minimum by considering that the disk has a non-negligible size (the diameter is roughly half of the involved wavelength at the anapole condition) in the propagation direction for in-plane incidence. Therefore, retardation effects are not negligible anymore and should play a role by largely modifying the response of the disk with respect to the normal incidence case [91,92]. For normal incidence (and a thin disk), we excite the in-plane eigenmodes of the disk without phase retardation between different lateral points of the disk, while for in-plane incidence the retardation of the excitation field between different lateral points in the disk means the quasi-static approximation does not hold anymore. Similar to effects shown in plasmonic particles [93,94] the resonance frequencies will thus shift, leading to a wavelength shift of the anapole condition. We calculated the anapole and maximum-energy wavelengths for different disk radii, keeping the thickness equal to 220 nm. As shown in Fig. 2.2**a,b**, the anapole and maximum-energy wavelengths almost coincide for normal excitation, except for some specific radii such as around $r = 275$ nm, due to the contribution of other multipolar moments to the energy storage inside the disk, as shown in multipolar simulations not shown here for the sake of simplicity. However, for in-plane incidence, both conditions (anapole and energy maximum) are decoupled. Moreover, the wavelength spacing between them grows proportional to the disk dimensions, which supports our argument on the retardation effects. Furthermore, we likewise observed this effect when calculating both wavelengths for disks having the same radius but different thicknesses (Fig. 2.2**c**). Indeed, in this case, the decoupling of the two conditions is also evident under normal incidence for sufficiently thick disks. Indeed, this supports our explanation: the decoupling is not caused by the direction of incidence and the shape of the disk in that direction, but merely by the thickness of the nanoparticle along the propagation direction.

Besides these observations, some differences can additionally be seen in the near-field patterns depicted in Fig. 2.2**d,e**. For normal incidence (Fig. 2.2**d**), the typical pattern with three maxima and two nodes of the electric field (forming the expected vortices of the electric field) is observed. In the case of the anapole state under in-plane incidence (Fig. 2.2**e**), these features also appear, but the electric-field is not as well confined in

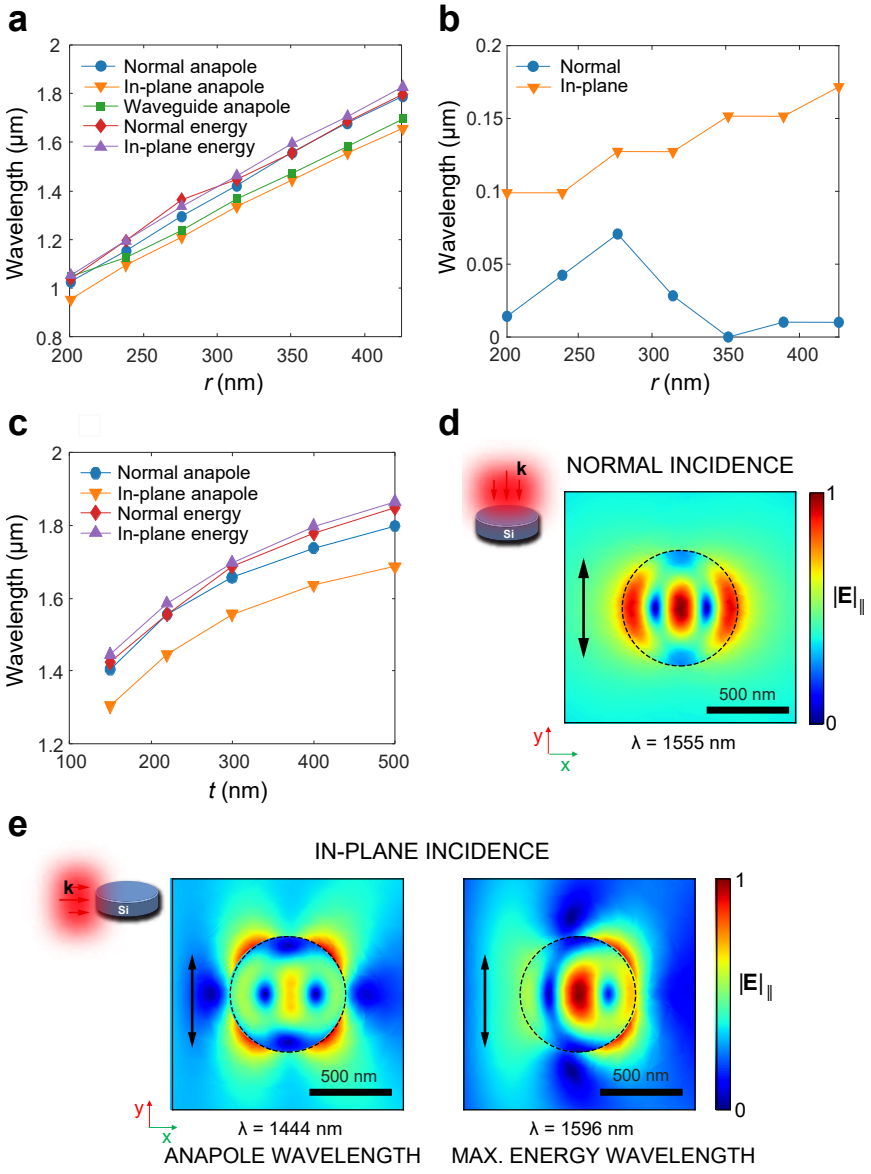

Figure 2.2: Spectral evolution of the anapole condition at normal and in-plane incidence. **a** Anapole-condition and maximum-energy wavelengths for normal and in-plane incidence as a function of the disk radius r. The wavelength at which a minimum of the out-of-plane scattering is observed under waveguide illumination is also shown. **b** Wavelength difference between the energy maximum and the anapole for the cases represented in **a**. **c** Anapole-condition and maximum-energy wavelengths for normal and in-plane incidence as a function of the disk thickness t for a fixed silicon disk radius r=350 nm. Calculated electric-field amplitude patterns in a disk of $r = 350$ nm at the relevant wavelengths for both **d** normal and **e** in-plane incidence. The black arrows indicate the polarization direction of the incident electric field. The calculations have been performed by dr. Ángela Barreda using COMSOL Multiphysics [95].

the disk. Instead, we observe four external field maxima surrounding the disk at the azimuthal positions $\pi/4$, $3\pi/4$, $5\pi/4$, and $7\pi/4$. When considering the field pattern

at the maximum-energy wavelength, we observe that the electric field concentration inside the disk increases considerably. The two electric-field vortices are still present, but there is a strong asymmetry between them, with the first one being partly obscured by the incident field while the second one is dominating the field distribution. Still, the signature of the toroidal excitation is present in the energy maximum, as can be expected due to the broadband character of this resonance.

2.3 In-plane excitation of an isolated silicon disk: numerical simulations

To achieve in-plane (or on-chip) excitation of the silicon disk, we consider a rectangular cross-section silicon waveguide of width w ended abruptly by a flat termination and spaced by a gap g from the disk boundary (Fig. 2.3).

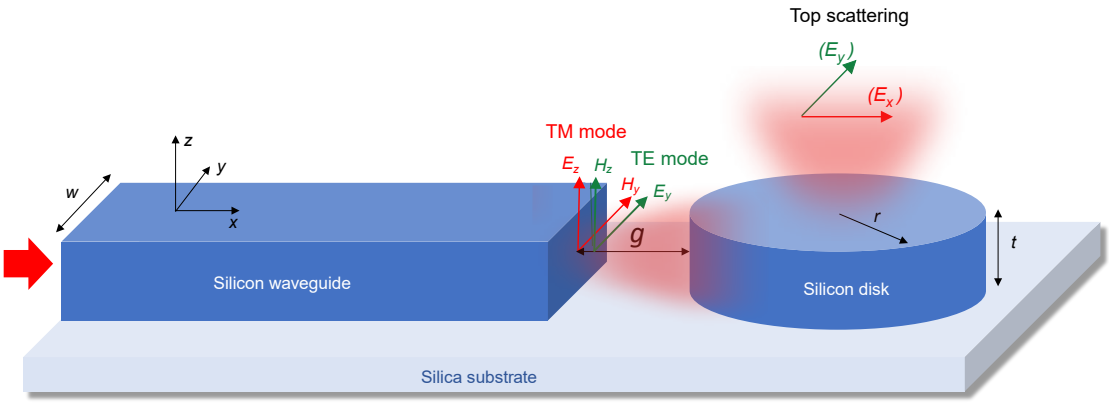

Figure 2.3: Sketch of the in-plane excitation of a silicon disk (radius r, thickness t) from a waveguide (width w) end propagating either the TE or the transverse magnetic (TM) mode. The main electric field components for each mode are depicted. The waveguide end and the disk are spaced by a gap g. The excited electric (magnetic) state scatters light mostly polarized along the y (x) direction. This structure can be fabricated in SOI wafers using mainstream silicon nanofabrication tools. The silica substrate, which ensures physical stability of the PICs, will red-shift the overall response of the system as part of the field penetrates a region with a refractive index slightly larger than 1.

Here, the silicon waveguide and the disk are placed on a silica substrate, which breaks the vertical symmetry and whose main effect will be to red-shift the overall response of the disk. A similar configuration was used in previous works to excite individual plasmonic nanostructures via integrated waveguides [27, 28]. Notice also that a similar waveguide-disk configuration was proposed to extract light generated internally in the disk via near-field coupling [70], while here we choose a gap $g = 600$ nm where no significant near-field interaction between waveguide and disk remains. By coupling light to the TE like mode of the waveguide (the main component of the electric field is in-plane) from the left side, light exiting from the waveguide end will excite the disk mainly via an in-plane electric field E_y and an out-of-plane magnetic field H_z. Note that the tight field confinement of the waveguide will also result in the existence of longitudinal components of the fields (E_x, H_x) [27, 31, 96] that also contribute to the disk excitation

because of the proximity of the waveguide termination and the disk boundary ($g < \lambda$). In principle, the contribution of such terms should be much smaller than the transversal ones, but the overall picture will be slightly different from the plane-wave case considered in the previous calculations.

We performed numerical simulations with RSoft Bandsolve [97] (Finite-difference time-domain FDTD) and CST Microwave Studio [98] to verify that the anapole state can be also excited from the waveguide end. First, we removed the substrate to mimic closely the case with FS excitation addressed above. The near-field patterns shown in the field maps in Fig. 2.4, which shows the electric field lines under waveguide illumination for three relevant wavelengths when the silica substrate is removed, look quite similar to the ones presented in Fig. 2.2**e** for FS lateral illumination. For instance, they evidence the formation of three main lobes of the electric field, which confirms the capability of our approach to excite the anapole state.

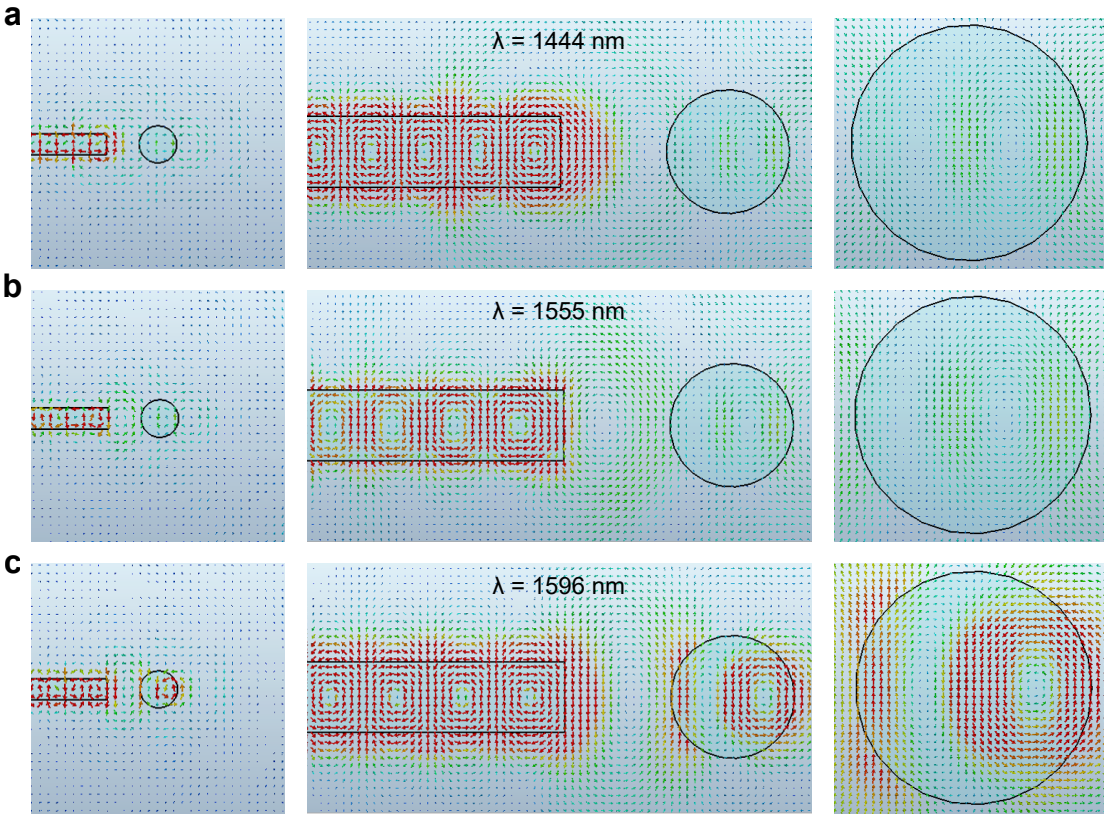

Figure 2.4: Simulations of the electric field lines (represented by arrows) of a $r = 350$ nm disk illuminated from a waveguide (in-plane driving) at three representative wavelengths: **a** anapole state for in-plane illumination, **b** anapole state for normal illumination and **c** energy maximum under in-plane illumination. Simulations performed with CST Microwave Studio.

We also performed numerical simulations (Fig. 2.5) with RSoft Bandsolve (FDTD) and CST Microwave Studio to demonstrate that the spectral response of the disk when illuminated from a nearby waveguide termination shows similar features as in the case of FS illumination addressed above.

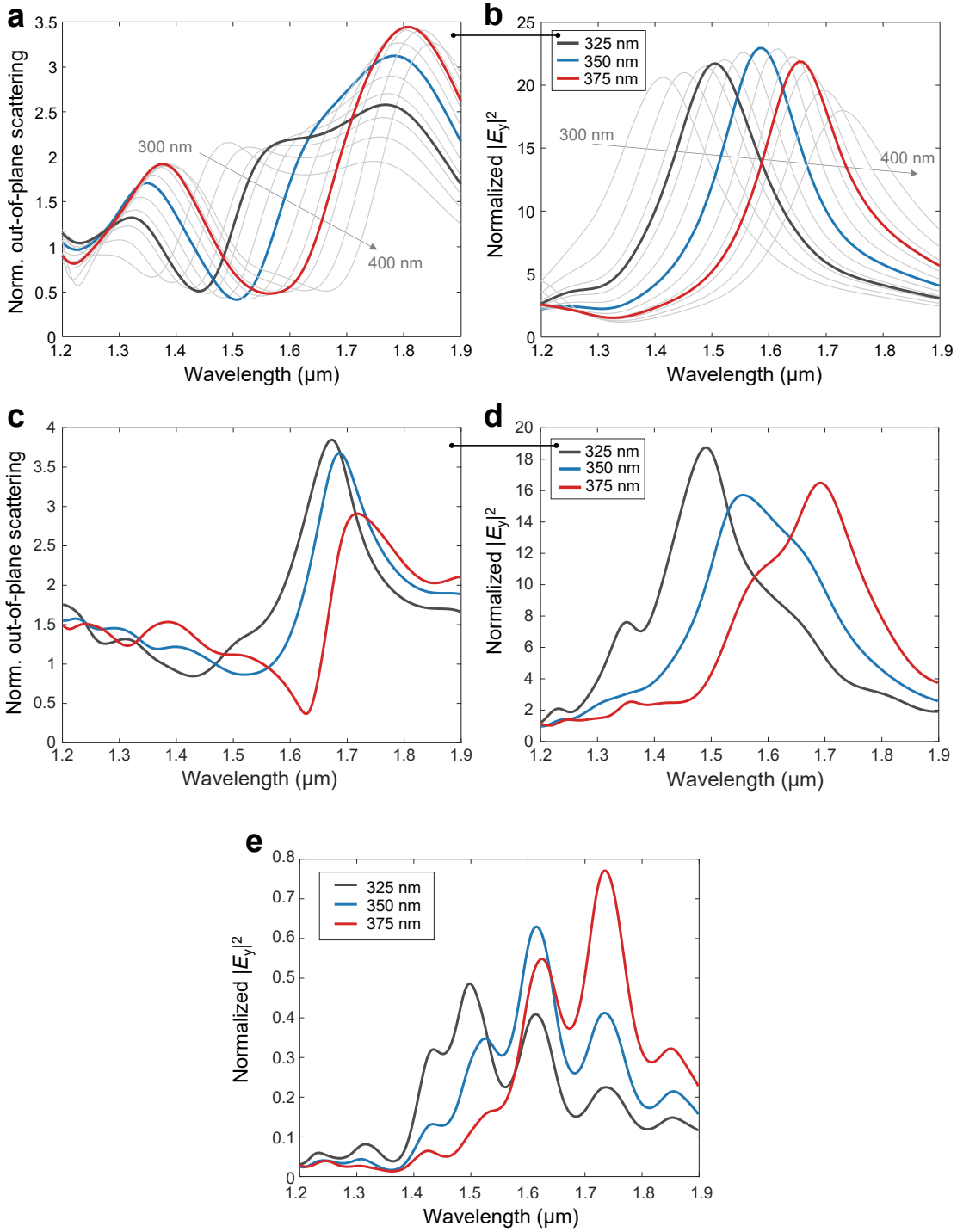

Figure 2.5: **a** 3D-FDTD simulations of the normalized out-of-plane scattering and **b** the electric-field intensity $|E_y|^2$ at the disk center for disk's radius r varying between 300 and 400 nm (325, 350, and 375 nm in color and the rest in 10 nm steps in gray as visual guide). **c** CST simulations of the normalized out-of-plane scattering and **d** the electric-field intensity $|E_y|^2$ at the disk center for disk's radius r varying between 325 and 375 nm. Normalization is performed by comparison with the same case without the silicon disk. **e** Same case as **d** but normalized with respect to the field in the center of an isolated waveguide.

Figure 2.5 shows (**a,b**) 3D-FDTD and (**c,d**) CST simulations of the normalized out-of-plane scattering and electric-field intensity spectra under waveguide illumination as a function of the disk radius. The results do not come out exactly the same due to the boundary conditions used in each simulation tool. But, as expected, increasing the disk radius red shifts both the anapole and maximum energy wavelengths, which confirms that both the anapole condition and the energy maximum can be carefully tuned over the whole telecom wavelengths window. Additionally, these results show that the scattering minimum and the energy maximum take place at different wavelengths regardless of the radius of the disk.

In the previous results, the calculated values have been normalized with respect to the same scenario without disk to account for the effect of the waveguide: in the case of scattering, since the field has been monitored at a distance of 2 µm from the disk top surface, we remove the effect of the evanescent field of the TE mode; in the case of the electric-field intensity in the disk center, we eliminate the effect caused by the field diverging at the waveguide output. Note that here the scattering is monitored only along the vertical axis ($\theta = 0°$), that is, we are calculating the out-of-plane scattering. This is a good approximation to pinpoint the anapole condition since only the ED and the toroidal moment will contribute to the scattering along that direction.

In the fabricated samples, both the waveguide and the disk need to rest on a silica substrate. We therefore considered the effect of the silica substrate on the features shown by the silicon disk when illuminated. As shown in Fig. 2.6, the presence of the substrate red shifts the anapole condition (scattering minimum in the far field), as can be expected since the refractive index of the whole system increases. However, the maximum energy wavelength remains virtually the same, which can be understood by considering that the field is strongly confined inside the disk and does not feel the presence of the substrate. Thus, this near-field property remains unchanged when introducing a substrate with moderate refractive-index contrast to the disk.

We also calculated the energy above the disk (Fig. 2.1**f** for FS illumination and Fig. 2.6 for waveguide illumination), which shows that the energy maximum at that plane coincides with the energy maximum inside the disk. This is an important point to be considered for the application of anapole states in nanophotonic sensors, as well as for the near-field measurements detailed below, where the energy is measured on the top surface of the disk.

Finally, we analyzed the near-fields in the disk in the presence of substrate via CST Microwave Studio simulations. As in the case of the structure completely surrounded by air, we considered the wavelength at which the more relevant features are observed. Noticeably, the near-field patterns are also quite similar when the substrate is added in the simulations (see Fig. 2.7). Indeed, the near-field patterns at the red-shifted wavelengths look almost identical for the energy maximum wavelength, while some discrepancies arise at the anapole condition wavelength. This can be explained by the presence of the substrate that breaks the system's mirror symmetry in the vertical direction. The substrate effect is more pronounced at the anapole condition, since the fields are not as strongly localized in the disk and are more perturbed due to the change of the refractive index below the disk. This essentially means that our driving scheme imitates the case of a disk illuminated laterally with a light beam propagating through FS.

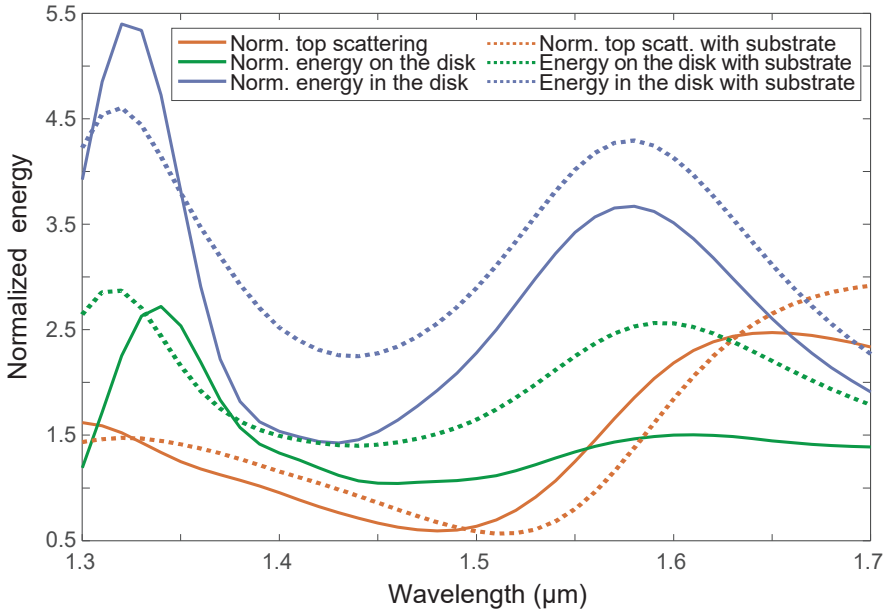

Figure 2.6: Numerically calculated energy inside the disk ($r = 350$ nm), at 50 nm spacing on top of the disk and at 2 µm distance from the disk with and without silica substrate. The latter metric is considered to be a good approximation of the scattered field. Illumination is in-plane from the waveguide end excited by the TE-like mode.

2.4 Far-field scattering measurements of the on-chip silicon disk

To confirm these numerical predictions, samples containing sets of waveguide-disk circuits were fabricated on a SOI chip using standard fabrication tools (details are described in Appendix B) as Fig. 2.8 shows. Each individual circuit (see Fig. 2.8) includes a 3 mm long input waveguide, whose initial width (3 µm) is chosen to maximize the coupling efficiency to an external lensed fiber in an end-fire coupling approach, and which is adiabatically narrowed down to $w = 400$ nm ending abruptly, and a silicon disk. We also fabricated structures without disk to normalize the top scattering response.

The microscope objective of the measurement system allowed us to record the field intensity scattered from the circuit in normal direction, separating the radiated emission from the regions highlighted with red squares (see Fig. 2.9 for the second group of the fabricated samples). Notice that the use of an objective with finite numerical aperture will result in collecting light propagating inside a cone with half-opening angle of $\Delta\theta = 5°$ around the z-axis ($\theta = 0°$), thus producing a residual background coming from multipolar terms different to the electric and toroidal dipoles.

Figure 2.10 shows the measured normalized out-of-plane scattering for three different disks having nominal radii of 325, 350, and 375 nm. When analyzing the measured scattering response, we observe that it presents some discrepancies with that obtained in simulation (Fig. 2.5). In particular, we appreciate a shift in the vertical axis so that in one of the samples (radius 350 nm) the normalized scattering minimum does not reach values below 1. We attribute this to the fact that the structures with and without disk are completely independent, so the coupling losses are different for each one and when normalizing we were not sure that the vertical axis (scattering response) was correct.

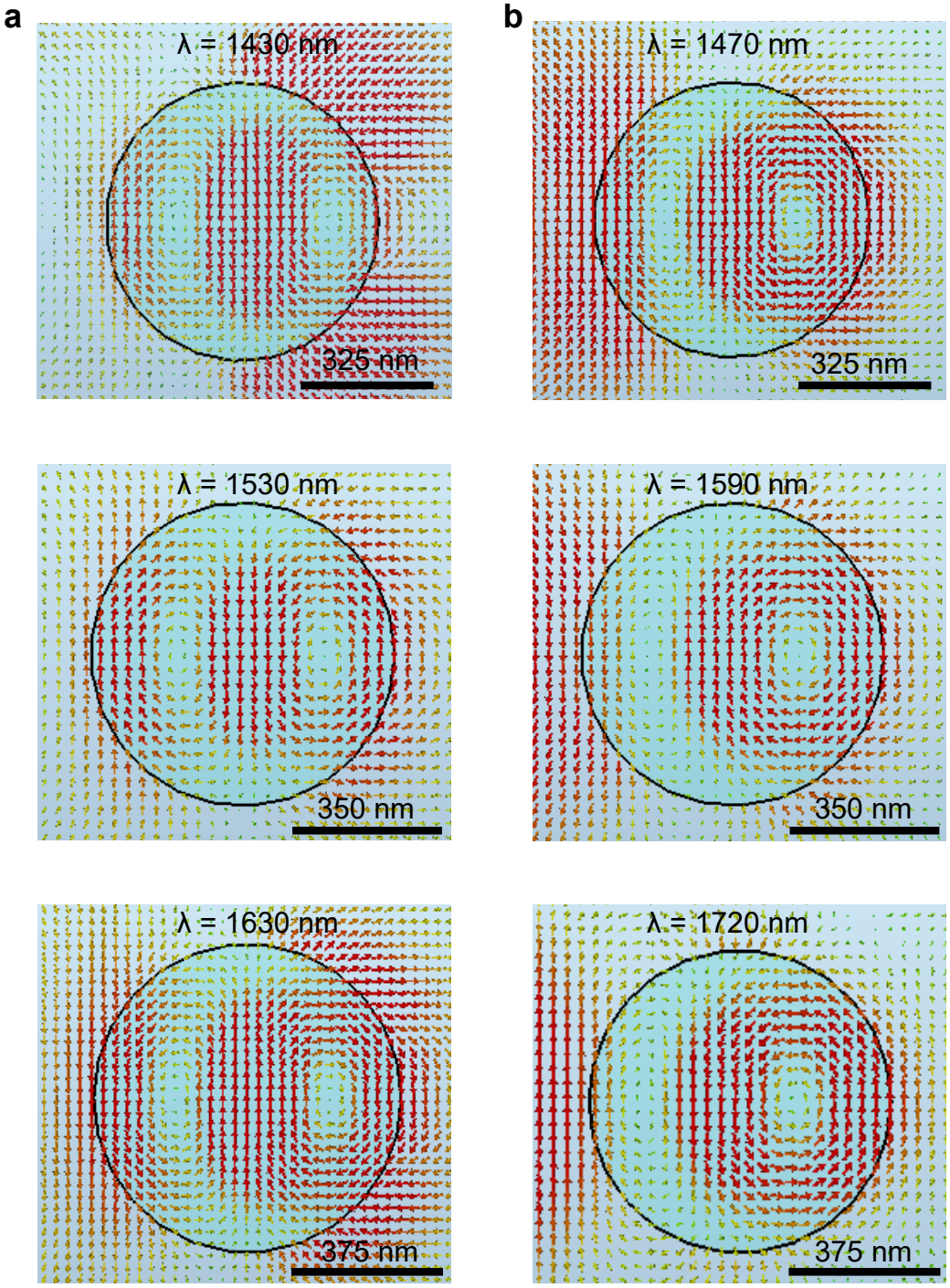

Figure 2.7: **a** Electric-field lines (represented by arrows) at the anapole and **b** maximum-energy wavelengths under waveguide illumination for a $r = 325$ nm (top row), 350 nm (middle row) and 375 nm (bottom row) disks with waveguide width $w = 420$ nm and gap $g = 600$ nm, with the system placed on a silica substrate. The wavelength have been obtained from simulations and show the expected red-shit with respect to the no-substrate case. Simulations performed with CST Microwave Studio.

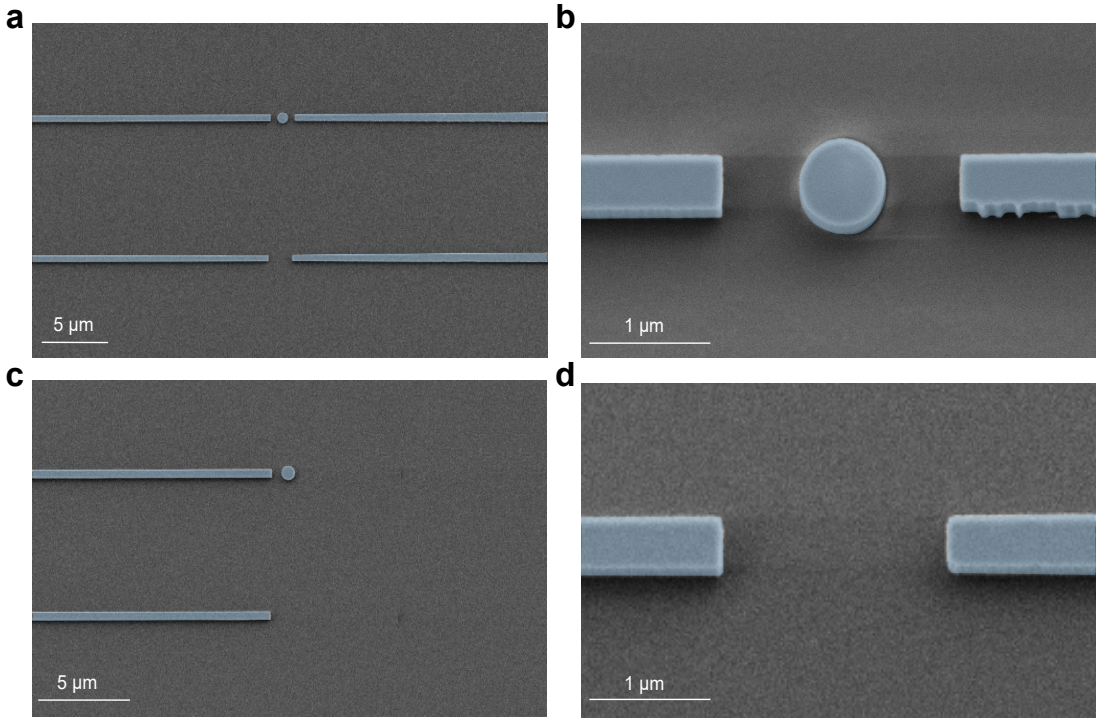

Figure 2.8: Scanning electron microscope (SEM) pictures of some fabricated circuits. **a,c** Structures with and without output waveguide respectively. **b,d** Details of structures with and without disk.

Due to this reason, two new samples were fabricated. Each individual circuit includes now a 3 mm long input waveguide, with initial width $w = 3$ µm which is adiabatically narrowed down to w= 420 nm. Then a 3-dB Y-splitter is inserted to split the input signal into two paths ended in an abruptly terminated waveguide, with a silicon disk patterned in only one of the paths. Figure 2.11 shows SEM images of a fabricated circuit, highlighting in detail the waveguide end acting as an excitation port as well as the disk. This configuration allows to have the same coupling losses for the structures with disk and without disk, thus enabling a correct normalization, removing the vertical shift noted above in Fig. 2.10.

Figure 2.12 shows the measured normalized out-of-plane scattering for three different disks having nominal radii of 325, 350, and 375 nm. Notice that the far-field scattering is not spatially tailored, in contrast to other integrated approaches such as the one demonstrated in [99]. The scattering responses, are qualitatively similar to the ones obtained in simulation (Fig. 2.5). In particular, there is a region with reduced scattering coincident with the predicted anapole condition. The scattering is, indeed, smaller than for the case of the terminated waveguide without disk (in other words, normalized scattering < 1, going even below 0.5 at some wavelengths, in agreement with numerical simulations), which means that not only the scattering is well suppressed, but also that the excitation of the ED and toroidal moments corrects the divergence of the beam exiting the waveguide termination and contribute to reduce the overall scattering out of the chip. Note that, as mentioned above, the excitation field is not a plane wave. This fact, together with the presence of the substrate makes that the normalized scattering

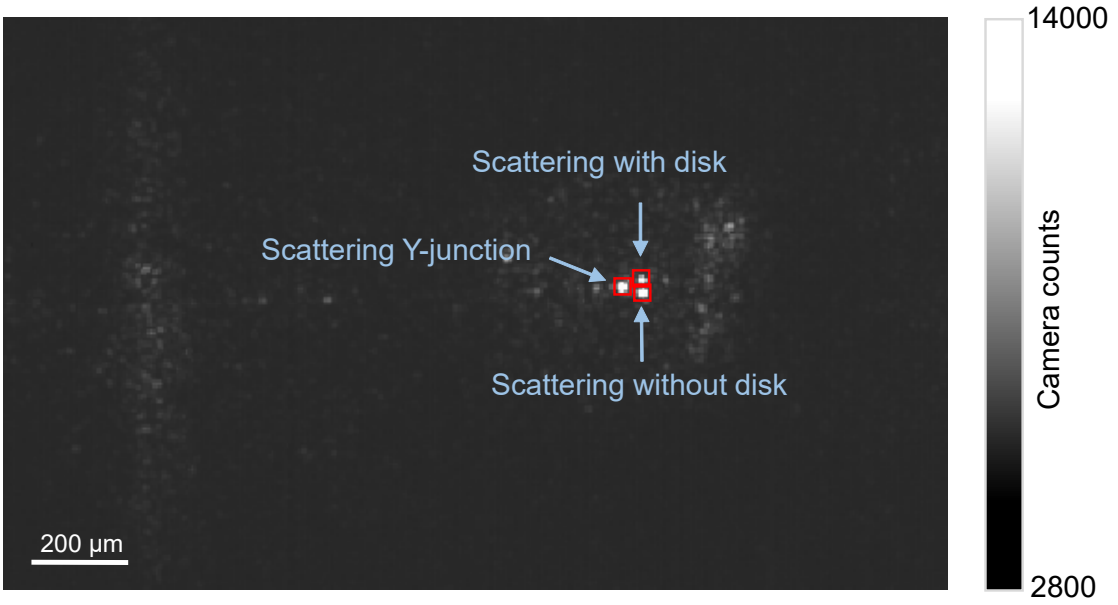

Figure 2.9: Image recorded with the infrared camera in the far-field measurements showing the spot corresponding to the Y-splitter, the waveguide termination with disk and the waveguide termination without disk.

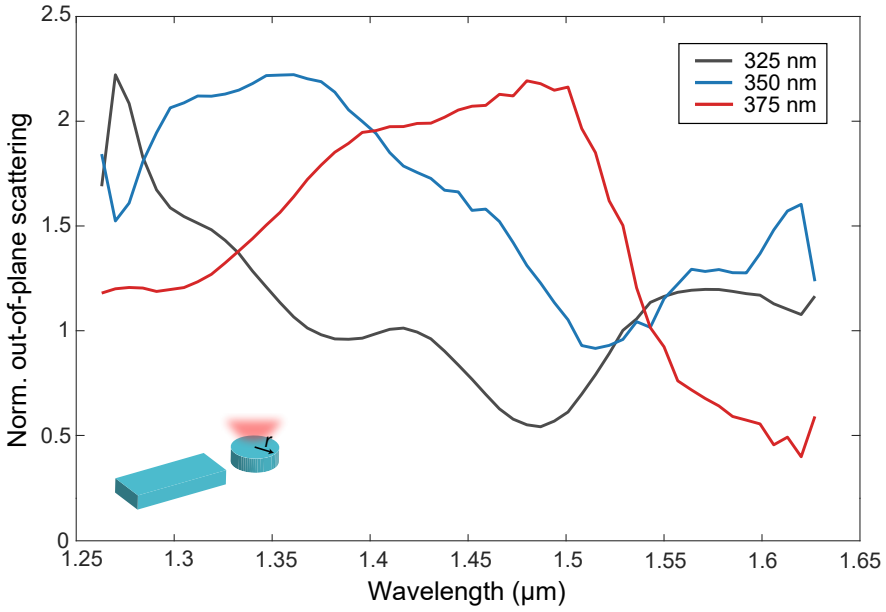

Figure 2.10: Experimental results of the out-of-plane scattering normalized to the value for a bare waveguide termination, recorded for disks with different radii (nominal values shown in the figure).

becomes lower than unity around the anapole condition, in contrast to the plane-wave illumination case when the residual normalized scattering would be equal to one.

The differences in the position of the scattering minimum for the two samples is

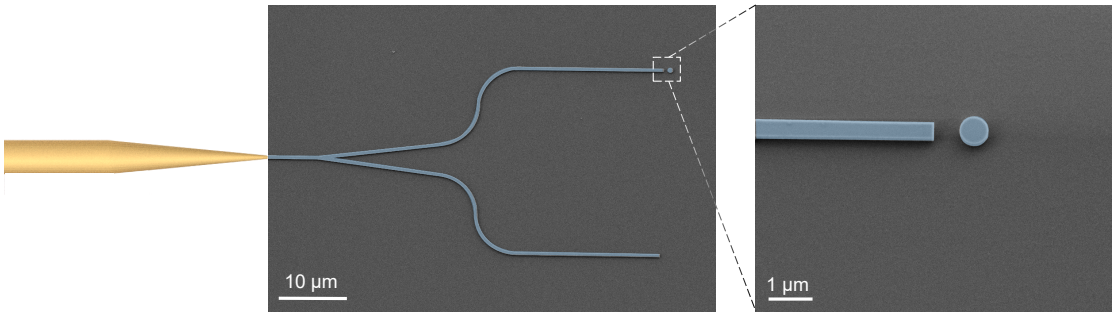

Figure 2.11: SEM picture of one of the fabricated circuits, showing the input waveguide (with an external lensed fiber sketched), a Y-splitter, and two waveguides, both ended in an abrupt termination, and one of them having a disk (nominal disk radius $r = 350$ nm) close to the termination. Inset: Close view the disk and the waveguide termination.

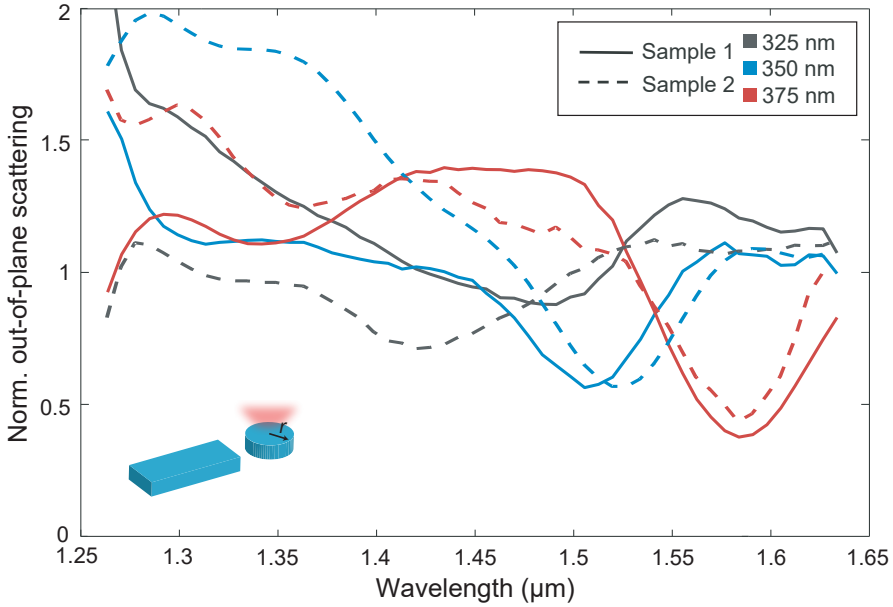

Figure 2.12: Experimental results of the out-of-plane scattering normalized to the value for a bare waveguide termination, recorded for disks with different radii (nominal values shown in the figure) in two different samples.

caused by the different radii in the fabricated samples. Indeed, the radius of the fabricated disks was about 5% smaller than the nominal values due to overetching (see details in Appendix B). However, a significant deviation to the scattering response shown in Fig. 2.5 is observed for the disk having a nominal radius $r = 325$ nm in Sample 1. Despite the estimated disk axes being only slightly different to the ones in Sample 2 (see Appendix B), we observe a significant red-shift of the scattering minimum. This scattering curve is also slightly top-displaced in comparison with the other responses. While we did not detect any large debris via SEM inspection, both observations together hint at potential minor fabrication irregularities or lithographic resist residue close to this specific disk being responsible for the higher scattering and spectral shift. Still, the

possibility to tune the anapole state by changing the radius is clearly demonstrated from these measurements.

2.5 Near-field measurements

In addition to the observed far-field scattering minimum, we experimentally verify the predicted dual-vortex structure of the anapole state as well as the numerically found decoupling of the minimum scattering condition and maximum-energy enhancement (Figs. 2.13 and 2.14) in the silicon disk by performing phase- and polarization-resolved near-field microscopy [100] on one of the samples (Sample 2) used in the far-field measurements (see Fig. 2.12).

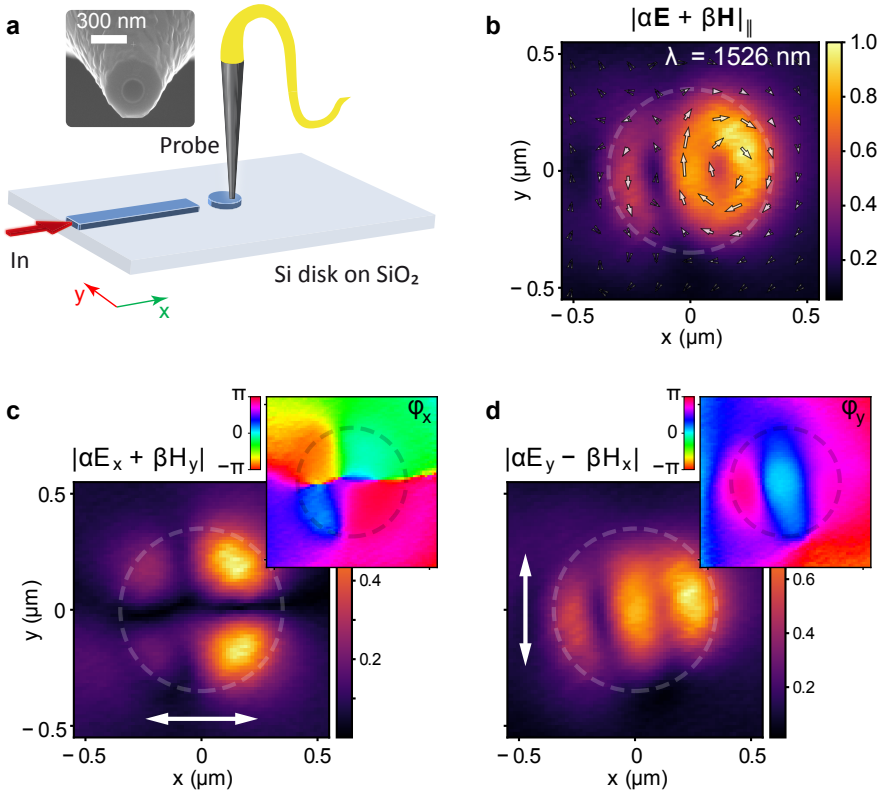

Figure 2.13: Phase- and polarization-resolved near-field measurements. **a** Sketch of the experimental set-up, utilizing an aperture-based near-field probe (see inset). **b** Near-field map of the normalized in-plane field amplitude as well as time-instantaneous field orientation (represented by white arrows) collected 30 nm above a silicon disk of nominal radius 375 nm (highlighted by the white dashed outline) at the wavelength of maximum near-field energy. **c** $|\leftrightarrow\rangle$ field map, consisting of a coherent sum of E_x and H_y, with the detected phase distribution shown as inset. **d** $|\updownarrow\rangle$ field map, consisting of a coherent sum of E_y and $-Hx$ as well as its phase distribution. The white arrows indicate the collected in-plane polarization direction. Both maps are normalized to the maximum field amplitude in **b**. Credit: Dr. Thomas Bauer, Delft University of Technology (The Netherlands).

We utilize an aperture-based near-field probe consisting of an aluminum-coated ta-

pered optical fiber (see inset in Fig. 2.13**a**) with an opening of 175 nm, and raster-scan the probe over the disk of nominal radius $r = 375$ nm from Sample 2 of Fig. 2.12 (actual radius measured via SEM: $r = 355$ nm), 30 nm above its top surface (see Fig. 2.13**a**, as well as Appendix D for additional details). With such a near-field probe collecting both, in-plane electric and magnetic field components [101], we extract near-field amplitude maps of the excited mode structure in the silicon disk (see Fig. 2.13**b** for a wavelength of $\lambda = 1526$ nm). The response of the near-field probe to the electric and magnetic field components is here given by the coupling coefficients α and β, respectively (see Appendix D and ref. [101]). Being able to not only detect the amplitude but also local phase and in-plane polarization information of the near-field (Fig. 2.13**c,d**) furthermore allows us to visualize the time-instantaneous field distribution, shown as white arrows in Fig. 2.13**b** for one given snapshot in the field's optical cycle.

The extracted full near-field information confirms the predicted dual vortex in the polarization structure of the mode inside the silicon disk at wavelengths around the anapole condition, while also highlighting the distinct difference to the symmetric field distribution of the anapole state under normal incidence.

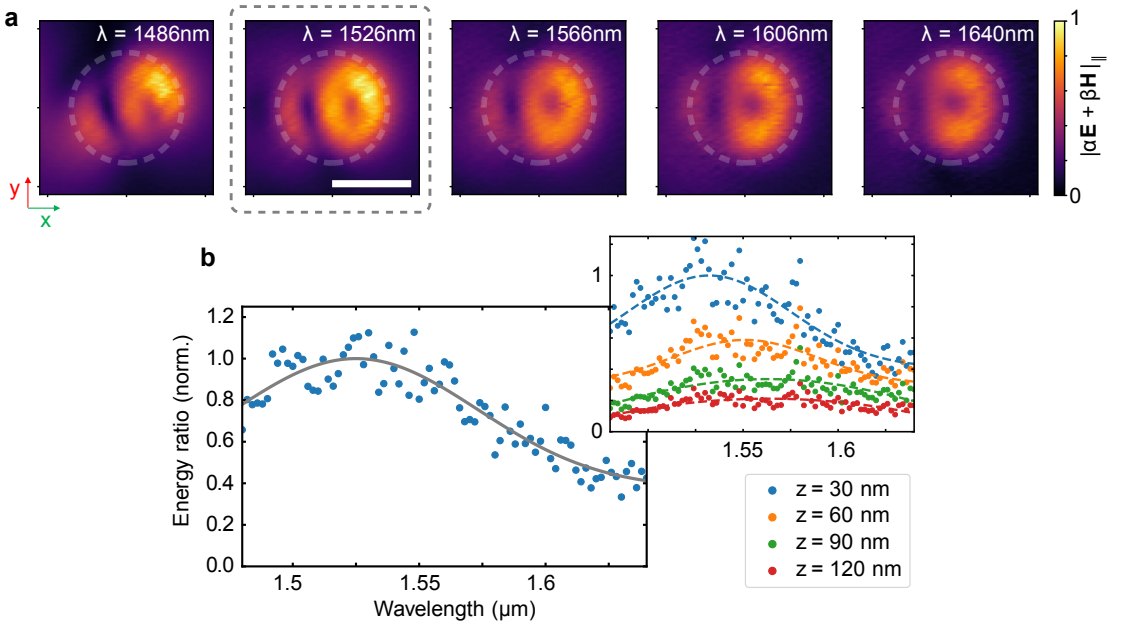

Figure 2.14: Wavelength-dependent near-field energy. **a** Near-field map of the in-plane field amplitude collected 30 nm above a silicon disk of nominal radius 375 nm (highlighted by the white dashed outline) in wavelength-steps of 40 nm around the point of maximum near-field energy (highlighted by a gray dashed box). The maps are normalized to the maximum field amplitude for the map of maximum near-field energy. **b** Spectral evolution of the near-field energy normalized to the emission of the feed waveguide. The gray line shows a Gaussian fit to the experimental data points. Inset: influence of the near-field probe on the spectral position of the energy maximum, highlighting the blue-shift when reducing the distance z between disk and probe [102], [103]. Credit: Dr. Thomas Bauer, Delft University of Technology (The Netherlands).

Sweeping the excitation wavelength between 1480 nm and 1640 nm in steps of 1 nm and scanning the resulting field distribution, we extract the near-field energy above

the disk's top surface by integrating for each wavelength over the area of the disk and normalizing to the mode energy emitted from the feed waveguide. For the disk with nominal radius of $r = 375$ nm, we see that the near-field maps over the full probed wavelength range (Fig. 2.14) exhibit the dual-vortex structure expected from the toroidal dipole moment, with the two vortex centers best visible at the wavelength of maximum energy at $\lambda = 1526$ nm, highlighted by a dashed gray line in the figure. The minor asymmetries observed in the collected field structures are an effect of the imperfect waveguide terminations, leading to a small tilt of the excitation wavefront, as confirmed by numerical simulations.

The energy ratio on top of the disk, normalized to its maximum value, is shown in Fig. 2.14**b**. The gray line corresponds here to a Gaussian fit to the experimental points shown in blue. The strong blue-shift of the maximum position with respect to the expected field maximum at $\lambda \approx 1600$ nm for the investigated disk is here caused by the coupling between the near-field probe and the silicon disk [102], [103]. This light-matter interaction is confirmed by collecting the near-field energy in the center of the disk at different heights above the disk surface, resulting in a successive blue-shift of the maximum-energy wavelength and collected energy enhancement as the probe is brought closer to the disk (see inset in Fig. 2.14**b**).

With everything seen in this chapter, it has been demonstrated that the first electric anapole state of an isolated silicon disk can be efficiently excited using an in-plane silicon waveguide as illumination source. This statement is supported by extensive numerical simulations (including multipole decomposition performed by Dr. Ángela Barreda) and experimental measurements in the far- and near-field regimes (these last measurements were done in the Delft University of Technology). In principle, our approach could also be valid to observe other anapoles resulting from the interference of higher-order multipolar moments in disks with higher aspect ratios (radius vs. wavelengths). The next step, which will be studied in the next chapter, is to achieve the observation of higher order anapole states using the same configuration.

Chapter 3

Observation of higher-order anapole states in silicon disks driven by integrated waveguides

Contents

3.1 Introduction

As already mentioned, anapole states naturally arise in high-index nanoparticles as a result of the interference between certain multipolar moments and are mainly characterized by a strong suppression of far-field scattering. In the previous chapter, the first-order electric anapole, resulting from the interference between the electric and toroidal dipoles, was characterized under in-plane illumination via an integrated waveguide as required in on-chip photonics.

In this chapter, we go a step further and analyze both numerically and experimentally the in-plane (on-chip) realization of the second-order electric and the magnetic anapole states in an individual silicon disk built in a PIC. The second-order electric anapole can be observed following the same procedure as in [104] - this is, using the TE waveguide mode to excite the transverse ED - but making the disk bigger in order to ensure that the targeted states take place at the wavelengths available in our laboratory. To this end, we increase the silicon thickness from the standard 220 nm thickness up to 350 nm, as well as, the disk radius, to place the anapole at the telecom wavelengths window where our laboratory instrumentation operates.

To observe signatures of magnetic anapoles, we have to address excitation of the magnetic field in the disk along the transversal direction, since an ideal vertical magnetic (which could be eventually excited using the TE waveguide mode) dipole does not

radiate out-of-plane. This can be achieved by using the TM mode of the driving silicon waveguide. As shown below, we observe strong dips - whose central wavelengths depend on the disk radius - in the far-field scattering spectra for the relevant polarization, which we consider a signature of the excitation of the targeted second-order electric and magnetic anapoles [76]. We also observe important differences between normal and in-plan excitation, remarkably for the second-order electric anapole, which we discuss in the text. Our results confirm the potential of this integrated approach to excite complex multipolar states in isolated high-index disks, opening new avenues to use anapole states in PICs.

3.2 Description of the system

Figure 2.3 displays a sketch of the structure used to observe the higher-order anapole states: an x-axis-oriented silicon waveguide with rectangular cross-section can propagate either its fundamental TE or TM mode characterized by its main field components E_{y} and H_{z} or E_{z} and H_{y}, respectively. The waveguide is abruptly terminated, and the output fields illuminating the disk (separated from the waveguide by a gap g) are essentially the same as in the waveguide [27]. Notice that guided modes are characterized by a main transverse component, but they also carry longitudinal field components [96] that are disregarded in this work for the sake of simplicity. Thus, the field exiting the waveguide can excite either the ED or the MD along the y-axis depending on the propagating waveguide mode (TE or TM, respectively). Ideally, an y-axis oriented electric (or magnetic) dipole will radiate in a doughnut-shape pattern so that the electric (or magnetic) far-field in the out-of-plane direction will be polarized along y (or x) [64]. Therefore, in analogy to the case of the electric anapole [104], detecting a reduction of the far-field scattering when measuring either the E_{y} or the E_{x} component could be interpreted as a signature of a second-order electric or a magnetic anapole state, respectively. Notably, the use of the TM mode also allows to excite the fundamental z-axis electric dipole but, in contrast to [76], this component will not radiate in the vertical direction, which makes easier to detect the magnetic anapole.

3.3 Numerical simulations

To analyze numerically the in-plane realization of the second-order electric and the magnetic anapole states in an individual silicon disk we performed simulations with COMSOL Multiphysics, RSoft Bandsolve and CST Microwave Studio.

3.3.1 Second-order electric anapole

We start our study by calculating the scattering properties of a single silicon disk surrounded by air. The effect of the substrate in the experiments will mainly consist on a red-shift of the whole optical response [104], as discussed in Chapter 2. We fix the disk thickness to $t = 350$ nm, which is thicker than the 220 nm value typical in SOI photonics but still available in commercial wafers. We choose a radius $r = 550$ nm and perform numerical simulations of the disk response upon normal and lateral illumination with the electric field along the x direction. This is, we follow the same strategy as in the case of the first electric anapole. Therefore, the lateral illumination mimics the scheme in Fig. 2.3 for the TE waveguide mode. The contributions to the scattering cross-section

of the main multipole moments (Cartesian electric **p**, magnetic **m**, quadrupolar electric Q_{ele} and quadrupolar magnetic Q_{mag}, together with their respective toroidal moments (**T**) are shown in Figs. 3.1**a** and **b** for normal and lateral illumination, respectively. It can be seen (Fig. 3.1**a**) that the second electric anapole condition - this is, $P+T_P = 0$ - is satisfied at a wavelength of 1475 nm under normal incidence. However, this condition is not met for lateral incidence (Fig. 3.1**b**). So, if for the first electric anapole, we identified a major difference between in-plane and normal incidence (the decoupling of the scattering minimum and energy maximum in the disk [104]), for the second electric anapole, the difference is even more noticeable, and there is neither a scattering minimum nor a dip in $P + T_P$ at the expected (from normal incidence simulations) anapole wavelength.

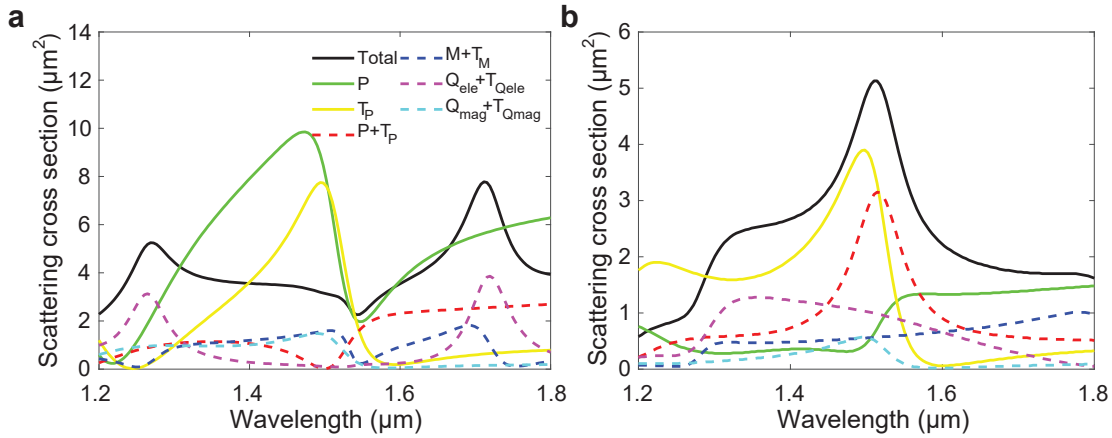

Figure 3.1: Spectral contribution under **a** normal and **b** lateral illumination of the dipolar electric (**p**) in red and magnetic (**m**) in blue, and quadrupolar electric (Q_{ele}) in purple and magnetic (Q_{mag}) in cyan moments, together with their respective toroidal moments, represented by **T**, to the scattering cross-section. Also, the individual contributions of the electric dipole (green), and its respective toroidal moment (yellow) to the scattering are represented. The disk dimensions are $t = 350$ nm and $r = 550$ nm.

As in the case of the first electric anapole, this behavior can be also attributed to retardation effects: the disk diameter is comparable to the wavelength, which may result in remarkably different scattering properties depending on the illumination direction. However, in on-chip photonics, the key requirement is to ensure minimum out-of-plane scattering (so that light remains in the PIC) whilst in-plane scattering can occur and even used to build - for instance - chains of disks for energy transport [71,77]. To verify if the scattering is reduced in the normal direction (parallel to the disk axis), we performed FDTD simulations and calculated the scattered E_y field along different directions. As shown in Fig. 3.2**a** there is a dip in the scattering response in the wavelength region where the electric anapole is predicted under normal excitation. This result also keeps when the disk is illuminated from the waveguide propagating the TE mode. As shown in Fig. 3.2**b**, the normalized top scattering (calculated as the ratio between the scattering with and without disk to remove the waveguide termination effect [104]) also displays a strong reduction in the expected wavelength region.

Notice also that the electric field inside the disk also displays a maximum at a wavelength slightly red-shifted compared to the scattering. This means that the decoupling of the minimum scattering condition and the maximum-energy enhancement (we assume

that the maximum energy takes place when the electric field in the disk center is maximized, as we observed in Chapter 2) also takes place for the second electric anapole. In this case, we represent the field maximum normalized with respect to the field in the center of an isolated waveguide. Remarkably, the enhancement is lower than in the case of the waveguide (normalized enhancement < 1). This means that the anapole state is not efficiently excited by the input waveguide, and strategies for a more efficient excitation need to be pursued if one wants to use this state in nonlinear applications.

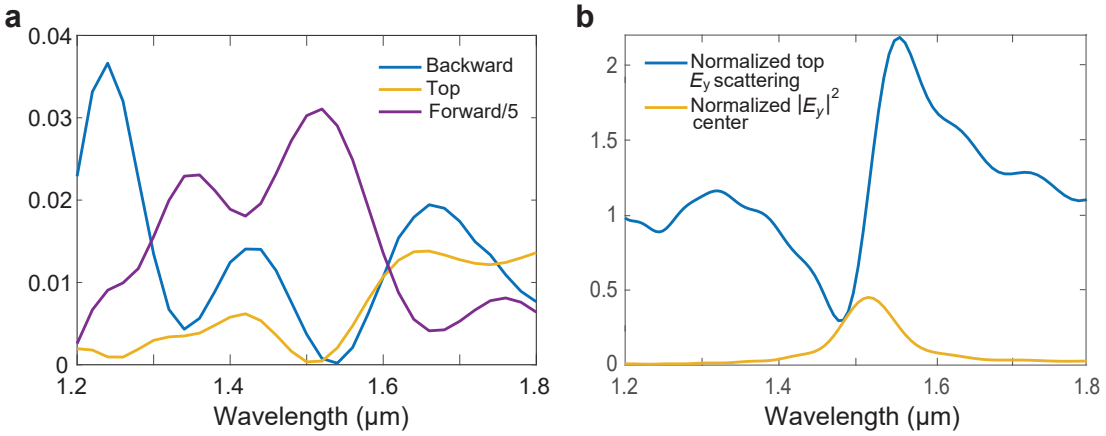

Figure 3.2: **a** Scattering (E_y component) of the disk illuminated in FS by a plane wave with the electric field parallel to the disk axis in the forward, backward and out-of-plane (top) directions. The top scattering shows a minimum around the wavelength for which the second electric anapole is predicted for normal illumination. **b** Normalized top scattering of the disk (blue curve) when illuminated by the light exiting from a waveguide propagating the TE mode. The yellow curve shows the $|E_y|^2$ component at the disk center normalized with respect to the field in the center of an isolated waveguide. The disk dimensions are $t = 350\,\text{nm}$ and $r = 550\,\text{nm}$.

Figures 3.3**a** and **b** show the electric near-field at $\lambda = 1510$ nm (the wavelength showing the top scattering minimum in Fig. 3.2**a**) on the symmetry plane of the disk under left-side lateral illumination either from FS or from a waveguide. We observe field patterns similar to those occurring under normal illumination [63] in the sense of having five field maxima separated by four nodes (forming four vortices of the electric field, as shown by the arrows depicted in Fig. 3.3**b**). The asymmetry in the near-field is due to the symmetry-breaking illumination conditions [104]. But the obtained patterns confirm our hypothesis that we can excite the second-order electric anapole using lateral illumination coming a waveguide.

We also performed numerical simulations with CST when the disk is illuminated by the light exiting from a waveguide propagating the TE mode. Figure 3.4 shows **a** the normalized top E_y scattering and **b** $|E_y|^2$ component at the disk center (normalized with respect to the field at the center of the waveguide) as a function of the disk radius. The results are consistent with those obtained in Figs. 3.1 and 3.2 and show us that increasing the disk radius red shifts both wavelengths, which confirms that the anapole condition can be carefully tuned over the whole telecom wavelengths window.

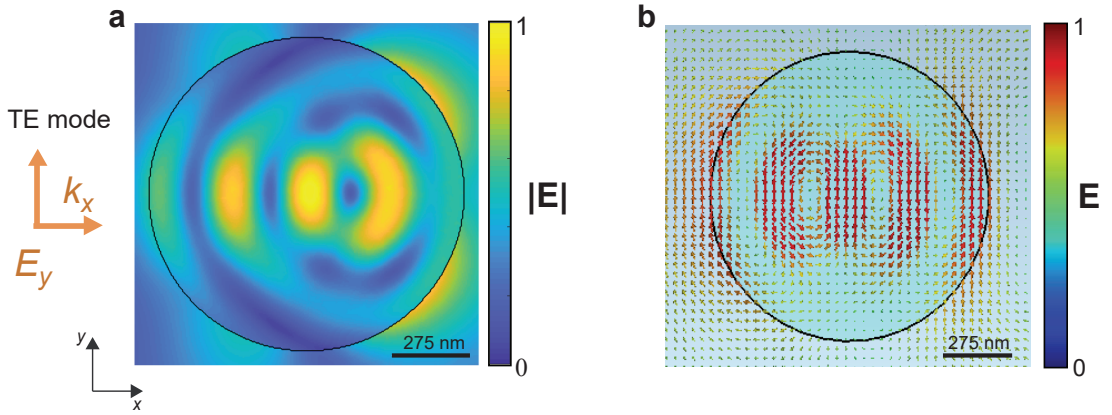

Figure 3.3: (**a**) Near-field pattern of the norm of the electric field at the anapole state wavelength, normalized to its maximum value, at ($\lambda = 1510$ nm); (**b**) Electric field lines at $\lambda = 1510$ nm under waveguide illumination. The disk dimensions are $t = 350$ nm and $r = 550$ nm.

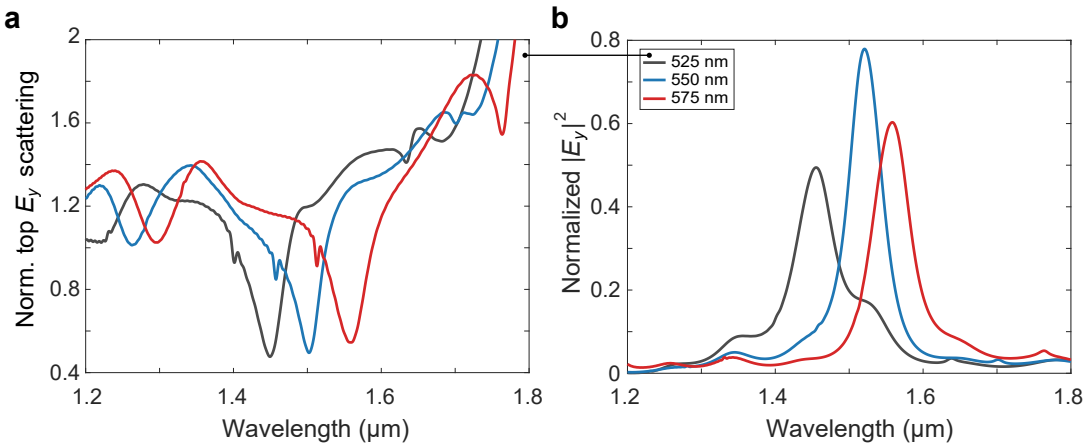

Figure 3.4: **a** Normalized top E_y scattering of the disk and **b** normalized $|E_y|^2$ component at the disk center for disks radius r varying between 525 nm and 575 nm.

Figure 3.5 shows the components of the electric field at the center of the disk when illuminate from a waveguide for disks of radii 525 nm, 550 nm and 575 nm at the anapole state wavelengths 1460 nm, 1500 nm and 1560 nm, respectively. In $|E_y|$ component (transversal electric field), we can see the formation of five main lobes, which confirms the ability of our approach to excite the anapole state.

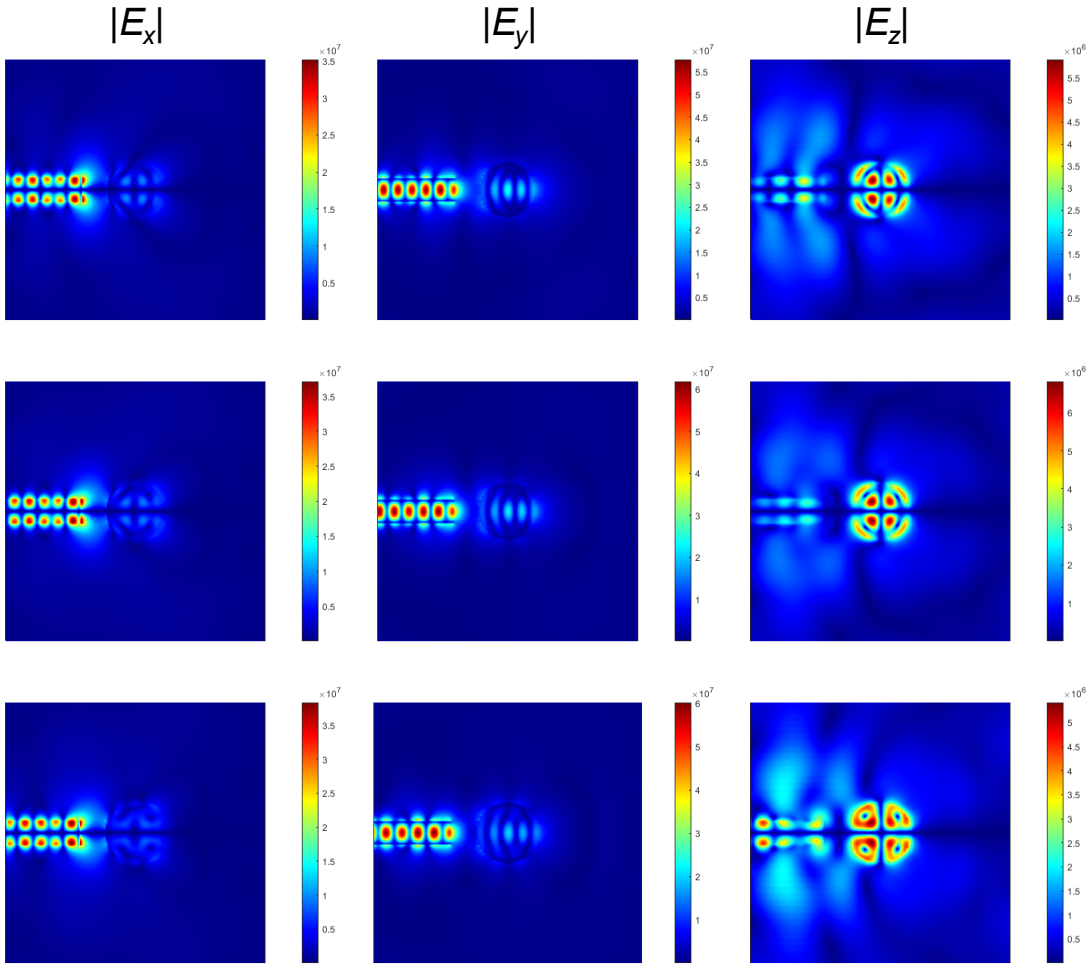

Figure 3.5: $|E_x|$, $|E_y|$ and $|E_z|$ at the center of the disk for disks of radii 525 nm (top row), 550 nm (middle row) and 575 nm (bottom row) at the anapole state wavelengths 1460 nm, 1500 nm and 1560 nm, respectively.

3.3.2 Magnetic anapole

Similar results can be obtained for the magnetic anapole, though now we consider $r = 400$ nm and, in the illumination, the incident field has the main component of the magnetic field pointing along the y-axis, which can be achieved by using the TM of the driving waveguide. It can be seen that the magnetic anapole condition - this is, $M + T_M = 0$ - is satisfied at a wavelength of 1480 nm for both normal (Fig. 3.6**a**) and lateral (Fig. 3.6**b**) illumination. Indeed, in comparison to the case of the electric anapole, we can see a quite broad region with reduced scattering under lateral illumination.

We performed FDTD simulations and calculated the scattered E_x field for both FS (Fig. 3.7**a**) and waveguide (Fig. 3.7**b**) illumination. In both situations, there is a dip in the top scattering response in the wavelength region where the magnetic anapole takes place. This confirms that a reduction of the out-of-plane scattering for the x-polarized far-field can be considered a signature of the existence of a magnetic anapole.

Figures 3.8**a** and **b** depict the magnetic field on the disk plane at the magnetic anapole

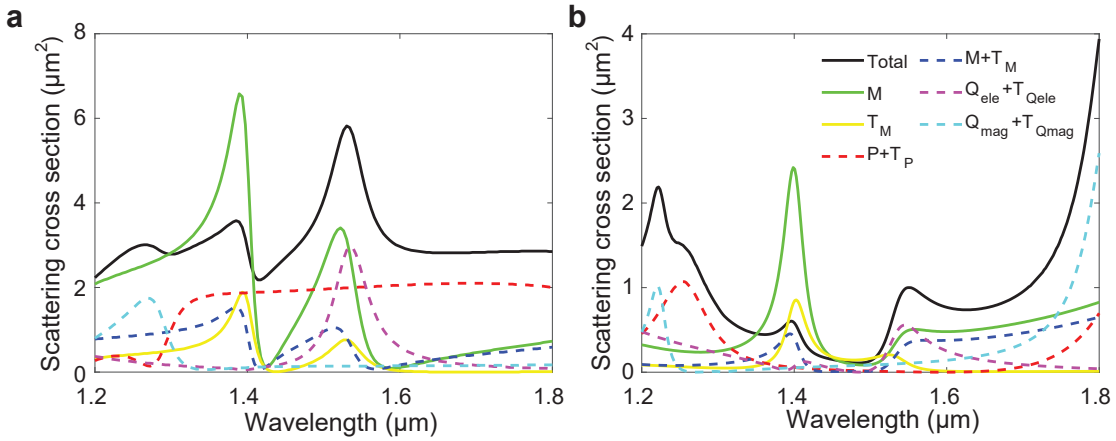

Figure 3.6: Spectral contribution under (**a**) normal and (**b**) lateral illumination of the dipolar electric (**p**) in red and magnetic (**m**) in blue, and quadrupolar electric (Q_{ele}) in purple and magnetic (Q_{mag}) in cyan moments, together with their respective toroidal moments, represented by T, to the scattering cross-section. Also, the individual contributions of the magnetic dipole (green), and its respective toroidal moment (yellow) to the scattering are represented. The disk dimensions are $t = 350\,\text{nm}$ and $r = 450\,\text{nm}$.

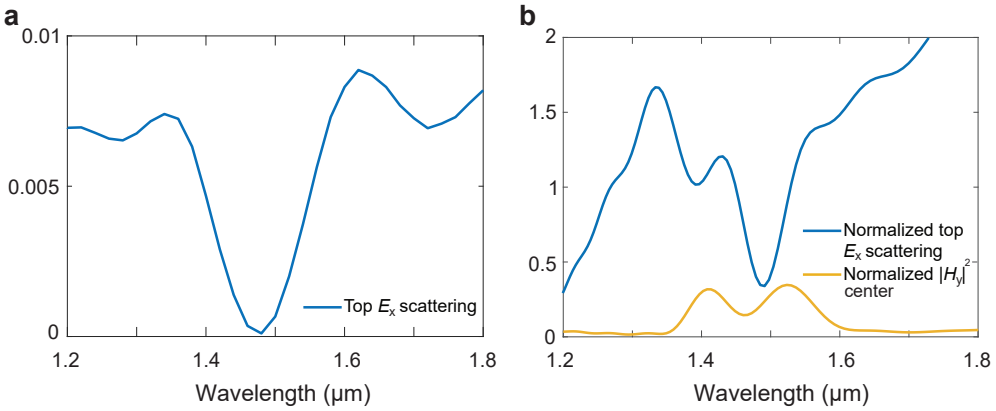

Figure 3.7: **a** Top scattering (E_x component) of the disk illuminated in FS by a plane wave with the electric field parallel to the disk axis. **b** Normalized top scattering of the disk (blue curve) when illuminated by the light exiting from a waveguide propagating the TM mode. The yellow curve shows the $|H_y|^2$ field component at the disk center normalized concerning the waveguide. The disk dimensions are $t = 350\,\text{nm}$ and $r = 450\,\text{nm}$.

wavelength ($\lambda = 1480$ nm) under FS and waveguide lateral illumination, respectively. The in-plane magnetic field in the disk shows three maxima, two nodes and two vortices of the in-plane magnetic field, as expected for a magnetic anapole [54]. Notice the resemblance between the in-plane magnetic field for the first magnetic anapole and the in-plane magnetic field for the first electric anapole addressed in Chapter 2.

We also performed numerical simulations with CST Microwave Studio when the disk is illuminated by the light exiting from a waveguide propagating the TM mode. Figure 3.9 shows **a** the normalized top E_x scattering and **b** $|H_y|^2$ component at the disk

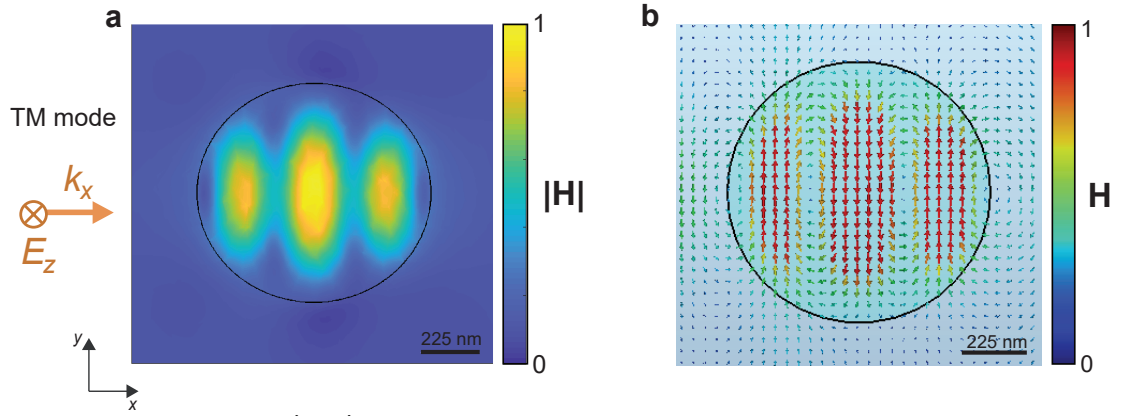

Figure 3.8: **a** Near-field pattern of the norm of the magnetic field at the anapole state wavelength ($\lambda = 1480$ nm), normalized to its maximum value; (**f**) Magnetic field lines at $\lambda = 1480$ nm under waveguide illumination. The disk dimensions are $t = 350$ nm and $r = 450$ nm.

center (normalized with respect to the field at the center of the waveguide) as a function of the disk radius. These results are in good qualitative agreements with the FDTD results shown above.

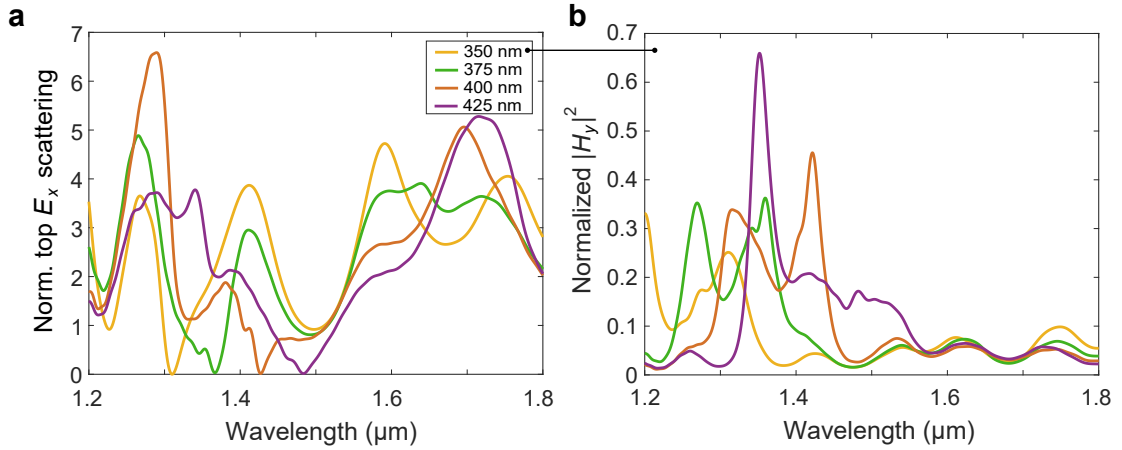

Figure 3.9: **a** Normalized top E_x scattering of the disk and **b** normalized $|H_y|^2$ component at the disk center for disks radius r varying between 350 nm and 425 nm.

The slight variation that the results present in terms of magnetic anapole wavelength with respect to those presented in Fig. 3.7 is due to the use of different simulation methods, since in the FDTD simulations the field is measured at a point, while with CST it is measured on a port that has a certain area. Even so, the results are consistent in that there is a region with reduced out-of-plane scattering, which is considered a signature of the existence of a magnetic anapole. As in the case of the electric anpole, an increase in the disk radius red shifts both wavelengths, which confirms that the anapole condition can be carefully tuned over the whole telecom wavelengths window.

Figure 3.10 shows the components of the magnetic field at the center of the disk when illuminate from a waveguide for disks of radii 350 nm, 375 nm and 400 nm at the anapole state wavelengths 1310 nm, 1370 nm and 1430 nm, respectively. In $|H_y|$ component, we can see the formation of three main lobes, which confirms the ability of our approach to excite the magnetic anapole state using the TM mode of the driving waveguide.

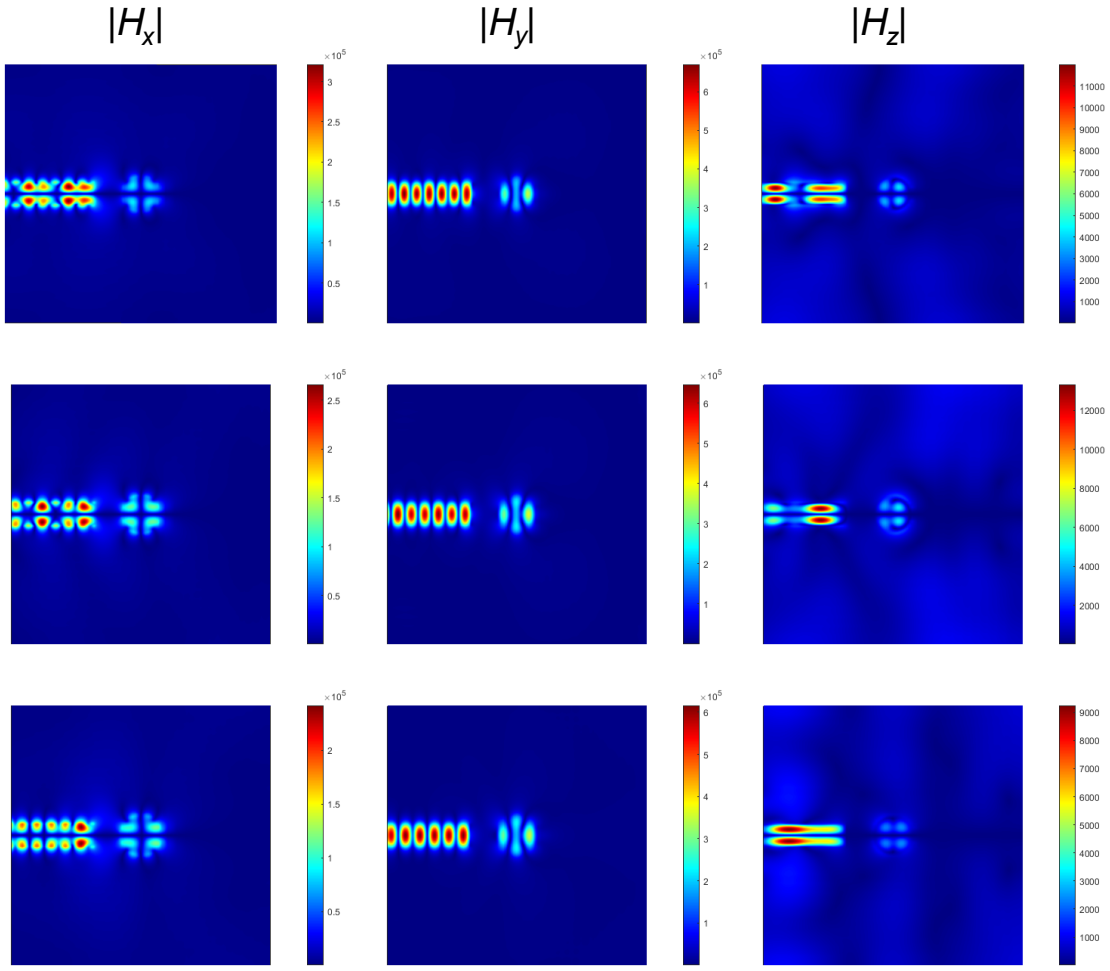

Figure 3.10: $|H_x|$, $|H_y|$ and $|H_z|$ at the center of the disk for disks of radii 350 nm (top row), 375 nm (middle row) and 400 nm (bottom row) at the anapole state wavelengths 1310 nm, 1370 nm and 1430 nm, respectively.

3.4 Far-field scattering measurements of the on-chip silicon disk

To confirm our numerical predictions, we fabricated different samples containing sets of waveguide-disk circuits on a SOI wafer and using standard fabrication tools. Figure 3.11**a** shows a SEM image of one of the fabricated circuits, containing an input waveguide, a Y-junction to split up the incoming guiding signals into two paths and two waveguide

terminations, with only one of them having an adjacent disk (see details in Fig. 3.11**b**). As explained in Chapter 2, this circuit allows us to measure simultaneously the top far-field scattering with and without disk for normalization purposes using the experimental set-up described in Appendix C. The circuit-setup pair also allows us to inject either the TE or the TM mode into the input waveguide. In addition, using a polarizer, we can filter the polarization of the scattered field to select either the E_y or the E_x component that allows to identify the scattering produced by the transverse electric or magnetic dipoles.

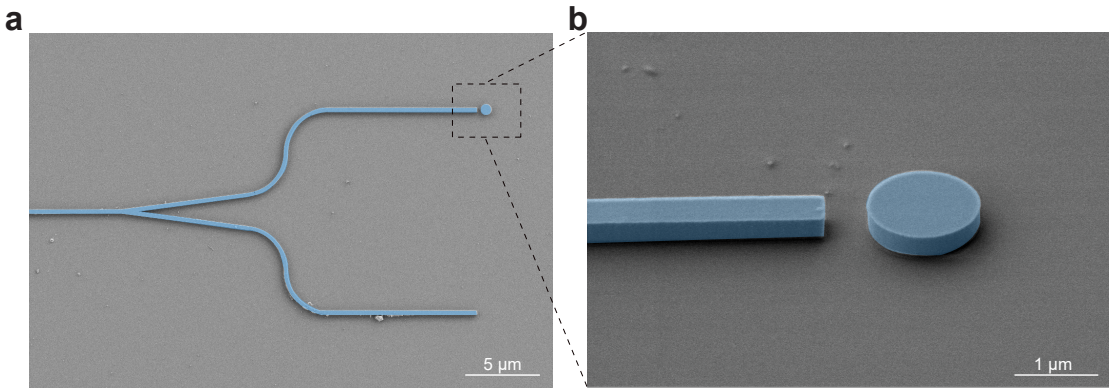

Figure 3.11: **a** SEM image of one of the fabricated circuits, showing the input waveguide, a Y-splitter, and two waveguides, both ended in an abrupt termination, and one of them having a disk. **b** SEM image showing in detail the disk and the waveguide termination. Nominal disk radius $r = 550$ nm, thickness $t = 350$ nm, waveguide width $w = 450$ nm and gap $g = 500$ nm.

First, we characterized the second electric anapole by using the TE mode of the input waveguide. Figure 3.12**a** shows the measured normalized out-of-plane scattering for three different disks having nominal radii of 525, 550 and 575 nm. We observe that there is a wavelength region with reduced scattering (reaching even 0.5 for $r = 550$ nm) which confirm the results of the numerical simulations presented in Figs. 3.2 and 3.4. Notice that the overall response is slightly red-shifted as a result of the presence of the silica substrate. The top scattering is, indeed, smaller than for the case of the terminated waveguide without disk (in other words, normalized scattering < 1 in agreement with numerical simulations), which means that not only the scattering is well suppressed, but also that the excitation of the electric and toroidal dipoles corrects the divergence of the beam exiting the waveguide termination and contribute to reduce the overall scattering out of the chip. This was also observed in the case of the first-order electric anapole [104] and also occurs in the case of the magnetic anapole shown below. As expected, the wavelengths at which the scattering minimum is measured increase in proportion to the disk radius [52]. Although the second electric anapole is supposed to provide a narrower response than the first one [63], we observed similar bandwidth in the scattering response for both the first [104] and second anapoles.

Finally, we characterized the magnetic anapole by using the TM mode of the input waveguide, being the results depicted in Fig. 3.12**b**. Again, we observe well defined minima (reaching normalized scattering values below even 0.5) of the top scattering at wavelengths that depend on the disk radius. Again, the minima are red-shifted in

comparison to the numerical simulations, which we attribute to the silica substrate, as already addressed in Chapter 2.

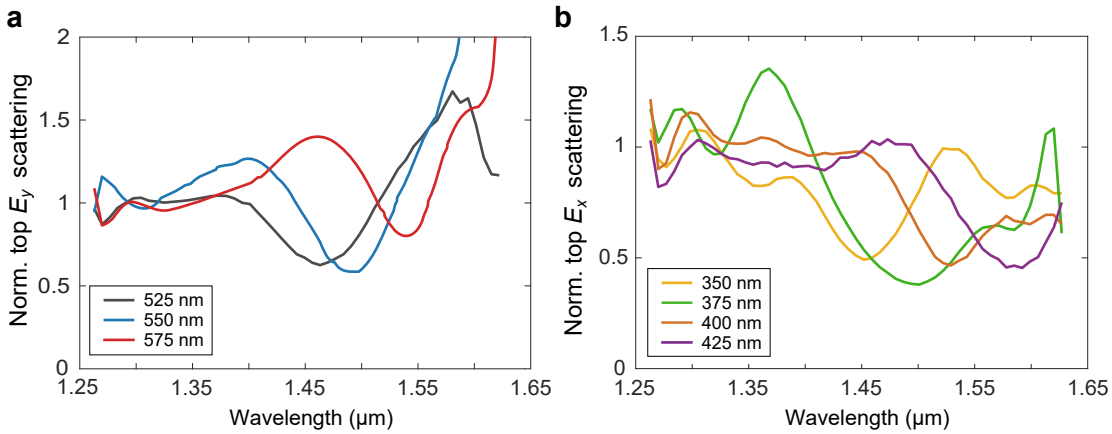

Figure 3.12: Experimental results of the out-of-plane scattering normalized to the value for a bare waveguide termination (no disk), recorded for disks with different radii (shown in the panels) under illumination with the TE/TM waveguide modes, detecting the E_y/E_x components of the far-field.

In this chapter, we have shown that the use of integrated waveguides for on-chip excitation of wavelength-sized silicon disks enables the observation of higher-order anapoles under in-plane illumination. To achieve this goal, first we increase the dimensions of the disk so that the target anapoles could be excited in the wavelength region that is accessible experimentally. This mainly required to work with thicker silicon layers (350 nm instead of the usual 220 nm thickness). Then, we used either the TE or the TM mode of the input waveguide to excite either the second-order electric anapole or the magnetic anapole. Notice that we only consider states with in-plane moments since these are the ones that can radiate in the vertical direction (out-of-plane) and, therefore, its suppression can be detected via far-field scattering measurements.

In contrast to the results of Chapter 2, here near-field experiments were not performed. But the reduction in scattering observed in far-field experiments is consistent with our simulation results. In particular, near-field simulations showed the formation of several vortices in the local electric and magnetic fields, in agreement with the results in the literature.

Noteworthy, we observed that for the case of the second-order electric anapole, multipolar decomposition does not predict a suppression of scattering for lateral incidence (which is otherwise predicted for normal incidence). Still, we show that there is a reduction of the top scattering at the predicted wavelengths, which can be used in PICs to build complex circuitry without out-of-plane scattering.

Chapter 4

Light guidance along silicon slotted-disk chains driven by integrated waveguides

Contents

4.1 Introduction

Previous chapters have focused on the observation of anapoles states in single disks illuminated transversely by a photonic waveguide. The radiationless properties of such states may also play a role when forming periodic chains of disks: in principle, minimizing the out-of-plane scattering should contribute to the efficient guiding of light along such chains even for modes placed above the light line (and therefore inherently lossy). It has been suggested and experimentally observed that chains of slotted disks can efficiently guide light around 10 µm wavelengths using modes over the light line around the anapole state, exploiting its reduced out-of-plane scattering [77]. However, as suggested in Ref. [77], this feature should be most valuable when building the chains on SOI and performing the guidance in the technologically-relevant telecom wavelength regime.

In this chapter, we analyze numerically and experimentally the guidance of light along straight and bent chains of regular and slotted silicon disks in the 1.5 µm wavelength region. In agreement with Ref. [77], we find that the introduction of an air gap in the silicon disks improves the coupling and enhances the transmission efficiency. However, our results suggest that the guidance is not related to the existence of the electric anapole state but to the excitation of a toroidal dipole that couples adjacent disks together with a magnetic quadrupole that contributes to reducing the out-of-plane scattering. Numerical simulations of the periodic chain of slotted disks confirm the existence of a high-Q leaky resonance over the light cone. Experiments are in good agreement with numerical simulations and demonstrate the importance of interference between Mie modes to build on-chip photonic based on wavelength-scale disks.

4.2 Numerical simulations

We start by considering the structure sketched in Fig. 4.1. It consists of a chain of evenly-spaced (period a) silicon disks with thickness t and radius r. The disks may eventually have an air gap of size G splitting them into two identical halves. We consider that rectangular cross-section waveguides (width w) are used as input and output ports: the left-hand side waveguide is used to illuminate the disk chain using the TE guided mode, whilst the right-hand side waveguide is used to collect the transmitted light.

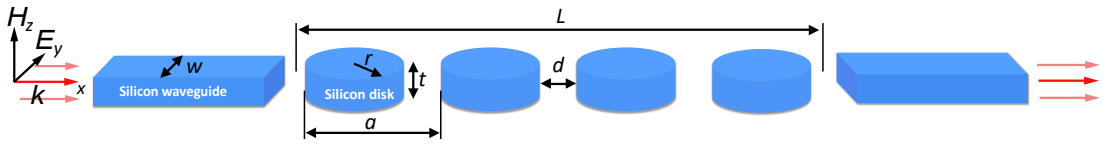

Figure 4.1: Sketch of the structure under study: an array of silicon disks (in the plot, there are $N = 4$ disks) with radius r and thickness t with period a is placed between two silicon waveguides (width w) that act as input and output ports.

In Chapter 2 we verified that a single disk with $r = 350$ nm and $t = 220$ nm supports an electric anapole at wavelengths around 1.5 µm under lateral illumination. Therefore, we have chosen this radius to perform numerical simulations of the transmission exhibited by a disk chain. The obtained results for 6, 10, and 14 disks and $a = 920$ nm - this means that the spacing between neighbor disks is 220 nm - are depicted in Fig. 4.2**a**. The transmission curves are normalized with respect to the response of a single straight waveguide. Interestingly, no appreciable transmission is observed in the region where the anapole takes place. Instead, we observe high transmission at wavelengths over 2 µm, which is attributed to truly-guided modes (or bound states [105]) below the light line (such modes can potentially appear at wavelengths $> 2a$ [82]) as well as in a region around 1.35 µm, which we can be ascribed to higher-order Mie resonances [104, 106].

We also performed calculations for different values of the period a in a chain formed for six disks to check its influence over the transmission behavior. The results, depicted in Fig. 4.2**b**, show that the transmission grows in the 1.5 µm wavelength region when the period a is reduced to values of 850 nm and below. Noticeably, the non-negligible transmission peaks for a values of 750 and 800 nm can be ascribed to the fact that those peaks occur in wavelength regions placed below the light line. Still, even for a separation between disks as small as 50 nm, the transmission in the anapole region is negligible. This means that the existence of the first electric anapole state does not provide a means for efficient energy transmission along disks chains. Therefore, the absence of out-of-plane scattering is not sufficient to ensure light guidance through the chain.

This observation is consistent with the results reported in Ref. [77], where it is shown that transmission along a chain of perfect disks is largely attenuated around the electric anapole wavelength, even when the disks are very close to each other. However, Ref. [77] proposed that the insertion of an air gap in the disk could contribute to reduced losses and achieve highly efficient transmission. Following this idea, we performed simulations of chains of slotted disks having air gaps of $G = 0.5r$ and $G = 0.9r$, choosing the disk radius ($r = 410$ nm and $r = 530$ nm, respectively) and the inter-disk spacing

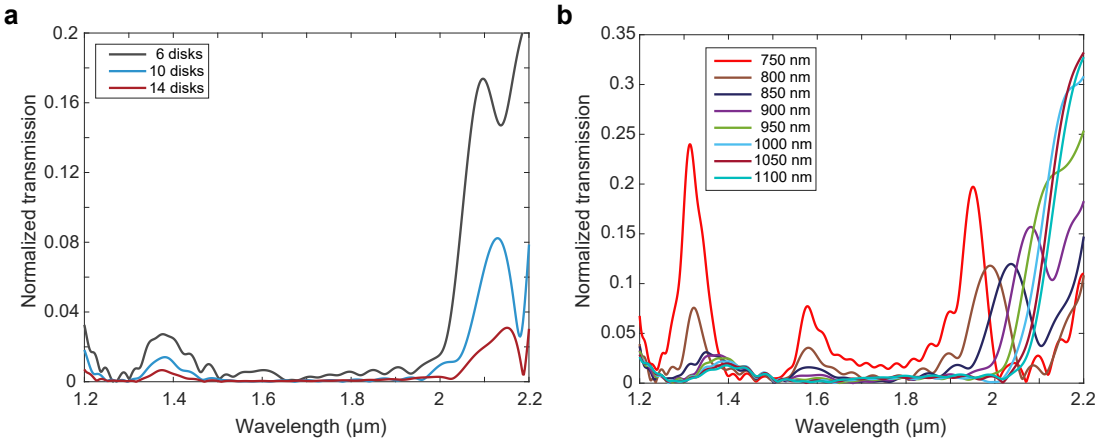

Figure 4.2: Transmission spectra normalized with respect to the response of a single waveguide ($w = 800$ nm) of **a** chains of 6, 10, and 14 disks with $r = 350$ nm, $t = 220$ nm and $a = 920$ nm and **b** chains of 6 disks with $r = 350$ nm and different values of the period a.

($d = 220$ nm) to allocate a transmission band close to the 1.5 μm wavelength region. The results, depicted in Fig. 4.3**a**, show that the insertion of the air-gap gives rise to a frequency region with relatively large transmission, specially in the case of $G = 0.5r$. We also computed the transmission at maxima along straight chains of different amounts of disks in the three cases shown in Fig. 4.3**a**. The results, depicted in Fig. 4.3**b**, show that the $G = 0.5r$ configuration performs better in terms of insertion (≈ 3.4 dB) as well as propagation (≈ 0.75 dB/μm) losses, in agreement with the results in Ref. [77].

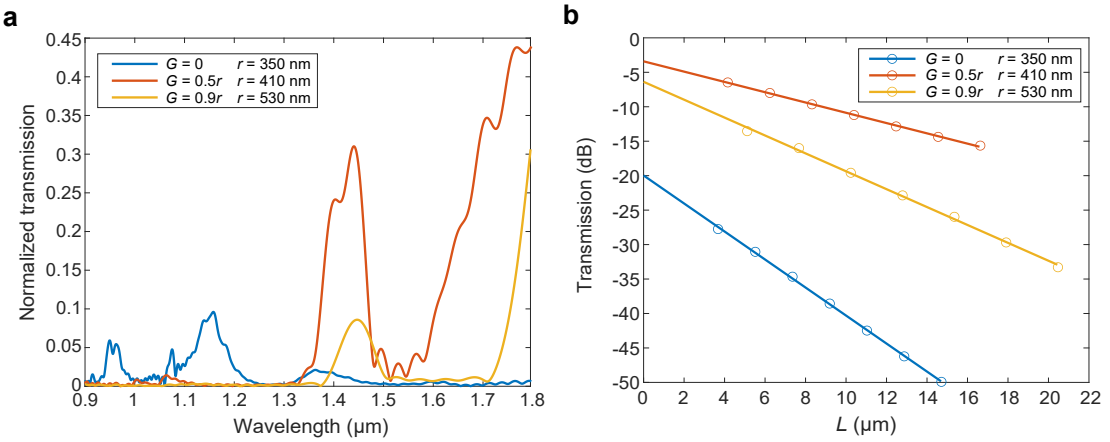

Figure 4.3: **a** Transmission across six disks for different values of the radius r and the air gap G (see legend), when a spacing between disks $d = 220$ nm is considered. **b** Normalized transmission as a function of the number of disks for different values of G (see legend) at the wavelength of maximum transmission. The slope gives the propagation loss, and the values for $L = 0$ gives the insertion loss.

In order to establish a link between the transmission bands and the existence of

anapole states in a single disk, we calculated the multipole decomposition under lateral illumination (Fig. 4.4) for the three different cases considered in Fig. 4.3**a**.

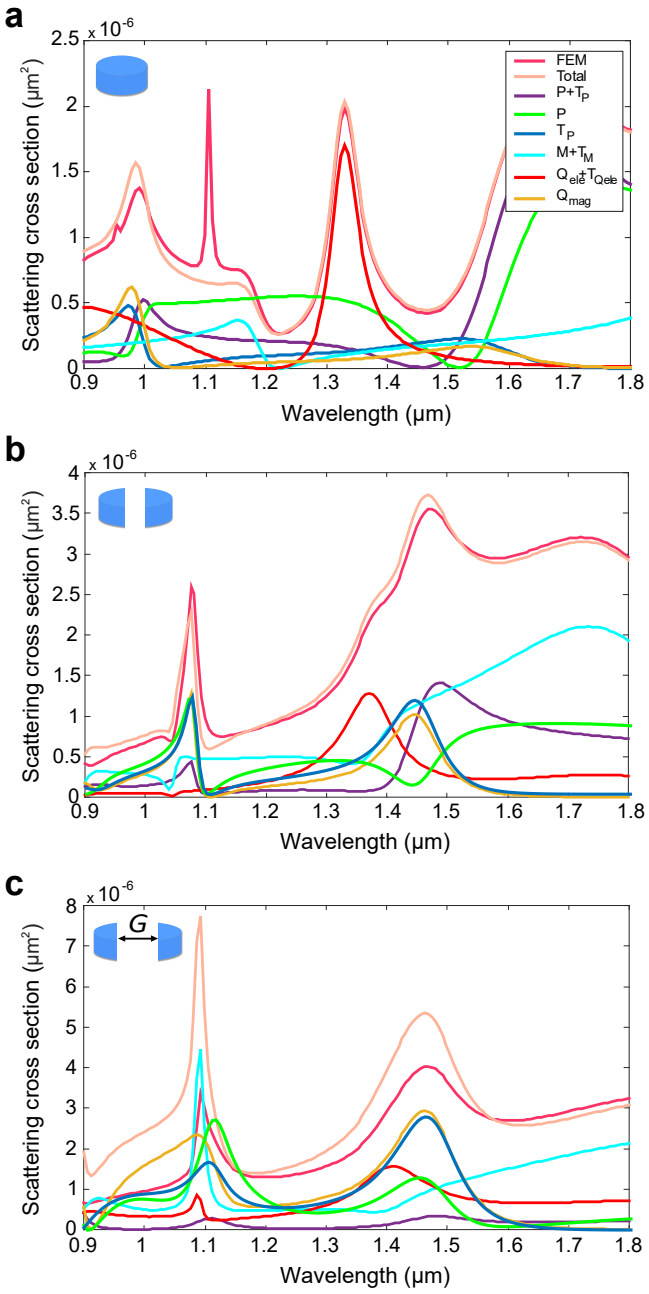

Figure 4.4: **Multipole response of isolated silicon disks**. Scattering spectra of a silicon disk with **a** $r = 350$ nm and $G = 0$, **b** $r = 410$ nm and $G = 0.5r$ and **c** $r = 530$ nm and $G = 0.9r$. Spectral contribution under lateral illumination of the dipolar electric (**P**), dipolar magnetic (**M**), quadrupolar electric (Q_{ele}) moments, and their respective toroidal moments, represented by **T**, to the scattering cross-section. Also, the individual contributions of the quadrupolar magnetic (Q_{mag}) and the electric dipole (**P**), together with its respective toroidal moment (T_P) to the scattering, are shown.

Figure 4.4 shows the contributions to the scattering cross-section of the main mul-

tipole moments for **a** $r = 350$ nm and $G = 0$ (the case considered in Chapter 2), **b** $r = 410$ nm and $G = 0.5r$ and **c** $r = 530$ nm and $G = 0.9r$. It can be seen that the wavelength regions of maximum transmission in Fig. 4.3**a** also corresponds to region of large scattering (Figs. 4.4**b** and **c**), but not to the electric anapole condition that takes place at much smaller wavelengths. In particular, it seems that the maximum transmission along the disk chain is linked to the existence of two higher-order multipoles in an isolated disk.

To confirm this assumption, we obtained the wavelength of occurrence of the different relevant states (the electric anapole, the toroidal dipole, and the magnetic quadrupole) for a single disk together with the maximum transmission wavelength along a disk chain as a function of G. As shown in Fig. 4.5, the transmission maximum perfectly overlaps with the toroidal dipole and the magnetic quadrupole whilst the electric anapole is always shifted to shorter wavelengths. Noteworthy, also in Ref. [77] there are a toroidal dipole and a magnetic quadrupole mode at the frequencies of maximum transmission.

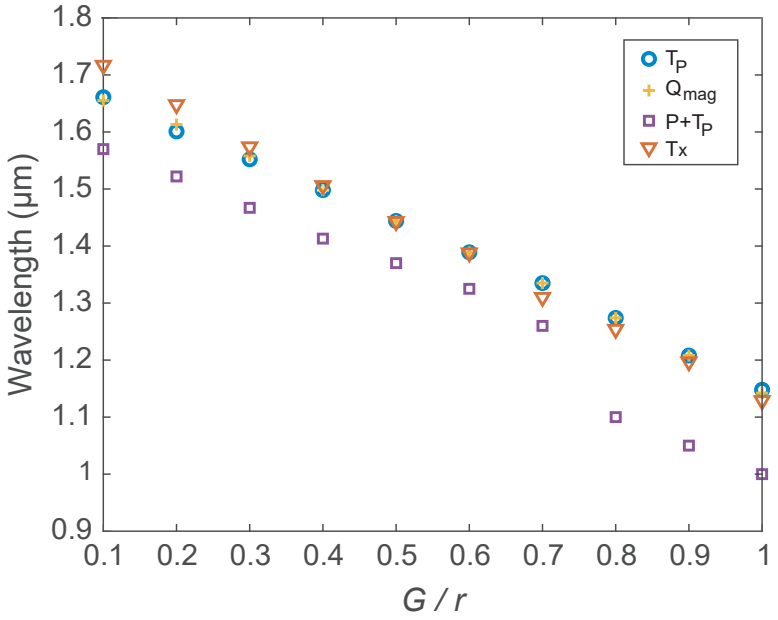

Figure 4.5: Calculated wavelengths of maximum chain transmission (Tx), electric anapole ($P + T_P = 0$), toroidal dipole (T_P) and magnetic quadrupole (Q_{mag}) as a function of the disk slot size G. The disk radius is $r = 410$ nm.

To verify the previous assumption, we performed simulations of continuous-wave signals propagating through the chains at the wavelength of maximum transmission for the case $r = 410$ nm, and $G = 0.5r$. The results, depicted in Fig. 4.6, show the existence of a closed-loop for the magnetic field on the x-z plane around the slotted disk. This is consistent with the excitation of the toroidal dipole [45], in agreement with the multipolar decomposition. In addition, the simultaneous excitation of the magnetic quadrupole results in a reduction of the magnetic field strength in the regions over and below the disk (see the arrows in Fig. 4.6**c**). This should contribute to reducing the scattering along the disk axis (out-of-plane scattering), as previously shown [107, 108] and depicted in the sketch presented in Fig. 4.7.

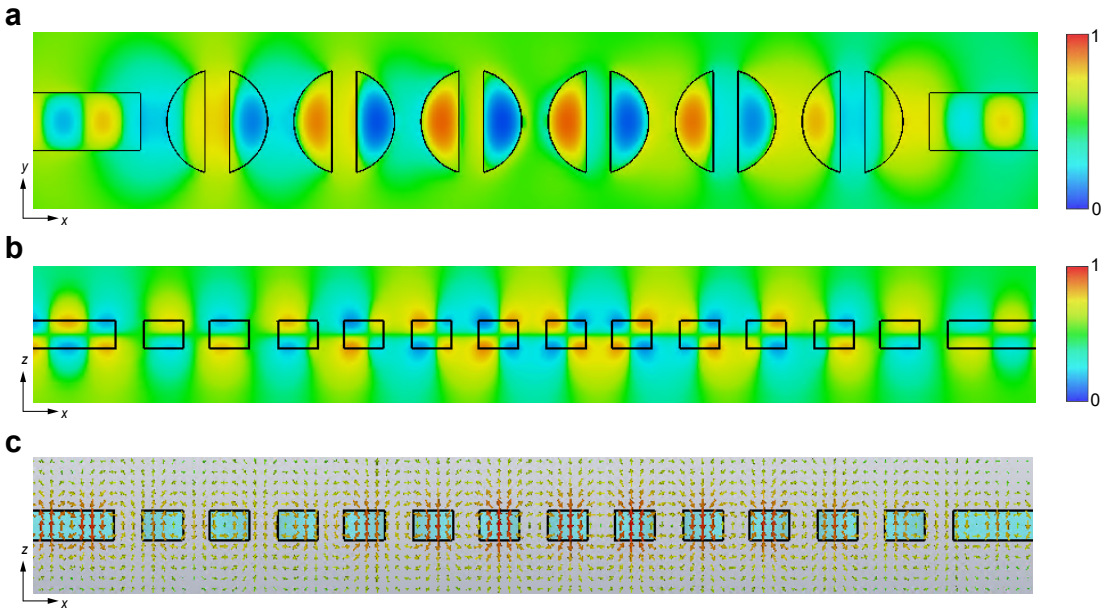

Figure 4.6: **Magnetic near-fields along the slotted disk chain at maximum transmission** ($\lambda = 1443$ nm). **a** Snapshot of H_z on the x-y plane. **b** Snapshot of H_x on the x-z plane. **c** Magnetic field H lines represented by arrows on the x-z plane. The disk dimensions are $r = 410$ nm, and $G = 0.5r$.

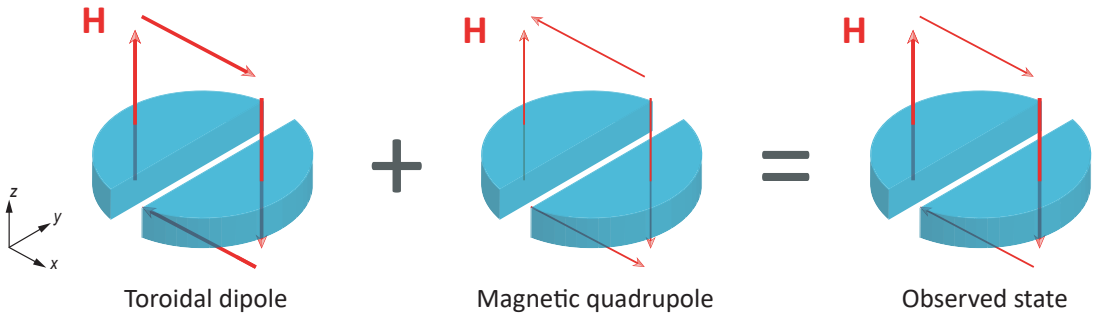

Figure 4.7: Sketch of the superposition of the magnetic field loops for the toroidal dipole and the magnetic quadrupole, resulting in the observed states.

We also performed simulations of continuous-wave signals propagating through the chains at the wavelength of maximum transmission for the cases $r = 530$ nm, $G = 0.9r$ (Fig. 4.8) and $r = 350$ nm, $G = 0$ (Fig. 4.9). The results shown in Fig. 4.8 are consistent with those depicted in Fig. 4.6 where we can see the existence of a closed-loop for the magnetic field on the x-z plane around the slotted disk. However, no appreciable transmission is observed in Fig. 4.9 at the wavelength where the anapole takes place.

In Ref. [108], it was shown that the excitation of toroidal dipoles in coupled high-index disks could eventually lead to the existence of bound states in the continuum (BICs) when forming 2D lattices. Therefore, in accordance to the results above, it

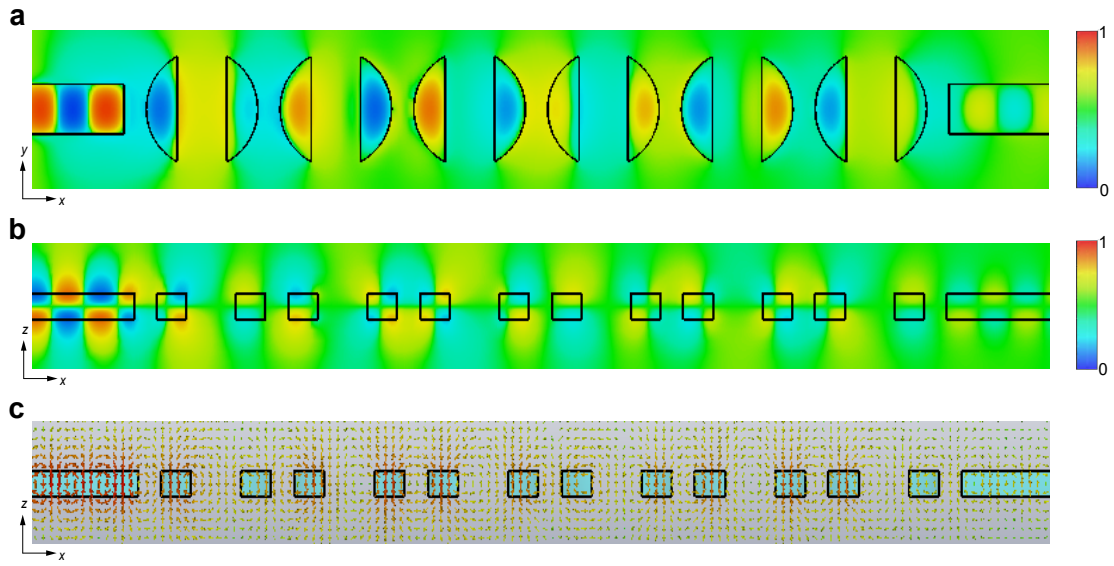

Figure 4.8: **Magnetic near-fields along the slotted disk chain at maximum transmission** ($\lambda = 1450$ nm). **a** Snapshot of H_z on the x-y plane. **b** Snapshot of H_x on the x-z plane. **c** Magnetic field H lines represented by arrows on the x-z plane. The disk dimensions are $r = 530$ nm, and $G = 0.9r$.

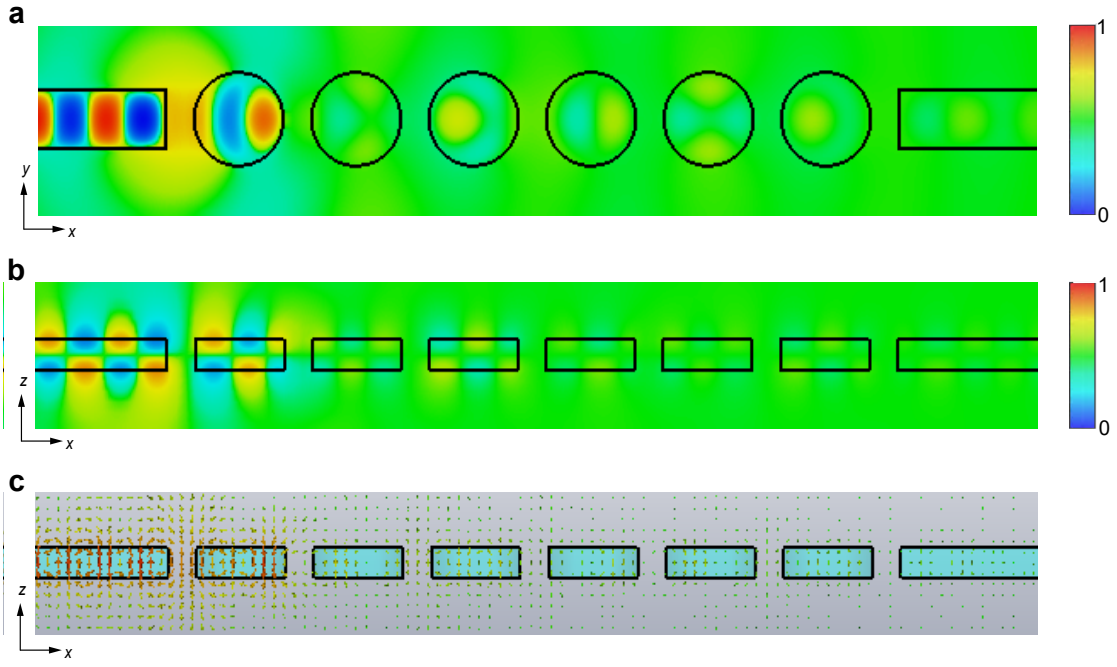

Figure 4.9: **Magnetic near-fields along the disk chain at maximum transmission** ($\lambda = 1159$ nm). **a** Snapshot of H_z on the x-y plane. **b** Snapshot of H_x on the x-z plane. **c** Magnetic field H lines represented by arrows on the x-z plane. The disk dimensions are $r = 350$ nm, and $G = 0$.

makes sense to consider if the slotted-disk chains can also support toroidal BICs and this could be the reason explaining the large transmission over the light line. To analyze the existence of BICs, we calculated the optical Q factor of a periodic chain of slotted disks. Figure 4.10 reports the results of numerical simulations of an infinite chain of disks with $G = 0.5r$. To ease the visualization of the relevant modes, the size of scatter points has been chosen as directly proportional to the mode energy confinement factor within the silicon region. The band structure along the chain direction shows few regions with flat dispersion (Fig. 4.10**a**), which corresponds to local maxima in the density of states (Fig. 4.10**b**). These regions could correspond to peaks in the transmission, especially when combined with high Q-factors, which are reported in Fig. 4.10**c**. The green flat region around $\lambda = 1.43$ µm, highlighted with a black arrow in panel Fig. 4.10**a**, it is likely the main responsible for the strong transmission peak shown in Fig. 4.3**a**, whose range between 1.32 and 1.46 µm is compatible with our simulations. Interestingly, a strong increase in Q-factor can be observed for the red-colored band around $\lambda = 1.54$ µm. This could hint towards the existence of a symmetry-protected BIC which could be difficult to detect in transmission experiment due to its existence for non-propagating waves at $[k_x,k_y] = [0,0]$.

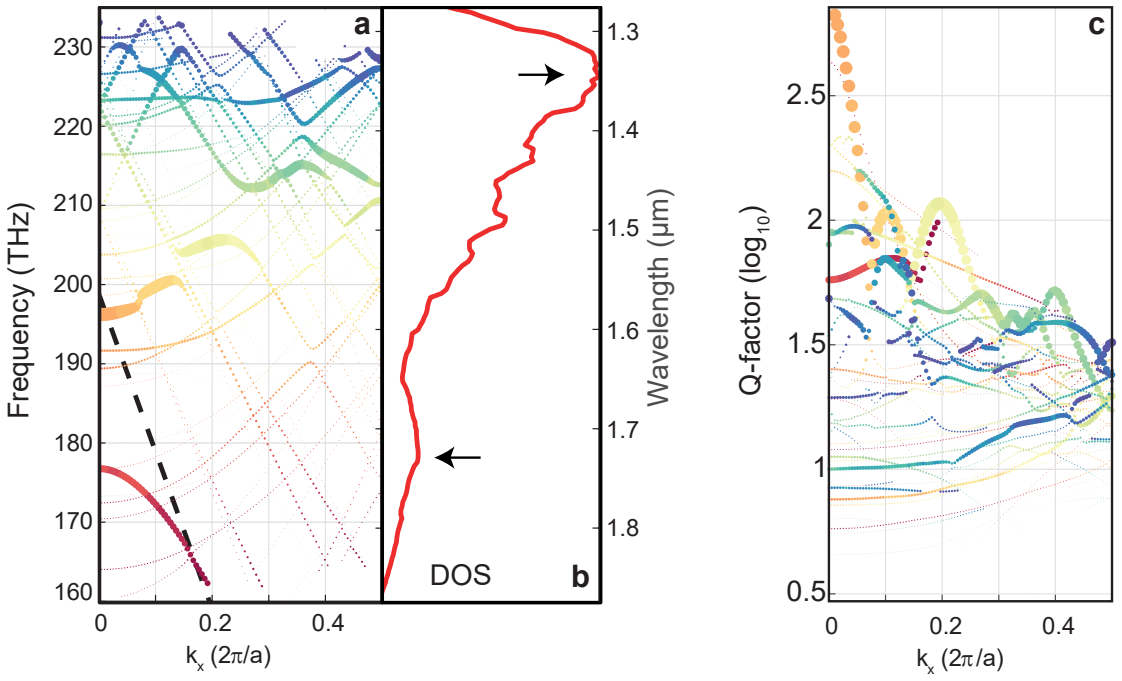

Figure 4.10: **Band structure of infinite chain of slotted disks. a** Band structure, **b** Density of States (DOS) and **c** Q-factors for an infinite chain of slotted disks with $G = 0.5r$. Marker size is proportional to the confinement factor of the electric field within the disk. Different modes are color coded to aid the comparison between panel **a** and **c**. Credit: Dr. Alessandro Pitanti, Istituto di Nanoscienze and Scuola Normale Superiore (Italy).

4.3 Experimental measurements

To confirm our numerical predictions, we used standard fabrication tools (see Appendix B) to fabricate different samples containing sets of straight and curved disks chains with waveguides as input and output ports, following the configuration sketched in Fig. 4.1. Figure 4.11 shows SEM images of several fabricated circuits with different G values and including both straight and curved (curvature radius R) chains, highlighting in detail the waveguide ends acting as input and output ports as well as the disk chains. The waveguides were adiabatically widened up to 3 µm to reduce coupling losses from the input lensed fiber as well as to the output detection system [27] (see Appendix B).

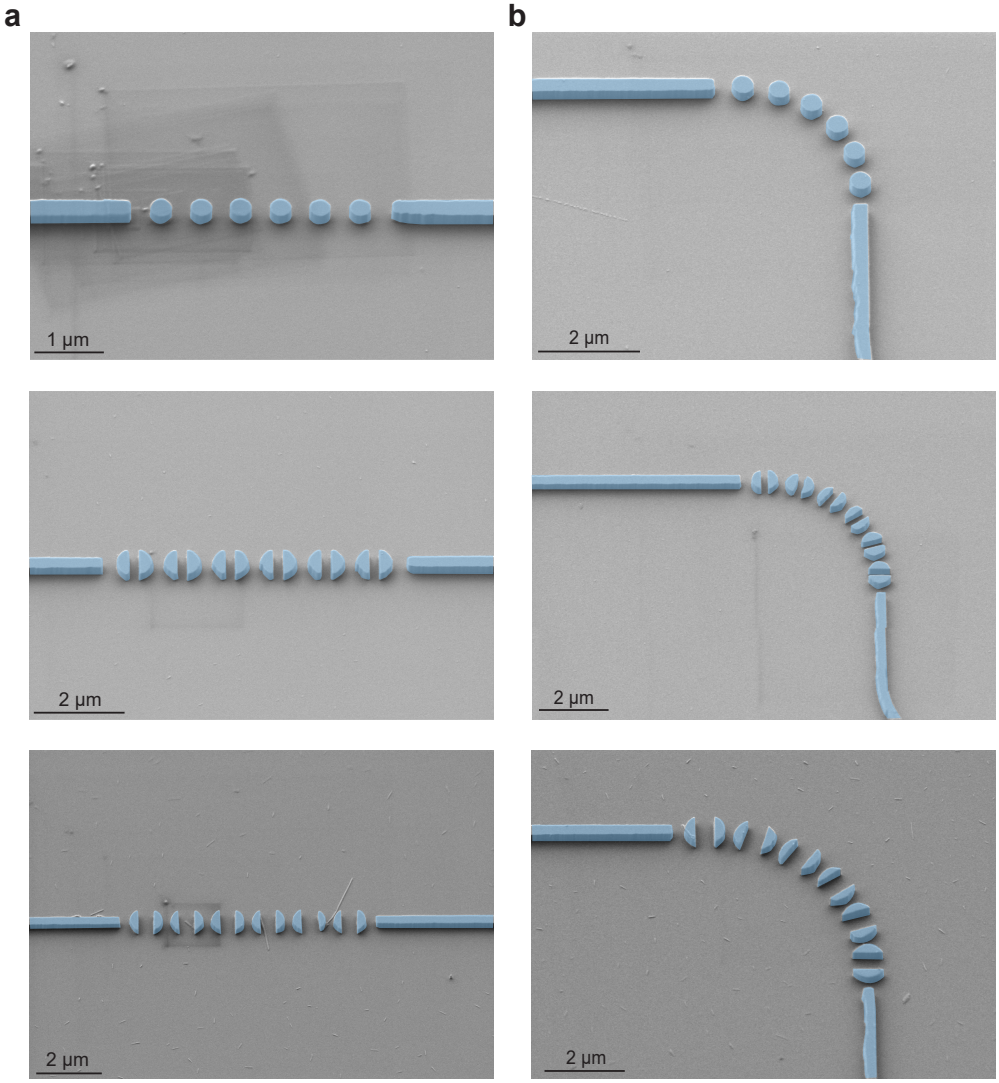

Figure 4.11: **False-color SEM micrographs of several fabricated samples.** Fabricated samples for six disks forming **a** straight and **b** bent chains. Rectangular cross-section waveguides are employed as input and output ports. Circuits with $G = 0$ (top panels), $G = 0.5r$ (middle panels), and $G = 0.9r$ (bottom panels) were fabricated using standard silicon nanofabrication processes. The curvature radii R are 2060 nm for $G = 0$, 3390 nm for $G = 0.5r$ and 4020 nm for $G = 0.9r$.

We also performed numerical simulations including the silica substrate (Figs. 4.12**a,b** and 4.13**a-d**) to compare the results of the experimental measurements. Figure 4.12**b** shows the measured normalized transmission for two straight chains with nominal disk radii of 400 and 425 nm with air gap $G = 0.5r$ (Fig. 4.11**a**, middle panel), separated by a 220 nm gap. Coupling losses were about 15 dB per facet and additional losses are due to some imperfections induced by problems in the etching of the disks (see SEM images

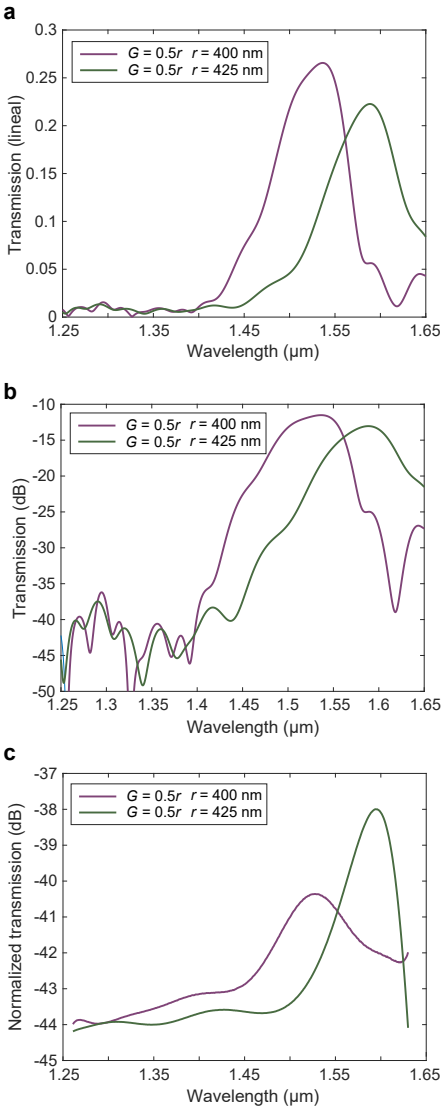

Figure 4.12: **Experimental light transmission along straight chains of disks. a,b** Numerical and **c** experimental transmission along a straight chain of six disks with different radii r (nominal values shown in the panels) and air gap $G = 0.5r$. To reproduce the experimental conditions, we have considered that the silicon disk lie on a silica substrate in the simulations. Normalization in the experimental panels is performed in comparison to the input power (1 mW).

in Fig. 4.11). Even though the noise level in our measurement system was about -44 dBm, we clearly observe a maximum transmission region in good agreement with the results obtained in the simulations depicted in Fig. 4.12**a,b** for the two radii under consideration. Notice that the transmission region is red-shifted in comparison to the results of Fig. 4.4, which we ascribed to the disk chain resting on a silica substrate.

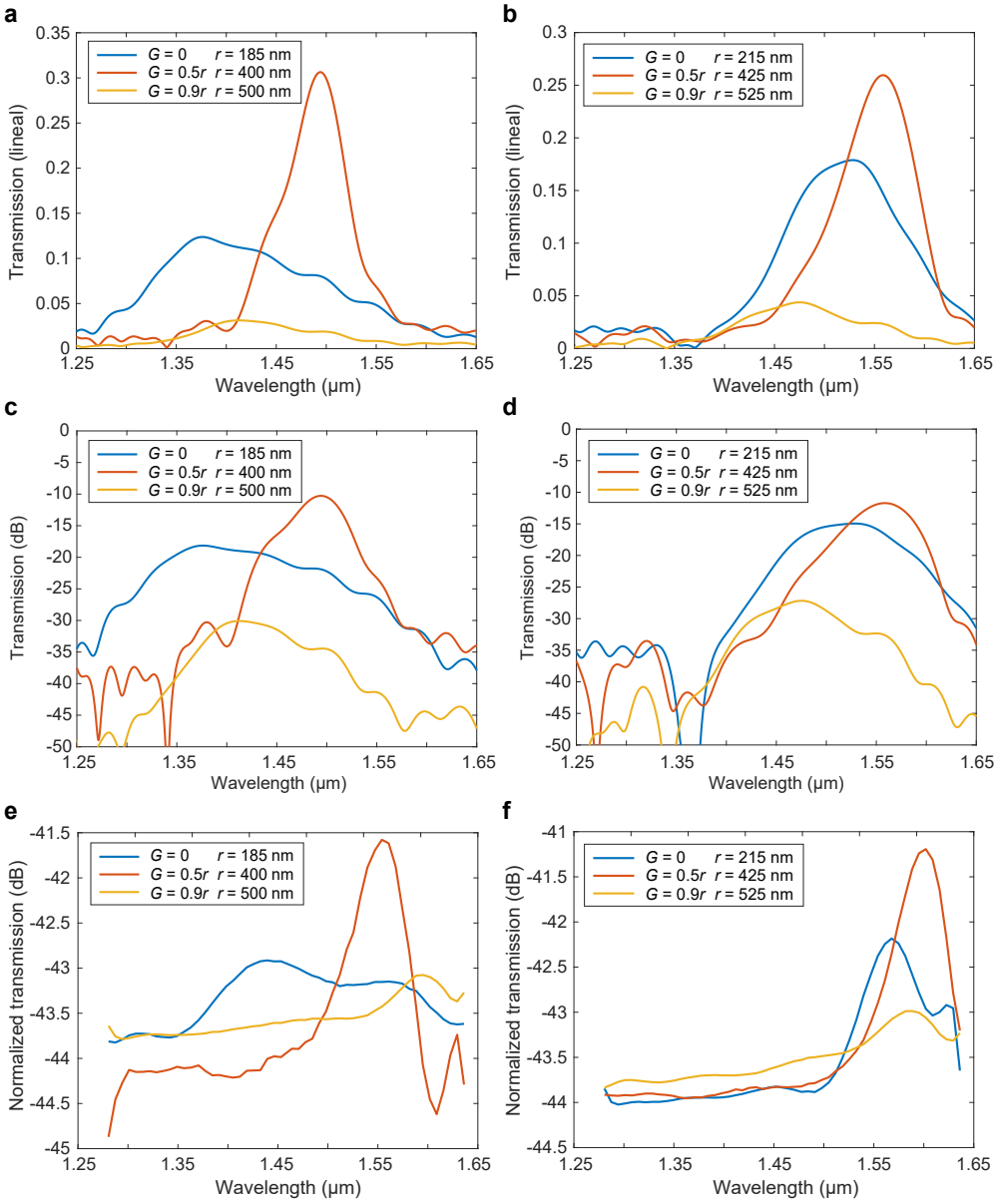

Figure 4.13: **Experimental light transmission along bent chains of disks. a-d** Numerical and **e,f** experimental transmission along curved chains of six disks with different radii r and air gaps G (shown in the panels). To reproduce the experimental conditions, we have considered that the silicon disk lies on a silica substrate in the simulations. Normalization in the experimental panels is performed in comparison to the input power (1 mW).

We also performed experimental measurements on the bent chains with different air gaps in the disks as the ones shown in Fig. 4.11. The air gap of each disk was properly rotated to follow the curvature of the chain and keep perpendicular to the curve. No further engineering on the position of the disks was performed to improve the optical transmission. We included chains with disks having $r \approx 200$ nm and $G = 0$ for comparison purposes. Figures 4.13**e** and **f** show the measured normalized transmission for bent chains with three different air gaps: $G = 0$, $G = 0.5r$, and $G = 0.9r$, each for two different nominal radii disks (shown in the panels). Again, we observe a wavelength region with the maximum transmission, which confirms the results of the numerical simulations presented in Figs. 4.13**a-d** as well as the experimental results on sharp bends reported in [77]. Indeed, our results also confirm that the disk chains with $G = 0.5r$ show the best performance. Notably, these results show that the toroidal-aided guidance along chains of subwavelength dielectric scatterers is also an interesting mechanism enabling low-loss guidance over sharp bends.

In this chapter, we have analyzed the guidance of light along periodic chains of silicon disks in the technologically-relevant telecom wavelength regime, thus extending the results of previous chapters to systems containing multiple disks. We have found that chains of perfect disks do not transport energy at wavelengths corresponding to the electric anapole state, but when the disk is split into two halves by an air gap of width G, energy transportation along chains can be relatively large, even building bent chains.

Chapter 5

Observation of photonic bandgap closure in 1D periodic chains of high-index nanobricks driven by integrated waveguides

Contents

5.1 Introduction

In the previous chapter, we have shown how certain multipolar moments (the electric toroidal dipole and the magnetic quadrupole) can contribute to efficient light guiding along periodic chains of slotted silicon disks at frequencies placed over the light line where propagation is essentially lossy since any mode can couple to the radiation continuum. In this case, the propagation features are not mainly determined by the periodicity but by the multipolar response of the isolated scatterers forming the chain. It makes sense therefore to see if the multipolar response of the scatterer can also play a role for guided modes placed below the light line, so they propagate inherently without losses.

As discussed in Chapter 1, the first PBG is remarkably important in integrated guided optics since it is usually the only one placed below the light cone; therefore, it can give rise to localized modes with large Q factors when defect-like cavities are created. TIR in the 2D perpendicular to the propagation direction, where the system is periodic, allows light waves to be contained below the light line in the field of integrated optics.

Theoretical studies have demonstrated that the first (or Bragg) PBG can disappear in a periodic thin film in 1D for TM modes (with the electric field perpendicular to the film). However, this study was 2D and did not include lateral confinement of the waves.

Here, we study a 1D photonic crystal with full transversal confinement formed by a set of silicon nanobricks and show that the Bragg PBG for TE-like modes can vanish under proper conditions. We choose this system because it allows for easy analysis of the

unit cell and can be easily fabricated using standard silicon micro- and nanofabrication tools, as shown in recent experiments [109–111]. Notably, interchanging the thickness and the width of the nanobricks should also lead to the closure of the PBG for TM-like modes, in contrast to the case addressed in [84]. To explain the closure, and since we cannot describe the system analytically, we adopt a strategy different to [84] and consider the electric and magnetic Mie resonances of the isolated nanobricks. Our results suggest that the interplay between both Mie resonances and the Bragg resonance leads to PBG closure, resulting in a metamaterial-like behavior of the periodic structure.

5.2 Numerical simulations

We consider a periodic structure made of high-index ($n = 3.5$) nanobricks with the dimensions of w_x, w_y, and w_z surrounded by air (see Fig. 5.1). The structure is periodic along the x axis (period a), whilst confinement of guided waves in the y and z direction is ensured by TIR.

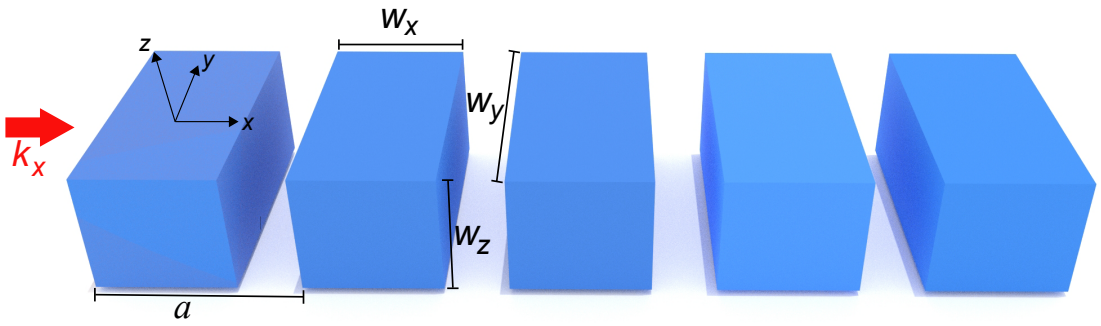

Figure 5.1: Sketch of the 1D periodic systems under study: a chain of high-index dielectric nanobricks.

Figure 5.2**a** shows the photonic bands—calculated using the plane wave expansion method—of the TE-like (or z-even parity) modes for $w_z = 220$ nm, $w_y = 450$ nm, and $a = 455$ nm for three different values of w_x. Notice that, due to the addition of the confinement along the y direction, we cannot classify the guided modes into TE or TM since the three components of the electric and magnetic fields are now present [96]. Nonetheless, the modes are usually termed either TE-like (the main component of the transverse field is E_y) or TM-like (the main component of the transverse field is E_z) in integrated optics due to their resemblance to the 2D picture. When $w_x = 200$ nm (green curves), a wide TE PBG opens between the dielectric and the air bands, as expected for high-contrast periodic systems [78]. The same happens for $w_x = 320$ nm (blue curves), though the PBG is redshifted because of the larger amount of dielectric material in the unit cell.

When analyzing the intermediate case ($w_x = 260$ nm, purple curves) we observe that the PBG vanishes. This means that the PBG width is neither directly nor inversely proportional to the parameter w_x. To know more about this relation, we calculate the frequencies of the dielectric and air bands at the boundary of the first Brillouin zone. Notice that these frequencies establish the boundaries of the Bragg bandgap. The results, depicted in Fig. 5.2**b**, clearly show a crossing of the bands—or band flip [84]—delimiting

the Bragg PBG at $w_x \approx 258$ nm. This means that, counterintuitively, the PBG vanishes even though we have a high-index contrast system. In general, an increase in w_x results not only in a red-shift of the bands, but also in a modification of the width of the Bragg PBG that eventually closes. To establish the effect of the period on PBG closure, we performed calculations for other values of a. We observed that the PBG was effectively closed at $w_x = 248$ nm for $a = 430$ nm and at $w_x = 267$ nm for $a = 480$ nm, meaning that the effect was also observed for other periods of the lattice.

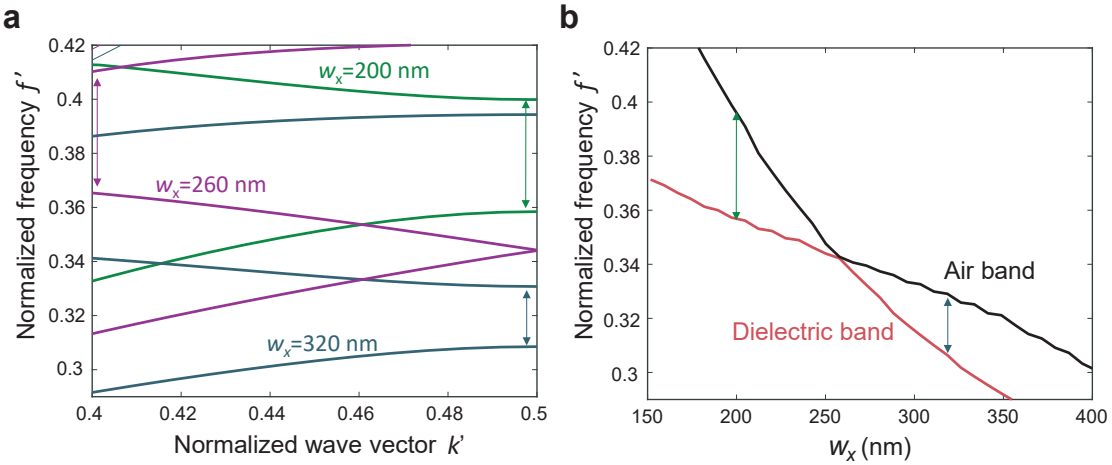

Figure 5.2: **a** Photonic bands for z-even parity (TE-like) modes for different values of w_x. **b** Frequencies of the dielectric and air bands as a function of w_x. Vertical arrows show the PBG for each value of w_x (for $w_x = 260$ nm a higher-order PBG is shown). The numerical simulations were performed for a 1D periodic chain of nanobricks with index $n = 3.5$ and dimensions $w_z = 220$ nm, $w_y = 450$ nm and $a = 455$ nm. The normalized frequency f' is given in units of $\omega a/2\pi c$, ω being the angular frequency and c the speed of light in vacuum. The normalized wave vector k' is given in units of $2\pi k/a$.

In comparison to the results in [84], we may argue that we now have TIR confinement in the lateral direction, which resembles the TE case found there. Indeed, by interchanging w_z and w_y in our periodic system (or rotating the structure 90° around the x axis), we should find that the PBG closes for TM-like (or z-odd parity) modes, meaning that the first PBG can be closed irrespective of the type of mode.

We also tested the vanishing behavior of the PBG using fully 3D FDTD simulations. The normalized intensity (square of the electric field at the center of the waveguide) after transmission along a chain of 10 nanobricks using rectangular waveguides of width w_y and thickness w_z for different values of w_x is shown in Fig. 5.3. Normalization is performed with respect to the response of a single waveguide. Notice that intensities over 1 (0 dB) are because the electric field is monitored locally, so resonant effects (such as Fabry–Perot fringes close to the PBG regions) can lead to large local intensities, though the normalized transmitted power is always lower than 1. In agreement with Fig. 5.2**a**, whilst broad dips appear for $w_x = 200$ nm and $w_x = 320$ nm at the expected frequency bands, there is not any observable dip for $w_x = 260$ nm (the fall in transmission above f' corresponds to higher-order PBGs, as shown in Fig. 5.2**a**).

To obtain further insights into the closure of the Bragg PBG, we obtained the main components of the transverse electric field at $k' = 0.5$ for the dielectric and air bands

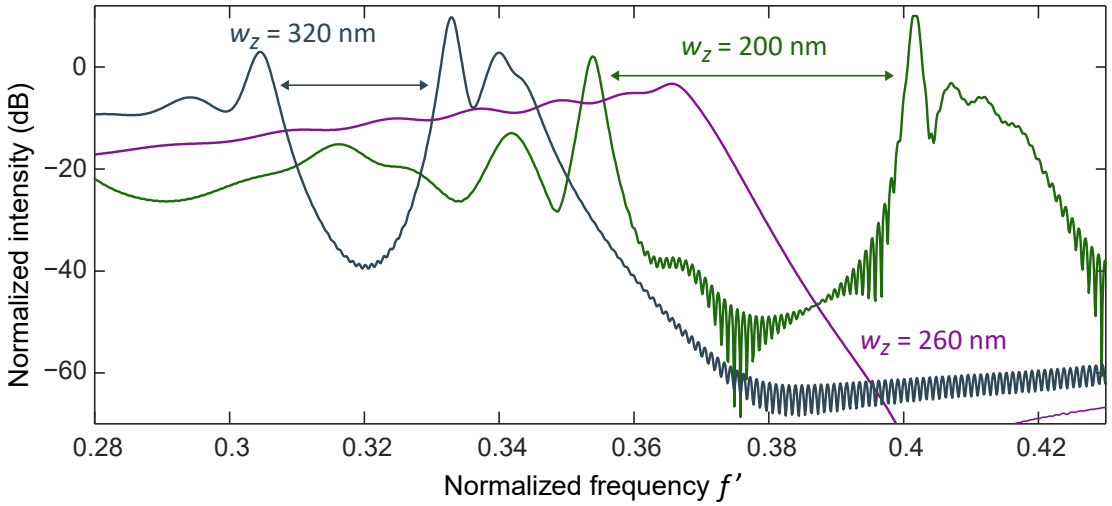

Figure 5.3: FDTD-calculated normalized intensity after transmission along a chain of 10 nanobricks using waveguides as input and output ports for w_x = 200, 260 and 320 nm. The results are normalized with respect to the transmission along a perfect rectangular waveguide. The trend is as follows: the PBG (highlighted by the horizontal lines with arrows) shifts to lower frequencies when w_x increases and disappears at $w_x \approx 260$ nm.

at different values of w_x. The results are illustrated in Fig. 5.4. For w_x = 200 nm, the dielectric band is characterized by a x-even parity transverse electric field (Ey) closely resembling an electric dipole pointing along y. The air band shows an opposite behavior in terms of parity, and the electric field patterns correspond to those of a magnetic dipole oriented along z (the magnetic field pattern is not shown here for the sake of simplicity). For w_x = 320 nm, the situation completely reverses; now, the dielectric (air) band has a magnetic (electric) dipole character. Therefore, it is the transition from electric to magnetic Mie resonances of the isolated nanobricks that explains the closure of the Bragg PBG. Indeed, the bandgap is closed because, for certain dimensions of the system, the Mie electric and magnetic resonances of the isolated nanobrick become degenerate at a frequency within a Bragg PBG.

To support this explanation, we calculated the frequencies of the ED and MD responses of isolated nanobricks as a function of w_x, following the approach in [104]. The results, depicted in Fig. 5.5, show that for small values of w_x the frequency of the ED is smaller than that of the MD, and this feature is inherited by the dielectric and air bands when the periodic system is formed. When w_x increases, the frequency of the MD decreases faster than that of the ED, resulting in the crossing of the Mie resonances, which are related to the band flipping and PBG closure in the periodic system. Indeed, even though we have only studied the effects of the w_x variation for simplicity, we can state that, for a given target frequency, there will be a triplet of (w_x, w_y, w_z) values for which the ED and MD resonances are degenerate. Therefore, it will be always possible to design a 1D periodic system with a closed bandgap at a certain wavelength. Moreover, if the degeneracy is achieved for a nanobrick with $w_z = w_y$, the Bragg PBG will be closed for both TE and TM modes simultaneously as a result of the symmetry of the system.

Notice that the crossing of the ED and MD of the isolated nanobricks takes place for a w_x value smaller than that obtained for the PBG closure. However, this can be

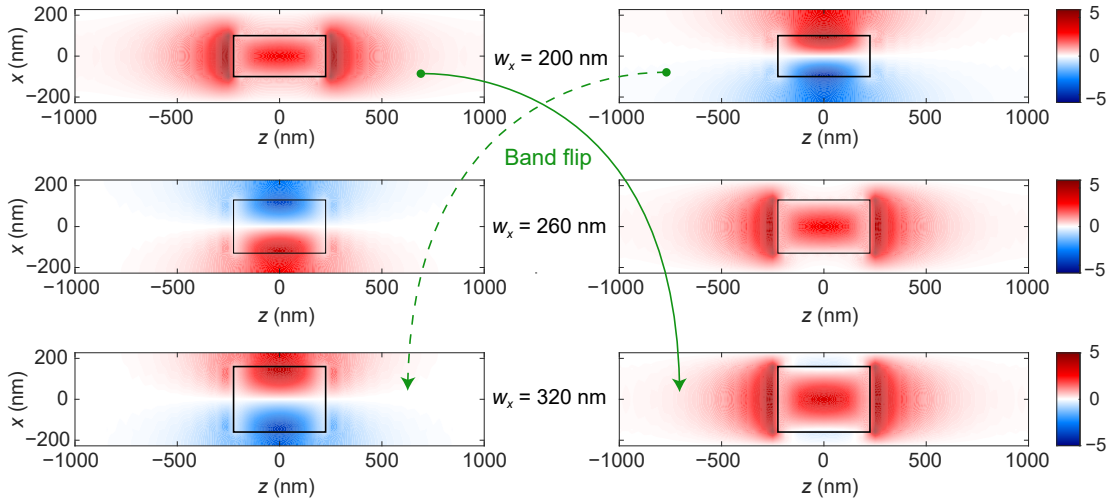

Figure 5.4: E_y field maps at the boundary of the first Brillouin zone for the dielectric (left column) and air (right column) bands at different values of w_x. For $w_x = 260$ nm (middle panels) the frequency difference between the two bands is negligible, meaning that they are close to the degeneracy point [112].

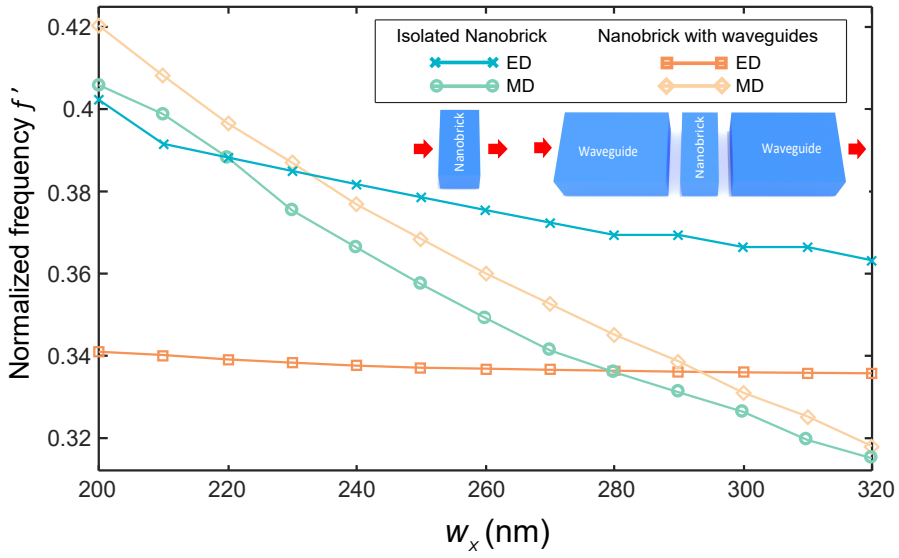

Figure 5.5: Calculation of the electric and magnetic dipole frequencies of an isolated nanobrick as a function of w_x obtained from a multipole decomposition. The orange and yellow curves show the frequencies of the maximum E_y and H_x at the nanobrick center when the nanobrick is embedded in a waveguide gap (illumination and collection using the TE-like mode of the waveguide ports). Inset: scheme of the illumination of the silicon nanobrick for each result.

explained because the isolated nanobrick is surrounded by a vacuum; when forming the chain part of the field, the electromagnetic field penetrates the neighboring nanobricks, resulting in a perturbation of the modes. To account for the additional presence of dielectric material, we calculated the frequencies of the ED and MD corresponding to

the maximum of the electric field and the magnetic field at the center of the nanobrick, respectively; this occurred when a single nanobrick was embedded in a waveguide gap of a length equal to a (see Fig. 5.5). The results, also shown in Fig. 5.5, indicate that, now, the flip frequency is red-shifted and the crossing point shifts to larger values of w_x.

5.3 Experimental measurements

To confirm our numerical predictions, different samples containing sets of nanobricks chains with waveguides as input and output ports were fabricated using standard fabrication tools (see Appendix B) following the configuration sketched in Fig. 5.1. Figure 5.6 shows SEM images of some fabricated circuits with different w_x values, highlighting in detail the waveguide ends acting as input and output ports, as well as the nanobricks chains. The waveguides were adiabatically widened up to 3 µm to reduce coupling losses from the input lensed fiber as well as to the output detection system [27] (see Appendix C).

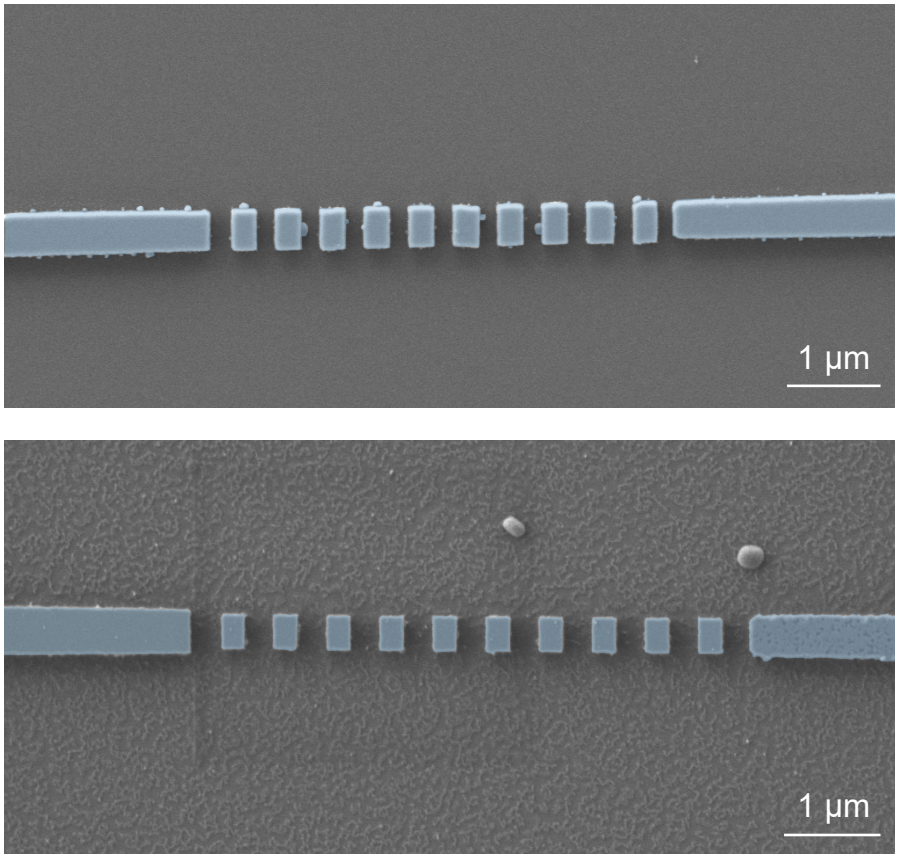

Figure 5.6: **False-color SEM micrographs of two fabricated circuits.** Fabricated chain for ten nanobricks with **a** $w_x = 260$ nm, $w_y = 450$ nm, $w_z = 220$ nm, $a = 480$ nm and **b** $w_x = 260$ nm, $w_y = 400$ nm, $w_z = 220$ nm, $a = 550$ nm. Rectangular cross-section waveguides are employed as input and output ports.

We also performed numerical simulations including the silica substrate (Fig. 5.7**a**) to compare the results of the experimental measurements. Figure 5.7 shows the **a** numerical

and **b** experimental transmission for ten chains with nominal w_x varying between 240 and 330 nm, $w_y = 350$ nm, $w_z = 220$ nm and $a = 380$ nm. In Fig. 5.7**a** we clearly observe the closure of the bandgap as w_x increases, but we could not see it in the experimental measurements. Due to fabrication problems (in particular, in the etching of the silicon layer), we could not reproduce exactly the designed devices, and this seems the main reason that prevented us to observe the PBG closure. Improving the etching should lead to better samples that enable the experimental observation of the predicted effect.

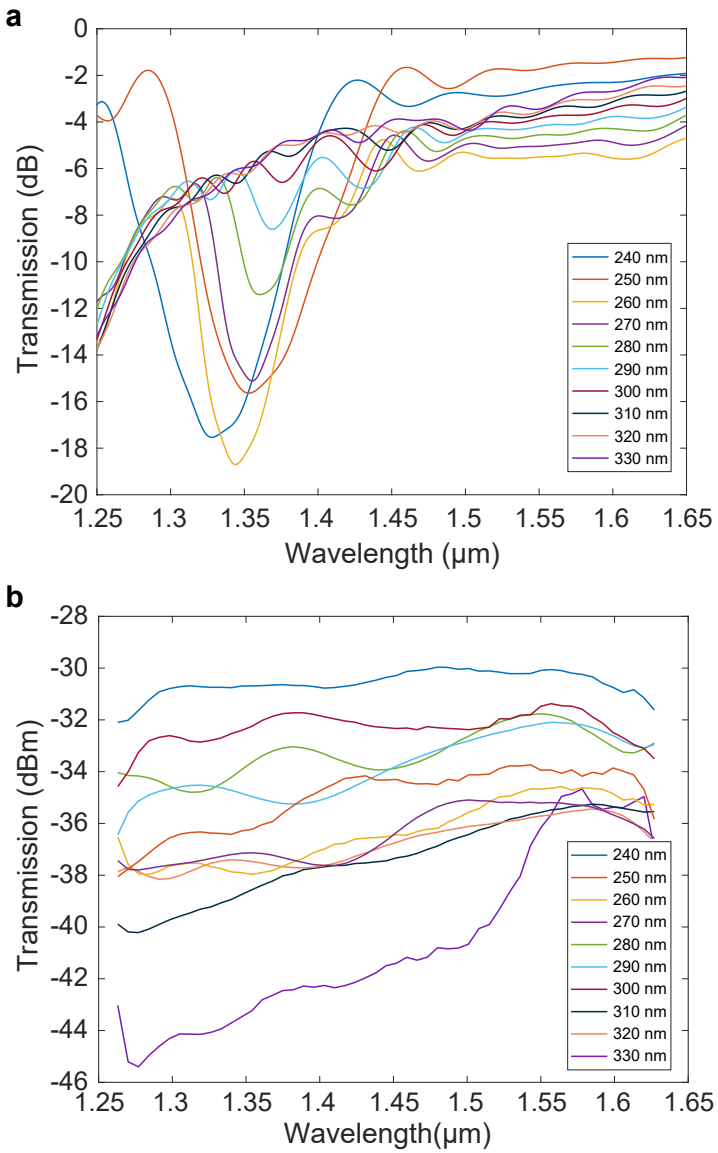

Figure 5.7: **Light transmission along chains of nanobricks.** **a** Numerical and **b** experimental transmission along chains of ten nanobricks with different w_x (nominal values shown in the panels), $w_y = 350$ nm, $w_z = 220$ nm and $a = 380$ nm. To reproduce the experimental conditions, we have considered that the silicon nanobrick lies on a silica substrate in the simulations.

Our results highlight the importance of the properties of the isolated unit cell when forming 1D lattices of high-index dielectric materials [29]. Noticeably, when the Mie

resonances of the unit cell dominate over the periodic response, the structure could, in principle, be considered as an all-dielectric metamaterial [113]. However, looking at the classification proposed in [114], the PBG closure takes place just when the Bragg wavelength equals the ED and MD wavelengths, meaning that we are just at the frontier separating the photonic crystal and metamaterial phases. Indeed, in the 2D periodic systems arranged in a square lattice studied in [114], which require very large indices to reach the metamaterial phase, the use of a hexagonal lattice [115] would allow one to obtain a "metamaterial" behavior in 2D silicon photonic crystals. Our results show that such metamaterial behavior naturally arises in a realistic 1D photonic crystal made of silicon nanobricks at bands placed below the light cone, which would ensure lossless performance. This behavior is manifested by the fact that the overlapping of the electric and magnetic dipolar Mie resonances closes the Bragg PBG, which is the fundamental feature of a photonic crystal.

Chapter 6

Conclusions and future work

Throughout this chapter, we summarize the results obtained in the thesis, which was aimed at the numerical and experimental investigation of the excitation of different electromagnetic multipoles in small silicon disks at telecom wavelengths and under lateral illumination. Our conclusions are drawn based on the initial objectives, and the lines of future work are sketched.

In chapter 2 we addressed the first-order electric anapole in silicon disks when driven laterally by integrated waveguides. This anapole arises from the interference between the ED and the toroidal dipole. These were our main findings:

- We demonstrated that the excitation of a radiationless anapole state in a silicon disk exhibits remarkable differences when excited on chip, i.e., from the side, in comparison with the commonly used normal incidence approach.
- Interestingly, the anapole condition and the maximum field energy inside the disk occur at well-separated wavelengths. We attributed this phenomenon to the large size (of the order of the wavelength) of the disk in the excitation direction, so retardation effects play a role in the multipolar decomposition. Besides numerical simulations, far- and near-field experiments confirmed this observation.
- Measurement of far-field out-of-plane scattering confirmed the existence of a wavelength region with suppressed scattering around the predicted anapole wavelength. Indeed, at such wavelengths, the recorded scattering is smaller than when there is no disk in the system. As expected from the simulations, the minimum scattering wavelength can be tuned by changing the disk radius.
- Near-field measurements confirmed that the maximum concentration of energy inside the disk was red-shifted in comparison to the anapole condition. Still, it was observed the local electric-field vortices have a different sense of rotation at each side of the disk, as expected from toroidal excitations widely reported in the literature. Notably, the two vortices changed from being symmetric (in amplitude) at the anapole condition to highly asymmetric at the maximum-energy region.

In chapter 3 we went a bit further and by making the disks bigger we showed that the use of integrated waveguides for on-chip excitation of wavelength-sized silicon disks enabled the observation of higher-order anapoles under in-plane illumination.

- In particular, for the second-order electric and the first magnetic anapole, a strong reduction in the top scattering of a single disk illuminated laterally from a nearby waveguide was predicted from numerical simulations and confirmed in experimental measurements.

- Completing the results in Ref. [104], some differences between normal and in-plane excitation were observed. Remarkably, for the second-order electric anapole the condition $P + T_{\mathrm{P}} = 0$ was not satisfied under in-plane illumination, which we also attribute to retardation effects in the disk. Still, these results showed that the out-of-plane scattering is severely reduced, which is an important feature in the practical use of anapole states in on-chip integrated photonics.

- The use of the TM-like mode enabled the observation of the magnetic anapole. Notably, in this case, the scattering was recorded for the longitudinal component of the guided electric field, which is the radiative component when the vertical dipolar moment is excited. Moreover, further engineering of the disk could eventually lead to hybrid anapoles, where the far-field scattering arising from the spherical electric and magnetic dipoles is simultaneously cancelled [54].

The results described in chapters 2 and 3 highlight the utility of this approach (on-chip excitation) for driving complex photonic states in wavelength-scale photonic elements. Indeed, by mixing TE and TM modes in the waveguide and changing the position between the waveguide termination and the disk, it could become possible to excite other complex states based on mode interference [60, 116] for on-chip photonics. Moreover, these findings may have important consequences when trying to employ anapole states for sensing or nonlinear applications in on-chip nanophotonics [117], either implemented in silicon or other high-index materials.

In chapter 4 we went from isolated disks to 1D groups and analyzed numerically and experimentally the guidance of light along periodic chains of silicon disks in the telecom wavelength regime. The main results were:

- We found that chains of perfect disks do not transport energy at wavelengths corresponding to the electric anapole state described in chapter 2. This observation is indeed consistent with the fact that the disk does not efficiently scatter radiation at the anapole wavelength and, therefore, cannot excite the next adjacent disk.

- When the disk was split into two halves by an air gap of width G, energy transportation along chains was relatively large, even when building bent chains. Remarkably, this happened at frequencies placed over the light line when coupling to radiative modes was enabled.

- Multipolar decomposition, as well as near-field patterns obtained by simulations, led us to suggest that it is the toroidal dipole responsible for the guidance, whereas the excitation of the magnetic quadrupole contributes to the reduction of out-of-plane scattering [107, 108].

- Calculations of the Q factor of an infinite chain showed that the large transmission could also be interpreted as a leaky resonance in the continuum, but there are no evident signatures of a BIC. Indeed, it could be envisaged that further engineering

of the disk could lead to the emergence of accidental BICs in 1D periodic systems. Such states should be experimentally observable as high-Q resonances under lateral waveguide excitation without recurring to complex methods for vertical excitation [118]. Experimental measurements on samples fabricated using standard silicon nanofabrication tools confirmed the simulation results and paved the route toward new applications of scatteringless states in chains of dielectric scatterers.

As a future line of research, it would be highly interesting to design and measure longer chains to study the losses in detail and show if lossless media fabrication is possible. Also, to minimize the losses due to curvature, it would be interesting to optimize the curvature of the chains.

In chapter 5 we addressed the light guidance along a periodic chain of dielectric scatterers but now at frequencies below the light line. We showed that the interplay between the electric and magnetic dipole resonances of a single nanobrick can lead to the closure of the Bragg PBG for guided modes when forming a 1D photonic crystal.

- This result is somewhat counterintuitive since, in principle, one may expect that any 1D periodic lattice should induce a forbidden band for waves propagating in the direction of the periodicity. Even though a very simple structure has been analyzed, the performance should be the same if the unit cell supports electric and magnetic resonances so that a band flip might arise under certain conditions. Importantly, the same effect should be observed in chain of silicon disks, as the one addressed in the previous chapters of this thesis.

- Noticeably, the PBG only vanishes for a perfect photonic crystal, so any tiny perturbation can open the PBG. This could be used to build active or tunable devices where the properties of a single nanobrick can be actively modified using electrical, optical, or even mechanical means.

It would be interesting to achieve the manufacture of perfect chains to experimentally demonstrate the results shown here due to this finding could lead to advances in the design of subwavelength integrated photonic devices [119] for application in signal processing, communication systems, or bio- and chemo-sensing. Notably, the resulting devices could be easily manufactured using mainstream silicon photonic technology.

A future line that applies to all of our previous results would be the use of high-index disks illuminated laterally to observe non-linear effects such as harmonic conversion or four-wave mixing, which has been reported to be highly efficient when exciting the disks from the top using FS light beams. The on-chip excitation could lead to all-optical processing at telecom wavelengths in ultra-compact footprints using relatively low input powers.

Appendices

Contents

A Numerical Simulations

In this Appendix, we briefly described the different numerical tools employed in the realization of this thesis.

Some numerical simulations presented in this thesis have been performed using the commercial 3-D full-wave solver CST Microwave Studio, which implements a finite integration technique (FIT). The FIT approach involves resolving Maxwell's equations in integral form, in contrast to most numerical methods that solve them in a differential form. It is important to discretize the calculation domain of the considered problem in order to numerically solve these equations. Therefore, to divide the issue into cells, a suitable mesh is required. A hexahedral mesh with 10 cells per wavelength has been applied to the architectures presented in this thesis. To model the silicon structures, a refractive index $n = 3.45$ has been considered. Open boundary conditions (perfectly matched layer) have been selected for external facets. In some cases, the system has been considered to be surrounded by air, and in others that it rests on a SiO_2 substrate. Field monitors have been used to observe the fields through and around the disk.

Some numerical results presented in this thesis were obtained via three-dimensional finite difference time domain (3D-FDTD) simulations (RSoft tool by Synopsys) as for example in Figs. 2.5**a,b**, 2.6 as well as the scattering under waveguide illumination in Fig. 2.2**a,c**. The software included material modes for silicon and silicon dioxide (substrate) that were employed in the simulations. The spectra in Fig. 2.5**a,b** were obtained as the Fourier transform of the electric field monitored either at a 2 µm distance from the disk center or at the disk center with and without disk to get the normalized response after exciting the TE mode of the waveguide with a pulsed signal centered at 1550 nm. Perfectly matched layers were applied at the boundaries of the simulation domain. The height to monitor the scattering, whilst not being truly far field, was chosen to avoid very time-consuming computations. In Fig. 2.6, the energy in the silicon disk, in a cylinder (thickness 50 nm, radius equal to the silicon disk) placed 50 nm on top of the disk surface, and in a cylinder (thickness 50 nm, radius equal to the silicon disk) placed 2 µm on top of the disk surface were monitored for different wavelengths of the input TE mode.

Electromagnetic multipole calculations, spectra representing the energy inside the disk and on the disk surface, and the electric and magnetic field intensity at the disk center shown in this thesis were performed by Dr. Ángela I. Barreda by means of a finite-element method implemented in the commercial software COMSOL Multiphysics. In particular, we used the Radio Frequency Module that allows us to formulate and solve the differential form of Maxwell's equations (in the frequency domain) together with boundary conditions. The disks are placed at the center of a spherical homogeneous region filled with air, whose radius is $\lambda/2$. A perfectly matched layer domain, with thickness $\lambda/4$, is positioned outside of the embedding medium domain and acts as an absorber for the scattered field. The mesh is chosen sufficiently fine as to allow numerical convergence of the results. In particular, the element size of the mesh of the embedding medium is smaller than $\lambda/5$ and that of the particles is smaller than $\lambda/[3\Re(n)]$, being n the silicon refractive index. The different multipolar contributions were obtained by integrating the displacement current induced inside the nanoparticle. The energy inside the disk corresponds to the volume average of the energy density time average at the disk volume. The energy on the disk surface was attained by means of the surface average of the energy density time average at the top surface of the disk.

B Fabrication

The samples of the designs under study in this thesis have been fabricated in the cleanroom of the Nanophotonics Technology Center at Universitat Politècnica de València. Electron-beam lithography has been done by Dr. Amadeu Griol.

The fabrication process can be described as follows. Standard silicon-on-insulator samples with top silicon layer thicknesses of 220 nm (Chapters 2, 4, 5) and 330 nm (Chapter 3) and a buried oxide layer thickness of 2 µm were used to build silicon structures. An electron-beam direct-writing procedure was used to define patterns on a coated 100 nm hydrogen silsesquioxane (HSQ) negative resist layer. Utilizing an acceleration voltage of 30 keV and an aperture size of 30 µm, the electron-beam exposure, carried out with a Raith150 tool, was tuned to achieve the required dimensions. The resist patterns were then printed onto the samples using an improved inductively coupled plasma-reactive ion etching (ICP-RIE) method utilizing fluoride gases (CF4 and C4F8) after the HSQ film had been developed with tetramethylammonium hydroxide.

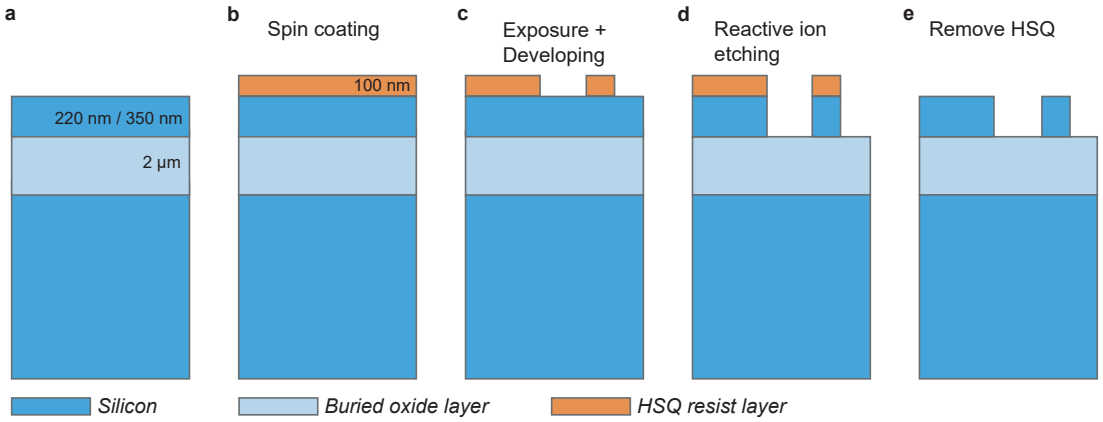

Figure B1: Scheme of different steps of the fabrication process. **a** Standard silicon-on-insulator samples with top silicon layer thicknesses of 220 nm / 330 nm and a buried oxide layer thickness of 2 µm. **b** Negative HSQ resist spin-coating. **c** Exposure and developing. **d** Reactive ion etching. **e** Remove HSQ film.

For the development of this thesis, many samples were fabricated that, being measured in the laboratory and not yielding the expected results, were redesigned and later fabricated until the measured results were similar to those obtained from simulations. Below are details of the final samples measured to obtain the results shown in chapters 2, 3, and 4.

B.1 Samples of Chapter 2

Below are details of two fabricated samples, each one having three circuits with disks of nominal radius 325, 350, and 375 nm for studying the first electric anapole. The samples were characterized by SEM and the actual dimensions of the disk measured, with sample 1 used for far-field measurements in Fig. 2.10, and sample 2 for far-field measurements in Fig. 2.12 and near-field measurements in Figs. 2.13 and 2.14.

	Sample 1			Sample 2		
Nominal disk radius r	325 nm	350 nm	375 nm	325 nm	350 nm	375 nm
SEM estimated x-axis	305 nm	320 nm	350 nm	297 nm	327 nm	355 nm
SEM estimated y-axis	310 nm	323 nm	359 nm	305 nm	332 nm	358 nm

Table B.1.1: Dimensions of samples measured in Chapter 2.

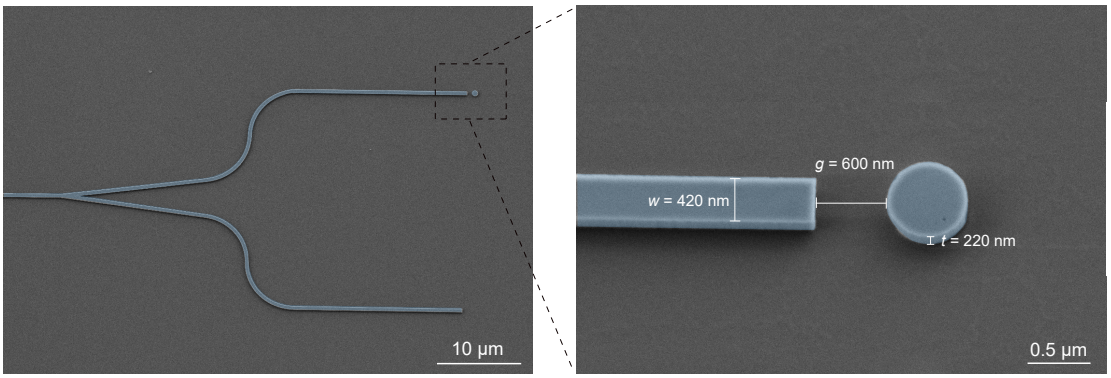

Figure B.1.1: False-color SEM micrograph of one fabricated circuit. Disk radius 350 nm.

B.2 Samples of Chapter 3

Details of two fabricated samples are described below, one having three circuits with disks of nominal radius 525, 550, and 575 nm for studying the second electric anapole and the other having four circuits with disks of nominal radius 350, 375, 400, and 425 nm for studying the magnetic anapole.

	Sample 1			Sample 2			
Nominal disk radius r	525 nm	550 nm	575 nm	350 nm	375 nm	400 nm	425 nm

Table B.2.1: Dimensions of samples measured in Chapter 3.

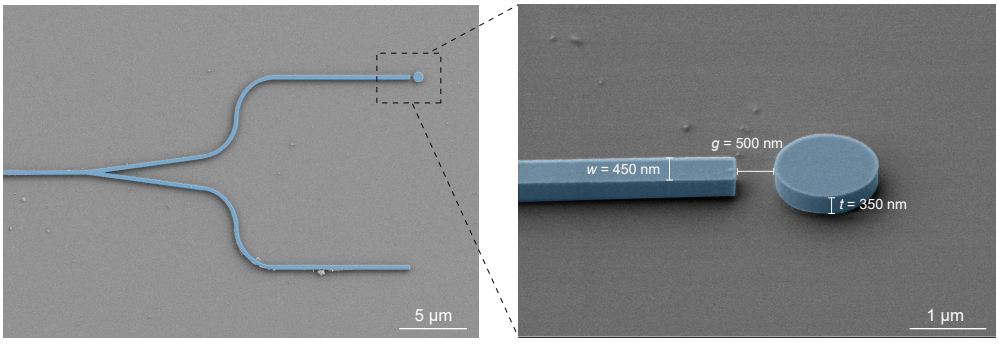

Figure B.2.1: False-color SEM micrograph of one of the fabricated circuit for the study of the second electric anapole. Disk radius 550 nm

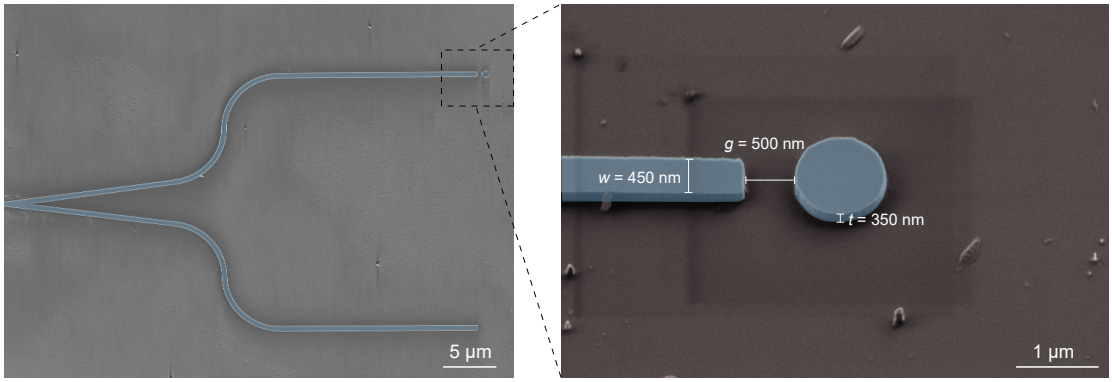

Figure B.2.2: False-color SEM micrograph of one of the fabricated circuit for the study of the magnetic anapole. Disk radius 425 nm.

B.3 Samples of Chapter 4

Samples containing sets of straight and bent chains with three different air gaps: $G = 0$, $G = 0.5$r, and $G = 0.9$r, each for two different nominal radii disks (shown in the table below) were fabricated to study the guidance of light through chains of disks.

	Straight chains		Bent chains					
	$G = 0.5r$		$G = 0$		$G = 0.5r$		$G = 0.9r$	
Estimated disk radius r	400 nm	425 nm	185 nm	215 nm	400 nm	425 nm	500 nm	525 nm

Table B.3.1: Dimensions of samples measured in Chapter 4

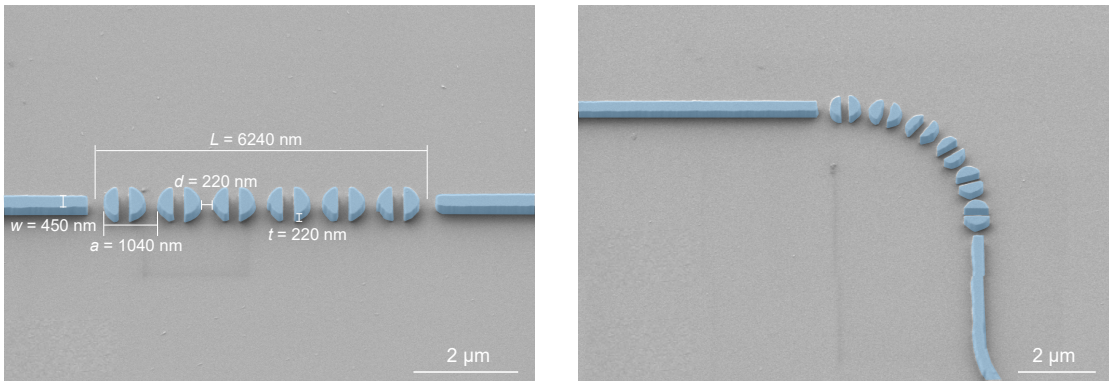

Figure B.3.1: False-color SEM micrograph of some of the fabricated chains (straight (left) and bent (right)) with air gap $G = 0.5r$.

C Experimental set-up

In this section, we describe the optical set-up (Fig. C1) used to obtain the experimental results presented in this work. The configuration corresponding to the horizontal path has allowed us to perform the transmission measurements and the vertical path the scattering measurements.

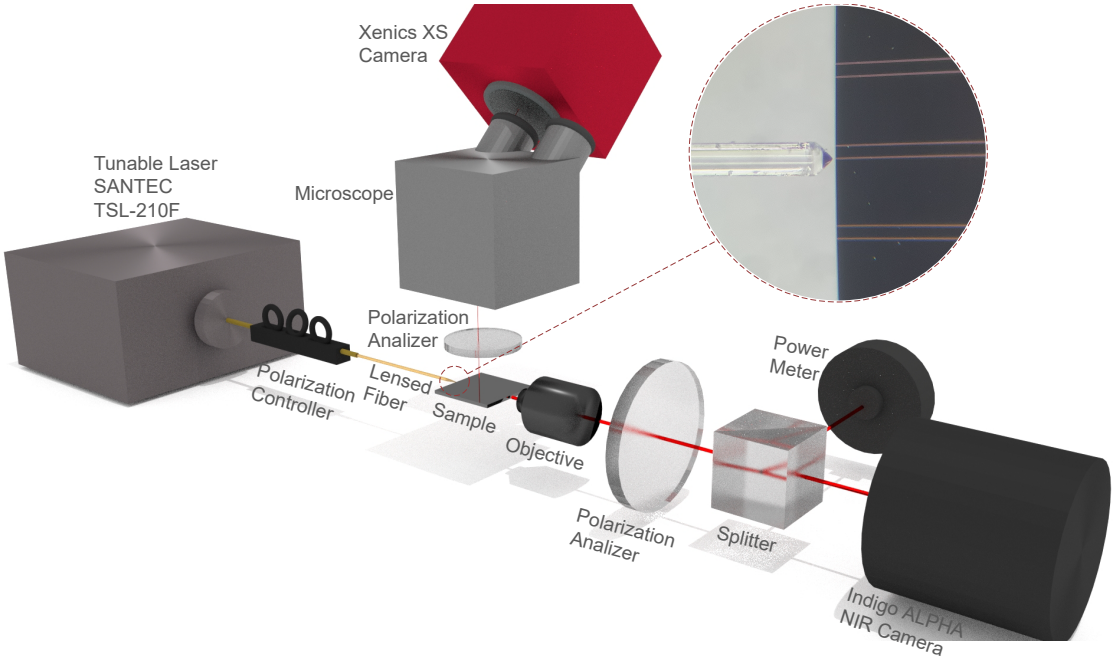

Figure C1: Scheme of the optical set-up used in the experimental measurements. Inset: Close view of the lensed fiber coupled to a waveguide.

First, a tunable laser SANTEC TSL-210F covering the range between 1260 nm and 1630 nm is used as a light source. A fiber polarizer was used to ensure that only a TE/TM-like mode was excited in the input waveguide, which was carried out via a lensed fiber. The lensed fiber and the sample were placed in positioning platforms which allow for aligning the input fiber with each waveguide included in the sample. Scattered light was captured with a stereoscope optical microscope (model 420-1105-10, National Optical & Scientific Instruments Inc. with effective numerical aperture NA $\approx$ 0.1 and high resolution, achromatic, color corrected lenses suitable for IR measurements) and detected in a Xenics XS infrared camera (model XS-1.7-320), which is equipped with a standard InGaAs detector that has a quantum efficiency between 85-100% between 1250 nm and 1650 nm (100% between 1450 nm and 1650 nm). A polarizing filter was added to the vertical path to select the right polarization in each case: E_y (perpendicular to the excitation direction) for the TE mode and E_x (parallel to the excitation direction) for the TM mode. An averaging of seven intensity measurements per wavelength was carried out to reduce the ripple in the measured scattering and then a smoothing of the data was performed by "polyfit" and "polival" Matlab functions, as previously done in [28].

In Fig. C2 we can see a photo of the setup used to perform the experimental measurements. The main elements of the system have been highlighted.

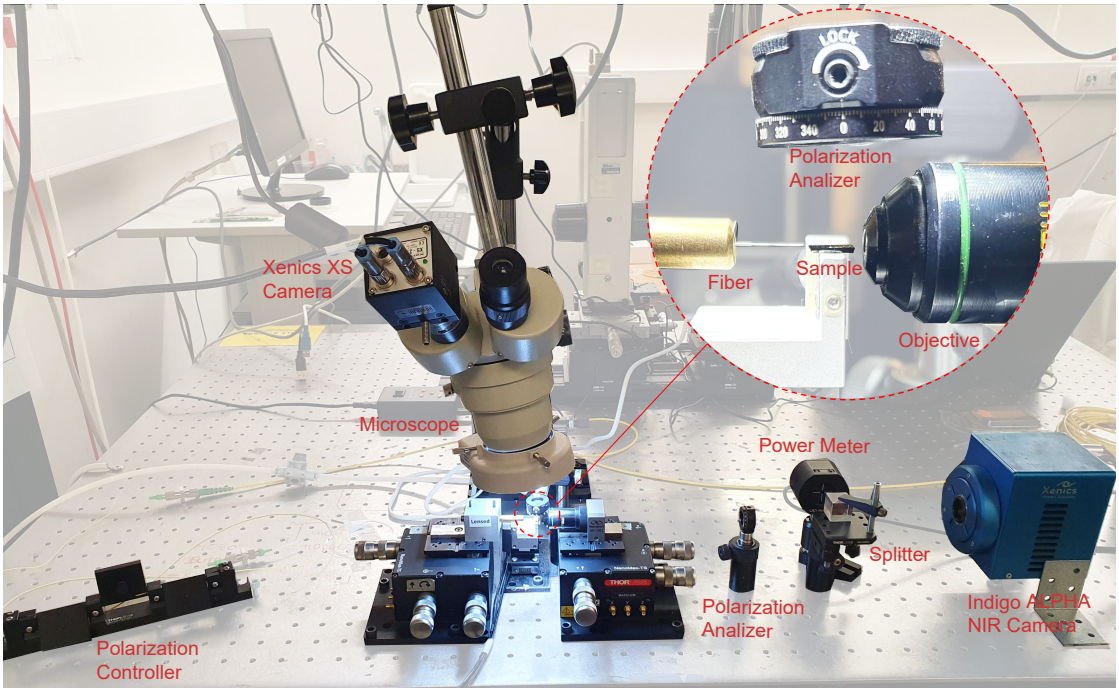

Figure C2: Photo of the set-up, highlighting the main elements of the measurement system. Inset: Details of the polarization filter used for scattering measurements and the lensed fiber, sample and objective coupled.

C.1 System alignment process

However, to perform the measurements, we must first check that the system is correctly aligned. In the alignment process, we will have two different scenarios:

1. Fiber-objective alignment

   First, we bring the lensed fiber and the objective close together (Fig. C.1.1) and move in the coordinates x, y, z looking for the light spot (Fig. C.1.3-1) as the output signal, in order to maximize the transmission. Here, we characterize the losses of the system to correctly address the normalization of the transmission measurements that we will perform once the system is aligned. In Fig. C.1.3 we can see a sketch of the alignment process. The left panel shows the main elements involved, and on the right side, we can see the output signal captured by the objective.

2. Fiber-sample-objective alignment

   We place the sample in the middle in order to inject (and collect) the laser signal in (and from) the sample to perform the transmission and scattering measurements. The procedure is as follows: First, we separate the lensed fiber from the objective and, in the middle, we put our sample. Then, we place the fiber and the objective higher than the sample (Fig. C.1.3-2), which allows us to obtain the light diffraction patterns as the output signal, as can be seen in the right part of the figure. Next, we move the objective towards the sample in the z direction (Fig. C.1.3-3) until half of our output signal is made up of the diffraction patterns. At this point, we

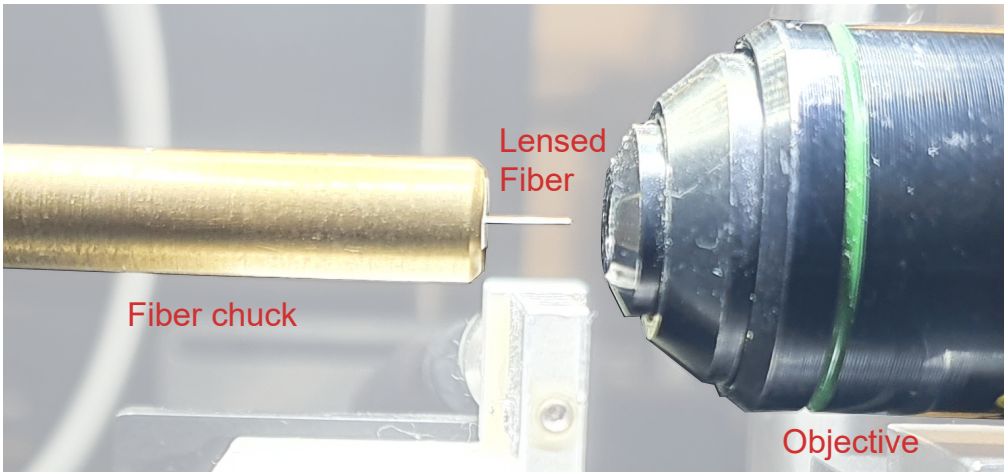

Figure C.1.1: Photo of the lensed fiber and objective coupled.

adjust the position of the objective in the x direction in order to obtain well-defined patterns. Subsequently, we displace the fiber in the z axis (Fig. C.1.3-4) and, when the patterns disappear, we adjust the objective in the y direction until we observe the spot of light as can be seen on the right part of the Fig. C.1.3-4. Finally, it only remains to make fine adjustments to both the fiber and the objective to achieve the maximum signal at the output of our system, monitoring the transmitted power. The result of the system alignment process is sketched in Fig. C.1.2, where it can be seen that the fiber has been aligned with the sample and the objective.

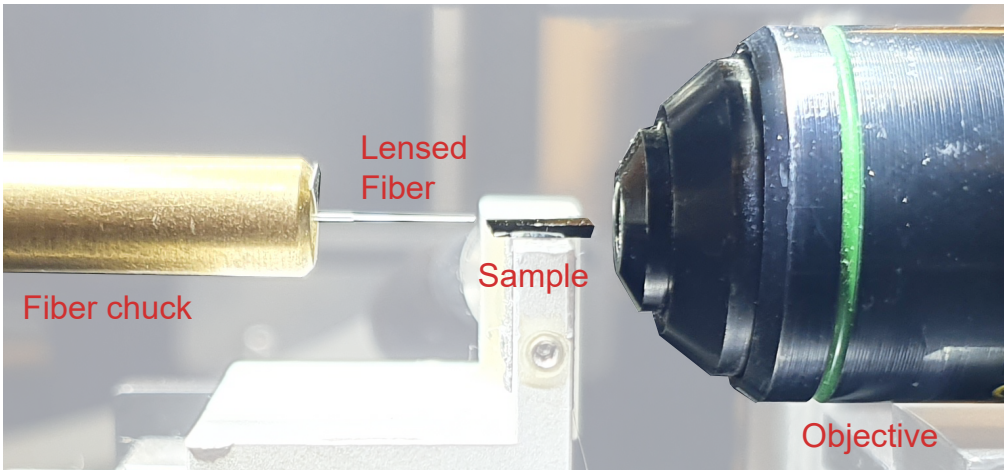

Figure C.1.2: Photo of the lensed fiber and objective coupled.

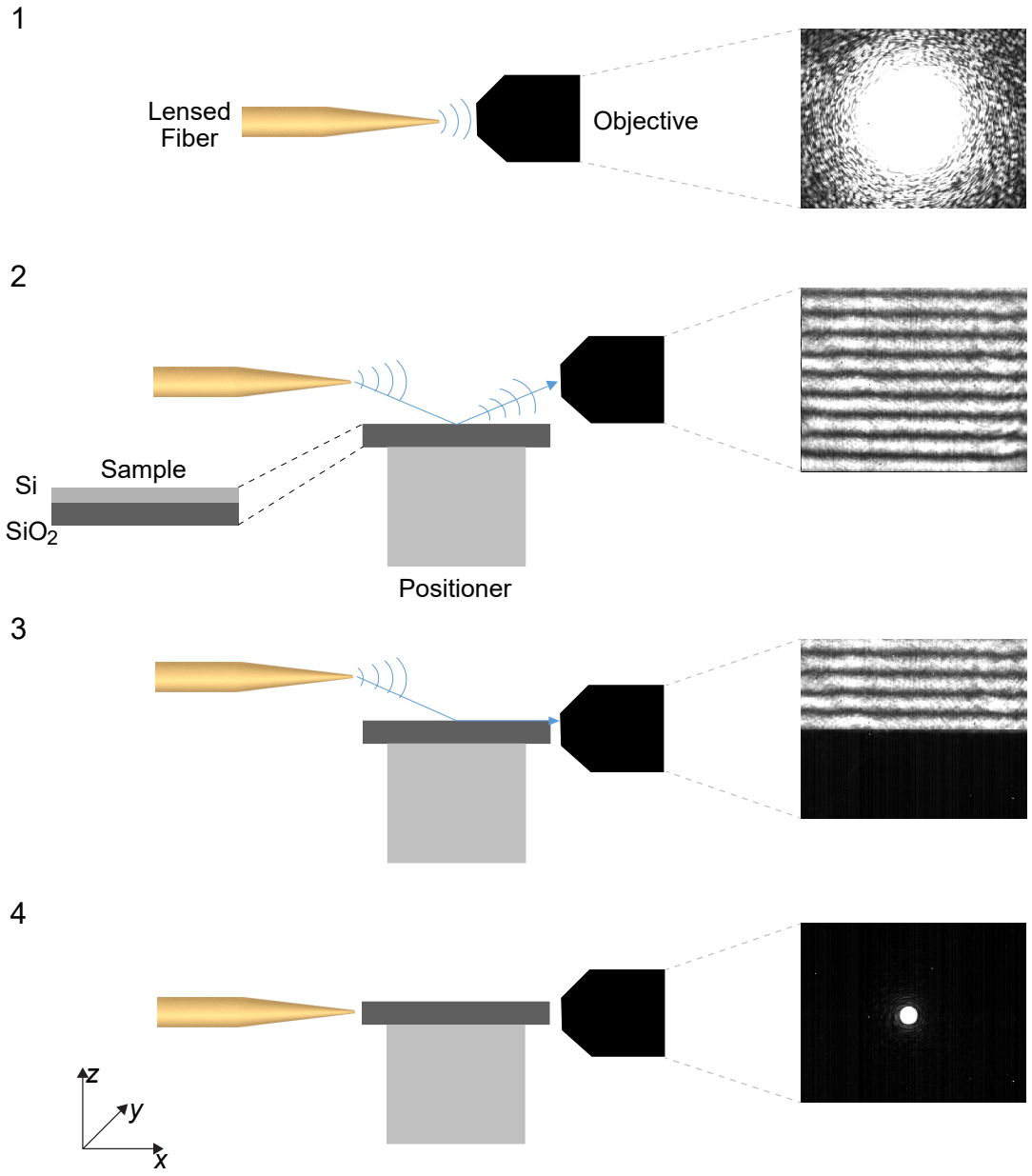

Figure C.1.3: Schematic illustration of system alignment process.

D Near-field optical measurements

Near-field measurements reported in Chapter 2 were performed at the Delft University of Technology (The Netherlands) by Dr. Thomas Bauer and Dr. Elena Pinilla in a home-build phase- and polarization-resolving near-field optical microscope. [100] The excitation light from a SANTEC TSL-710 laser was split into a signal and reference branch for interferometric phase detection, with the signal light being end-fire-coupled into the feed waveguide by a microscope objective. FS polarization control ensures that only the TE mode of the feed waveguide is excited. The aperture-based near-field probe

consists of a tapered single-mode optical fibre coated with 150 nm aluminium and an apex opening of 175 nm. The probe-to-sample distance is controlled via either shear-force feedback for scans on the surface of the sample, or optical height feedback via a SmarAct picoscale interferometer. The light collected through the fibre-based probe is combined with the reference beam in an optical fibre network, with the reference light frequency-shifted by 40 kHz to allow for heterodyne detection of the amplitude and phase of the collected signal. Polarization resolution is achieved by splitting the combined light beam into two orthogonal polarization components and separately detecting the amplitude and phase of the x- and y-component of the collected light field.

Due to the near-field probe exhibiting an electric and magnetic response, the retrieved near-field signal is a combination of both, in-plane electric and magnetic near fields. The complex tensors α and β quantifying the system response to in-plane field components are to first order given by diagonal (α) and off-diagonal (β) position-independent matrices combining the similar local field components E_x and H_y to one detection channel as well as E_y and H_x to the orthogonal detection channel. For the chosen probe type, the coupling coefficients in these matrices are virtually identical, with $\alpha_{xx} = \alpha_{yy} = Z_0\beta_{xy} = Z_0\beta_{yx}$, where Z_0 is the impedance of FS. [101]

E Author's Merits

E.1 Publications

- **E. Díaz-Escobar**, A.I. Barreda, L. Mercadé, A. Pitanti, A. Griol and A. Martínez, "Light guidance aided by the toroidal dipole and the magnetic quadrupole in silicon slotted-disk chains," *ACS Photonics* (2023).
- **E. Díaz-Escobar**, A.I. Barreda, A. Griol and A. Martínez, "Experimental observation of higher-order anapoles in individual silicon disks under in-plane illumination," *Applied Physics Letters*, **121**, 201105 (2022).
- **E. Díaz-Escobar**, L. Mercadé, A.I. Barreda, J. García-Rupérez and A. Martínez, "Photonic Bandgap Closure and Metamaterial Behavior in 1D Periodic Chains of High-Index Nanobricks," *Photonics*, **9**, 691 (2022).
- **E. Díaz-Escobar**, T. Bauer, E. Pinilla-Cienfuegos, A.I. Barreda, A. Griol, L. Kuipers and A. Martínez, "Radiationless anapole states in on-chip photonics," *Light: Science & Applications*, **10**, 204 (2021).

E.2 Conferences

- **E. Díaz-Escobar**, A.I. Barreda, A. Griol and A. Martínez, "Observation of higher-order anapole resonances in single silicon disks driven by integrated waveguides," in 12th International Conference on Metamaterials, Photonic Crystal and Plasmonics (*META 2022*) (Torremolinos, Spain, 2022).
- **E. Díaz-Escobar**, A. I. Barreda, L. Mercadé, A. Griol and A. Martínez, "Bandgap closure in 1D photonic crystals from interplay between Mie resonances," in 17th IEEE International Conference on Group IV Photonics (*GFP 2021*) (Online, 2021).
- **E. Díaz-Escobar**, T. Bauer, E. Pinilla-Cienfuegos, A.I. Barreda, A. Griol, L. Kuipers and A. Martínez, "In-plane excitation of anapole states in silicon disks," in XIII Reunión Nacional de Óptica (*RNO 2021*) (Online, 2021).
- **Evelyn Díaz-Escobar**, Elena Pinilla-Cienfuegos, Ángela I. Barreda, Laura Mercadé, Amadeu Griol and Alejandro Martínez, "Exotic nanophotonics with subwavelength high-index disks," in XXXVI Simposium Nacional de la Unión Científica Internacional de Radio (*URSI 2021*) (Online, 2021).
- **E. Díaz-Escobar**, T. Bauer, E. Pinilla-Cienfuegos, A.I. Barreda, A. Griol, L. Kuipers and A. Martínez, "Radiationless anapole states in on-chip photonics," in Spintronics, Photonics, Phononics or Magneto-Optics Online International Conference (*SPPM 2021*) (Online, 2021).
- **E. Díaz-Escobar**, E. Pinilla-Cienfuegos, T. Bauer, A. I. Barreda, A. Griol, L. Kuipers and A. Martínez, "In-Plane Driving of Anapole Resonances in Silicon Disks at Telecom Wavelengths," in 14th International Congress on Artificial Materials for Novel Wave Phenomena (*Metamaterials 2020*) (Online 2020).

Bibliography

[1] F. Namavar, G. T. Reed, and S. K. Toh. Optical waveguides in simox structures. *IEEE Photonics Technology Letters* **3**, 19–21 (1991)

[2] B. E. Little, J. S. Foresi, G. Steinmeyer, E. R. Thoen, S. T. Chu, H. A. Haus, E. P. Ippen, L. C. Kimerling, and W. Greene. Ultra-compact si-sio2 microring resonator optical channel dropping filters. *IEEE Photonics Technology Letters* **10**, 549–551 (1998)

[3] J. P. Lorenzo and R. A. Soref. 1.3 m electro-optic silicon switch. *Applied Physics Letters* **51**, 6 (1998)

[4] M. Lipson. The revolution of silicon photonics. *Nature Materials 2022 21:9* **21**, 974–975 (2022)

[5] Simply silicon. *Nature Photonics 2010 4:8* **4**, 491–491 (2010)

[6] M. Hochberg and T. Baehr-Jones. Towards fabless silicon photonics. *Nature Photonics 2010 4:8* **4**, 492–494 (2010)

[7] A. Rickman. The commercialization of silicon photonics. *Nature Photonics 2014 8:8* **8**, 579–582 (2014)

[8] T. Baehr-Jones, T. Pinguet, P. L. Guo-Qiang, S. Danziger, D. Prather, and M. Hochberg. Myths and rumours of silicon photonics. *Nature Photonics 2012 6:4* **6**, 206–208 (2012)

[9] A. E. Soria. *Design and implementation of nanoantennas on integrated guides and their application on polarization analysis and synthesis*. Doctoral Thesis, Universitat Politècnica de València (2018), URL http://hdl.handle.net/10251/105382

[10] G. Roelkens, J. Van Campenhout, J. Brouckaert, D. Van Thourhout, R. Baets, P. R. Romeo, P. Regreny, A. Kazmierczak, C. Seassal, X. Letartre, G. Hollinger, J. Fedeli, L. Di Cioccio, and C. Lagahe-Blanchard. Iii-v/si photonics by die-to-wafer bonding. *Materials Today* **10**(7), 36–43 (2007)

[11] S. Tanaka, S.-H. Jeong, S. Sekiguchi, T. Kurahashi, Y. Tanaka, and K. Morito. High-output-power, single-wavelength silicon hybrid laser using precise flip-chip bonding technology. *Opt. Express* **20**(27), 28057–28069 (2012)

[12] F. Gardes, A. Brimont, P. Sanchis, G. Rasigade, D. Marris-Morini, L. O'Faolain, F. Dong, J. Fedeli, P. Dumon, L. Vivien, T. Krauss, G. Reed, and J. Martí. High-speed modulation of a compact silicon ring resonator based on a reverse-biased pn diode. *Opt. Express* **17**(24), 21986–21991 (2009)

[13] P. Dong, S. Liao, D. Feng, H. Liang, D. Zheng, R. Shafiiha, C.-C. Kung, W. Qian, G. Li, X. Zheng, A. V. Krishnamoorthy, and M. Asghari. Low vpp, ultralow-energy, compact, high-speed silicon electro-optic modulator. *Opt. Express* **17**(25), 22484–22490 (2009)

[14] A. Rizzo, U. Dave, A. Novick, A. Freitas, S. P. Roberts, A. James, M. Lipson, and K. Bergman. Fabrication-robust silicon photonic devices in standard sub-micron silicon-on-insulator processes (2022)

[15] M. A. Foster, A. C. Turner, M. Lipson, A. L. Gaeta, P. Dumais, F. Gonthier, S. Lacroix, A. Villeneuve, P. G. J. Wigley, G. I. Stegeman, D. Akimov, M. Schmitt, R. Maksimenka, K. Dukel, Y. Kondrat, A. Khokhlov, V. Shevandin, W. Kiefer, and A. M. Zheltikov. Nonlinear optics in photonic nanowires. *Optics Express, Vol. 16, Issue 2, pp. 1300-1320* **16**, 1300–1320 (2008)

[16] A. L. Gaeta, M. Lipson, and T. J. Kippenberg. Photonic-chip-based frequency combs. *Nature Photonics 2019 13:3* **13**, 158–169 (2019)

[17] L. M. Morales. *Phonons Manipulation in Silicon Chips Using Cavity Optomechanics*. Doctoral Thesis, Universitat Politècnica de València (2021), URL http://hdl.handle.net/10251/171461

[18] G. Moody, V. J. Sorger, D. J. Blumenthal, P. W. Juodawlkis, W. Loh, C. Sorace-Agaskar, A. E. Jones, K. C. Balram, J. C. Matthews, A. Laing, M. Davanco, L. Chang, J. E. Bowers, N. Quack, C. Galland, I. Aharonovich, M. A. Wolff, C. Schuck, N. Sinclair, M. Lončar, T. Komljenovic, D. Weld, S. Mookherjea, S. Buckley, M. Radulaski, S. Reitzenstein, B. Pingault, B. Machielse, D. Mukhopadhyay, A. Akimov, A. Zheltikov, G. S. Agarwal, K. Srinivasan, J. Lu, H. X. Tang, W. Jiang, T. P. McKenna, A. H. Safavi-Naeini, S. Steinhauer, A. W. Elshaari, V. Zwiller, P. S. Davids, N. Martinez, M. Gehl, J. Chiaverini, K. K. Mehta, J. Romero, N. B. Lingaraju, A. M. Weiner, D. Peace, R. Cernansky, M. Lobino, E. Diamanti, L. T. Vidarte, and R. M. Camacho. 2022 roadmap on integrated quantum photonics. *Journal of Physics: Photonics* **4**, 012501 (2022)

[19] Genalyte, http://genalyte.com/

[20] Intel, http://intel.com/content/www/us/en/research/intel-labssilicon-photonics-research.html.

[21] P. Bienstman, T. Claes, and W. Bogaerts. Vernier-cascade label-free biosensor with integrated arrayed waveguide grating for wavelength interrogation with low-cost broadband source. *Optics Letters, Vol. 36, Issue 17, pp. 3320-3322* **36**, 3320–3322 (2011)

[22] M. C. Estevez, M. Alvarez, and L. M. Lechuga. Integrated optical devices for lab-on-a-chip biosensing applications. *Laser Photonics Reviews* **6**, 463–487 (2012)

[23] V. Toccafondo, M. V. Andrés, J. García-Rupérez, P. Pérez-Millán, J. G. Castelló, J. L. Cruz, and N. S. Losilla. Real-time and low-cost sensing technique based on photonic bandgap structures. *Optics Letters, Vol. 36, Issue 14, pp. 2707-2709* **36**, 2707–2709 (2011)

[24] C. Sun, M. T. Wade, Y. Lee, J. S. Orcutt, L. Alloatti, M. S. Georgas, A. S. Waterman, J. M. Shainline, R. R. Avizienis, S. Lin, B. R. Moss, R. Kumar, F. Pavanello, A. H. Atabaki, H. M. Cook, A. J. Ou, J. C. Leu, Y. H. Chen, K. Asanović, R. J. Ram, M. A. Popović, and V. M. Stojanović. Single-chip microprocessor that communicates directly using light. *Nature 2015 528:7583* **528**, 534–538 (2015)

[25] L. Vivien. Silicon chips lighten up. *Nature 2015 528:7583* **528**, 483–484 (2015)

[26] F. J. Rodríguez-Fortuño, A. Espinosa-Soria, and A. Martínez. Exploiting metamaterials, plasmonics and nanoantennas concepts in silicon photonics. *Journal of Optics* **18**(12), 123001 (2016)

[27] A. Espinosa-Soria, A. Martínez, and A. Griol. Experimental measurement of plasmonic nanostructures embedded in silicon waveguide gaps. *Optics Express, Vol. 24, Issue 9, pp. 9592-9601* **24**, 9592–9601 (2016)

[28] A. Espinosa-Soria, E. Pinilla-Cienfuegos, F. J. Díaz-Fernández, A. Griol, J. Martí, and A. Martínez. Coherent control of a plasmonic nanoantenna integrated on a silicon chip. *ACS Photonics* **5**, 2712–2717 (2018)

[29] A. I. Kuznetsov, A. E. Miroshnichenko, M. L. Brongersma, Y. S. Kivshar, and B. Luk'yanchuk. Optically resonant dielectric nanostructures. *Science* **354** (2016)

[30] I. Staude and J. Schilling. Metamaterial-inspired silicon nanophotonics. *Nat. Photonics* **11**(5), 274–284 (2017)

[31] L. Novotny and B. Hecht. Principles of nano-optics. *Principles of Nano-Optics* **9780521832243**, 1–539 (2006)

[32] A. V. Kabashin, P. Evans, S. Pastkovsky, W. Hendren, G. A. Wurtz, R. Atkinson, R. Pollard, V. A. Podolskiy, and A. V. Zayats. Plasmonic nanorod metamaterials for biosensing. *Nature Materials 2009 8:11* **8**, 867–871 (2009)

[33] H. A. Atwater and A. Polman. Plasmonics for improved photovoltaic devices. *Nature Materials 2010 9:3* **9**, 205–213 (2010)

[34] B. Luk'Yanchuk, N. I. Zheludev, S. A. Maier, N. J. Halas, P. Nordlander, H. Giessen, and C. T. Chong. The fano resonance in plasmonic nanostructures and metamaterials. *Nature Materials 2010 9:9* **9**, 707–715 (2010)

[35] A. E. Miroshnichenko, S. Flach, and Y. S. Kivshar. Fano resonances in nanoscale structures. *Reviews of Modern Physics* **82**, 2257–2298 (2010)

[36] L. Novotny and N. V. Hulst. Antennas for light. *Nature Photonics 2011 5:2* **5**, 83–90 (2011)

[37] C. M. Soukoulis and M. Wegener. Past achievements and future challenges in the development of three-dimensional photonic metamaterials. *Nature Photonics 2011 5:9* **5**, 523–530 (2011)

[38] N. I. Zheludev and Y. S. Kivshar. From metamaterials to metadevices. *Nature Materials 2012 11:11* **11**, 917–924 (2012)

[39] A. V. Kildishev, A. Boltasseva, and V. M. Shalaev. Planar photonics with metasurfaces. *Science* **339**, 12320091–12320096 (2013)

[40] W. Liu, A. E. Miroshnichenko, and Y. S. Kivshar. Control of light scattering by nanoparticles with optically-induced magnetic responses. *Chinese Physics B* **23**, 047806 (2014)

[41] K. Y. Bliokh, F. J. Rodríguez-Fortuño, F. Nori, and A. V. Zayats. Spin–orbit interactions of light. *Nature Photonics 2015 9:12* **9**, 796–808 (2015)

[42] H. T. Chen, A. J. Taylor, and N. Yu. A review of metasurfaces: physics and applications. *Reports on Progress in Physics* **79**, 076401 (2016)

[43] J. David. *Classical Electrodynamics , 3rd Edition*, Volume 3 (1962)

[44] C. F. Bohren and D. R. Huffman. Absorption and scattering of light by small particles. *Absorption and Scattering of Light by Small Particles* (1998)

[45] N. Papasimakis, V. A. Fedotov, V. Savinov, T. A. Raybould, and N. I. Zheludev. Electromagnetic toroidal excitations in matter and free space. *Nature materials* **15**, 263–271 (2016)

[46] W. Liu and Y. S. Kivshar. Multipolar interference effects in nanophotonics. *Philosophical Transactions of the Royal Society A: Mathematical, Physical and Engineering Sciences* **375** (2017)

[47] K. V. Baryshnikova, D. A. Smirnova, B. S. Luk'yanchuk, and Y. S. Kivshar. Optical anapoles: Concepts and applications. *Advanced Optical Materials* **7**, 1801350 (2019)

[48] W. Liu, J. Shi, B. Lei, H. Hu, A. E. Miroshnichenko, T. Kaelberer, V. Fedotov, N. Papasimakis, D. Tsai, N. Zheludev, W. T. Chen, P. C. Wu, V. Savinov, Y. Z. Ho, Y. f Chau, N. I. Zheludev, and D. P. Tsai. Efficient excitation and tuning of toroidal dipoles within individual homogenous nanoparticles. *Optics Express, Vol. 23, Issue 19, pp. 24738-24747* **23**, 24738–24747 (2015)

[49] T. Kaelberer, V. A. Fedotov, N. Papasimakis, D. P. Tsai, and N. I. Zheludev. Toroidal dipolar response in a metamaterial. *Science* **330**, 1510–1512 (2010)

[50] A. E. Miroshnichenko, A. B. Evlyukhin, Y. F. Yu, R. M. Bakker, A. Chipouline, A. I. Kuznetsov, B. Luk'yanchuk, B. N. Chichkov, and Y. S. Kivshar. Nonradiating anapole modes in dielectric nanoparticles. *Nature Communications 2015 6:1* **6**, 1–8 (2015)

[51] R. Alaee, C. Rockstuhl, and I. Fernandez-Corbaton. Exact multipolar decompositions with applications in nanophotonics. *Advanced Optical Materials* **7**, 1800783 (2019)

[52] L. D. Negro and R. Wang. Engineering non-radiative anapole modes for broadband absorption enhancement of light. *Optics Express, Vol. 24, Issue 17, pp. 19048-19062* **24**, 19048–19062 (2016)

[53] H. P. Urbach, L. Wei, N. Bhattacharya, and Z. Xi. Excitation of the radiationless anapole mode. *Optica, Vol. 3, Issue 8, pp. 799-802* **3**, 799–802 (2016)

[54] B. Luk'yanchuk, R. Paniagua-Domínguez, A. I. Kuznetsov, A. E. Miroshnichenko, and Y. S. Kivshar. Hybrid anapole modes of high-index dielectric nanoparticles. *Physical Review A* **95**, 063820 (2017)

[55] P. C. Wu, C. Y. Liao, V. Savinov, T. L. Chung, W. T. Chen, Y. W. Huang, P. R. Wu, Y. H. Chen, A. Q. Liu, N. I. Zheludev, and D. P. Tsai. Optical anapole metamaterial. *ACS Nano* **12**, 1920–1927 (2018)

[56] S. Q. Li and K. B. Crozier. Origin of the anapole condition as revealed by a simple expansion beyond the toroidal multipole. *Physical Review B* **97**, 245423 (2018)

[57] F. Monticone, D. Sounas, A. Krasnok, and A. Alù. Can a nonradiating mode be externally excited? nonscattering states versus embedded eigenstates. *ACS Photonics* **6**, 3108–3114 (2019)

[58] E. A. Gurvitz, K. S. Ladutenko, P. A. Dergachev, A. B. Evlyukhin, A. E. Miroshnichenko, and A. S. Shalin. The high-order toroidal moments and anapole states in all-dielectric photonics. *Laser Photonics Reviews* (2019)

[59] M. Kerker, D. S. Wang, and C. L. Giles. Electromagnetic scattering by magnetic spheres. *JOSA, Vol. 73, Issue 6, pp. 765-767* **73**, 765–767 (1983)

[60] M. V. Rybin, K. L. Koshelev, Z. F. Sadrieva, K. B. Samusev, A. A. Bogdanov, M. F. Limonov, and Y. S. Kivshar. High- q supercavity modes in subwavelength dielectric resonators. *Physical Review Letters* **119**, 243901 (2017)

[61] J. B. Pendry, D. Schurig, and D. R. Smith. Controlling electromagnetic fields. *Science* **312**, 1780–1782 (2006)

[62] B. Lukyanchuk, R. Paniagua-Domínguez, A. I. Kuznetsov, A. E. Miroshnichenko, and Y. S. Kivshar. Suppression of scattering for small dielectric particles: Anapole mode and invisibility. *Philosophical Transactions of the Royal Society A: Mathematical, Physical and Engineering Sciences* **375** (2017)

[63] Y. Yang, V. A. Zenin, and S. I. Bozhevolnyi. Anapole-assisted strong field enhancement in individual all-dielectric nanostructures. *ACS Photonics* **5**, 1960–1966 (2018)

[64] V. Savinov, N. Papasimakis, D. P. Tsai, and N. I. Zheludev. Optical anapoles. *Communications physics* (2019)

[65] G. Grinblat, Y. Li, M. P. Nielsen, R. F. Oulton, and S. A. Maier. Efficient third harmonic generation and nonlinear subwavelength imaging at a higher-order anapole mode in a single germanium nanodisk. *ACS Nano* **11**, 43 (2016)

[66] G. Grinblat, Y. Li, M. P. Nielsen, R. F. Oulton, and S. A. Maier. Enhanced third harmonic generation in single germanium nanodisks excited at the anapole mode. *Nano Letters* **16**, 4635–4640 (2016)

[67] M. Timofeeva, L. Lang, F. Timpu, C. Renaut, A. Bouravleuv, I. Shtrom, G. Cirlin, and R. Grange. Anapoles in free-standing iii-v nanodisks enhancing second-harmonic generation. *Nano Letters* **18**, 3695–3702 (2018)

[68] D. G. Baranov, R. Verre, P. Karpinski, and M. Käll. Anapole-enhanced intrinsic raman scattering from silicon nanodisks. *ACS Photonics* **5**, 2730–2736 (2018)

[69] A. Martínez, J. Blasco, P. Sanchis, J. V. Galán, J. García-Rupérez, E. Jordana, P. Gautier, Y. Lebour, S. Hernández, R. Guider, N. Daldosso, B. Garrido, J. M. Fedeli, L. Pavesi, and J. Martí. Ultrafast all-optical switching in a silicon-nanocrystal-based silicon slot waveguide at telecom wavelengths. *Nano Letters* **10**, 1506–1511 (2010)

[70] J. S. T. Gongora, A. E. Miroshnichenko, Y. S. Kivshar, and A. Fratalocchi. Anapole nanolasers for mode-locking and ultrafast pulse generation. *Nature Communications 2017 8:1* **8**, 1–9 (2017)

[71] V. Mazzone, J. S. T. Gongora, and A. Fratalocchi. Near-field coupling and mode competition in multiple anapole systems. *Applied Sciences 2017, Vol. 7, Page 542* **7**, 542 (2017)

[72] V. A. Zenin, A. B. Evlyukhin, S. M. Novikov, Y. Yang, R. Malureanu, A. V. Lavrinenko, B. N. Chichkov, and S. I. Bozhevolnyi. Direct amplitude-phase near-field observation of higher-order anapole states. *Nano Letters* (2017)

[73] A. G. Lamprianidis and A. E. Miroshnichenko. Excitation of nonradiating magnetic anapole states with azimuthally polarized vector beams. *Beilstein Journal of Nanotechnology 9:139* **9**, 1478–1490 (2018)

[74] L. Xu, M. Rahmani, K. Z. Kamali, A. Lamprianidis, L. Ghirardini, J. Sautter, R. Camacho-Morales, H. Chen, M. Parry, I. Staude, G. Zhang, D. Neshev, and A. E. Miroshnichenko. Boosting third-harmonic generation by a mirror-enhanced anapole resonator. *Light: Science Applications* pages. 2047–7538 (2018)

[75] J. Tian, H. Luo, Y. Yang, F. Ding, Y. Qu, D. Zhao, M. Qiu, . Sergey, and I. Bozhevolnyi. Active control of anapole states by structuring the phase-change alloy ge 2 sb 2 te 5. *Nature Communications* (2019)

[76] P. Kapitanova, E. Zanganeh, N. Pavlov, M. Song, P. Belov, A. Evlyukhin, and A. Miroshnichenko. Seeing the unseen: Experimental observation of magnetic anapole state inside a high-index dielectric particle. *Annalen der Physik* (2020)

[77] T. Huang, B. Wang, W. Zhang, and C. Zhao. Ultracompact energy transfer in anapole-based metachains. *Nano Letters* **13**, 41 (2021)

[78] J. D. Joannopoulos, P. R. Villeneuve, and S. Fan. Photonic crystals: putting a new twist on light. *Nature 1997 386:6621* **386**, 143–149 (1997)

[79] M. C. Oh, H. J. Lee, M. H. Lee, J. H. Ahn, S. G. Han, and H. G. Kim. Tunable wavelength filters with bragg gratings in polymer waveguides. *Applied Physics Letters* **73**, 2543 (1998)

[80] K. M. Ho, C. T. Chan, and C. M. Soukoulis. Existence of a photonic gap in periodic dielectric structures. *Physical Review Letters* **65**, 3152 (1990)

[81] A. Blanco, E. Chomski, S. Grabtchak, M. Ibisate, S. John, S. W. Leonard, C. Lopez, F. Meseguer, H. Miguez, J. P. Mondla, G. A. Ozin, O. Toader, and H. M. V. Driel. Large-scale synthesis of a silicon photonic crystal with a complete three-dimensional bandgap near 1.5 micrometres. *Nature 2000 405:6785* **405**, 437–440 (2000)

[82] A. Martínez, J. Blasco, J. Martí, P. Sanchis, F. Cuesta-Soto, and J. García. Intrinsic losses of coupled-cavity waveguides in planar-photonic crystals. *Optics Letters, Vol. 32, Issue 6, pp. 635-637* **32**, 635–637 (2007)

[83] R. Halir, P. J. Bock, P. Cheben, A. Ortega-Moñux, C. Alonso-Ramos, J. H. Schmid, J. Lapointe, D. X. Xu, J. G. Wangüemert-Pérez, Íñigo Molina-Fernández, and S. Janz. Waveguide sub-wavelength structures: a review of principles and applications. *Laser Photonics Reviews* **9**, 25–49 (2015)

[84] S.-G. Lee and R. Magnusson. Essential differences between te and tm band gaps in periodic films at the first bragg condition. *Optics Letters, Vol. 44, Issue 19, pp. 4658-4661* **44**, 4658–4661 (2019)

[85] J. García, P. Sanchis, A. Martínez, J. Martí, N. A. R. Bhat, J. E. Sipe, M. Soljacic, S. G. Johnson, S. Fan, M. Ibanescu, E. Ippen, J. Joannopoulos, M. Notomi, K. Yamada, A. Shinya, J. Takahashi, C. Takahashi, and I. Yokohama. 1d periodic structures for slow-wave induced non-linearity enhancement. *Optics Express, Vol. 16, Issue 5, pp. 3146-3160* **16**, 3146–3160 (2008)

[86] W. Sohler and R. D. L. Rue. Integrated optics – new material platforms, devices and applications. *Laser Photonics Reviews* **6**, A21–A22 (2012)

[87] M. Soltani, S. Yegnanarayanan, A. Adibi, A. Liu, R. Jones, L. Liao, D. Samara-Rubio, D. Rubin, O. Cohen, R. Nicolaescu, and M. Paniccia. Ultra-high q planar silicon microdisk resonators for chip-scale silicon photonics. *Optics Express, Vol. 15, Issue 8, pp. 4694-4704* **15**, 4694–4704 (2007)

[88] F. J. Rodríguez-Fortuño, I. Barber-Sanz, D. Puerto, A. Griol, and A. Martínez. Resolving light handedness with an on-chip silicon microdisk. *ACS Photonics* **1**, 762–767 (2014)

[89] M. Borghi, C. Castellan, S. Signorini, A. Trenti, and L. Pavesi. Nonlinear silicon photonics. *Journal of Optics* **19**, 093002 (2017)

[90] R. Colom, L. Xu, L. Marini, F. Bedu, I. Ozerov, T. Begou, J. Lumeau, A. E. Miroshnishenko, D. Neshev, B. T. Kuhlmey, S. Palomba, and N. Bonod. Enhanced four-wave mixing in doubly resonant si nanoresonators. *ACS Photonics* **6**, 1295–1301 (2019)

[91] D. A. Bobylev, D. A. Smirnova, and M. A. Gorlach. Nonlocal response of mie-resonant dielectric particles. *Physical Review B* **102**, 115110 (2020)

[92] A. Patoux, C. Majorel, P. R. Wiecha, A. Cuche, O. L. Muskens, C. Girard, and A. Arbouet. Polarizabilities of complex individual dielectric or plasmonic nanostructures. *Physical Review B* **101**, 235418 (2020)

[93] T. J. Davis, K. C. Vernon, D. E. Gómez, S. Zhang, D. A. Genov, Y. Wang, M. Liu, X. Zhang, P. W. Barber, R. K. Chang, H. Massoudi, and E. calculations. Effect of retardation on localized surface plasmon resonances in a metallic nanorod. *Optics Express, Vol. 17, Issue 26, pp. 23655-23663* **17**, 23655–23663 (2009)

[94] R. Yu, L. M. Liz-Marzán, and F. J. G. D. Abajo. Universal analytical modeling of plasmonic nanoparticles. *Chemical Society Reviews* **46**, 6710–6724 (2017)

[95] Comsol multiphysics 5.3a

[96] A. Espinosa-Soria and A. Martínez. Transverse spin and spin-orbit coupling in silicon waveguides. *IEEE Photonics Technology Letters* **28**, 1561–1564 (2016)

[97] Rsoft bandsolve.

[98] Cst studio suite 2019, 2020 and 2021

[99] X. Cai, J. Wang, M. J. Strain, B. Johnson-Morris, J. Zhu, M. Sorel, J. L. O'Brien, M. G. Thompson, and S. Yu. Integrated compact optical vortex beam emitters. *Science* **338**, 363–366 (2012)

[100] M. Burresi, R. J. Engelen, A. Opheij, D. V. Oosten, D. Mori, T. Baba, and L. Kuipers. Observation of polarization singularities at the nanoscale. *Physical Review Letters* **102**, 033902 (2009)

[101] B. L. Feber, N. Rotenberg, D. M. Beggs, and L. Kuipers. Simultaneous measurement of nanoscale electric and magnetic optical fields. *Nature Photonics 2013 8:1* **8**, 43–46 (2013)

[102] M. Burresi, T. Kampfrath, D. V. Oosten, J. C. Prangsma, B. S. Song, S. Noda, and L. Kuipers. Magnetic light-matter interactions in a photonic crystal nanocavity. *Physical Review Letters* **105**, 123901 (2010)

[103] S. Vignolini, F. Intonti, F. Riboli, L. Balet, L. H. Li, M. Francardi, A. Gerardino, A. Fiore, D. S. Wiersma, and M. Gurioli. Magnetic imaging in photonic crystal microcavities. *Physical Review Letters* **105**, 123902 (2010)

[104] E. Díaz-Escobar, T. Bauer, E. Pinilla-Cienfuegos, Ángela I. Barreda, A. Griol, L. Kuipers, and A. Martínez. Radiationless anapole states in on-chip photonics. *Light: Science Applications 2021* **10, 204** (2021)

[105] C. W. Hsu, B. Zhen, A. D. Stone, J. D. Joannopoulos, and M. Soljacic. Bound states in the continuum. *Nature Reviews Materials 2016 1:9* **1**, 1–13 (2016)

[106] E. Díaz-Escobar, Ángela I. Barreda, A. Griol, and A. Martínez. Experimental observation of higher-order anapoles in individual silicon disks under in-plane illumination. *Applied Physics Letters* **121**, 201105 (2022)

[107] Y. He, G. Guo, T. Feng, Y. Xu, and A. E. Miroshnichenko. Toroidal dipole bound states in the continuum. *Physical Review B* **98**, 161112 (2018)

[108] C. Cui, S. Yuan, X. Qiu, L. Zhu, Y. Wang, Y. Li, J. Song, Q. Huang, C. Zeng, and J. Xia. Light emission driven by magnetic and electric toroidal dipole resonances in a silicon metasurface. *Nanoscale* **11**, 14446–14454 (2019)

[109] L. Ding, D. Morits, R. Bakker, S. Li, D. Eschimese, S. Zhu, Y. F. Yu, R. Paniagua-Dominguez, and A. I. Kuznetsov. All-optical modulation in chains of silicon nanoantennas. *ACS Photonics* **7**, 1001–1008 (2020)

[110] D. Pereira-Martín, M. Luque-González, J. G. Wangüemert-Pérez, A. Hadij-Elhouati, Íñigo Molina-Fernández, P. Cheben, J. H. Schmid, S. Wang, W. N. Ye, J. Ji˘jiří, J. Jiříčtyroký, and A. Ortega-Moñux. Complex spectral filters in silicon waveguides based on cladding-modulated bragg gratings. *Optics Express, Vol. 29, Issue 11, pp. 15867-15881* **29**, 15867–15881 (2021)

[111] D. Farnesi, S. Pelli, S. Soria, G. N. Conti, X. L. Roux, M. M. Ballester, L. Vivien, P. Cheben, P. Cheben, and C. Alonso-Ramos. Metamaterial engineered silicon photonic coupler for whispering gallery mode microsphere and disk resonators. *Optica, Vol. 8, Issue 12, pp. 1511-1514* **8**, 1511–1514 (2021)

[112] E. Díaz-Escobar, L. Mercadé, Ángela I. Barreda, J. García-Rupérez, and A. Martínez. Photonic bandgap closure and metamaterial behavior in 1d periodic chains of high-index nanobricks. *Photonics* **9**, 691 (2022)

[113] I. Staude and J. Schilling. Metamaterial-inspired silicon nanophotonics. *Nature Photonics 2017 11:5* **11**, 274–284 (2017)

[114] M. V. Rybin, D. S. Filonov, K. B. Samusev, P. A. Belov, Y. S. Kivshar, and M. F. Limonov. Phase diagram for the transition from photonic crystals to dielectric metamaterials. *Nature Communications 2015 6:1* **6**, 1–6 (2015)

[115] S. V. Li, Y. S. Kivshar, and M. V. Rybin. Toward silicon-based metamaterials. *ACS Photonics* **5**, 4751–4757 (2018)

[116] K. Koshelev, S. Kruk, E. Melik-Gaykazyan, J. H. Choi, A. Bogdanov, H. G. Park, and Y. Kivshar. Subwavelength dielectric resonators for nonlinear nanophotonics. *Science* **367**, 288–292 (2020)

[117] A. Karabchevsky, A. Katiyi, A. S. Ang, and A. Hazan. On-chip nanophotonics and future challenges. *Nanophotonics* **9**, 3733–3753 (2020)

[118] S. Zanotto, G. Conte, L. C. Bellieres, A. Griol, D. Navarro-Urrios, A. Tredicucci, A. Martínez, and A. Pitanti. Optomechanical modulation spectroscopy of bound states in the continuum in a dielectric metasurface. *PHYSICAL REVIEW APPLIED* **17**, 44033 (2022)

[119] P. Cheben, R. Halir, J. H. Schmid, H. A. Atwater, and D. R. Smith. Subwavelength integrated photonics. *Nature 2018 560:7720* **560**, 565–572 (2018)